The Dissertation Committee for Yonduck Sung
certifies that this is the approved version of the following dissertation:

Large Eddy Simulation of TiO_2 Nanoparticle Evolution in Turbulent Flames

Committee:

Venkat Raman, Supervisor

Robert D. Moser, Co-supervisor

Ofodike A. Ezekoye

Ronald D. Matthews

Noel Clemens

Large Eddy Simulation of TiO_2 Nanoparticle Evolution in Turbulent Flames

by

Yonduck Sung, B.S., M.S.M.E

DISSERTATION

Presented to the Faculty of the Graduate School of

The University of Texas at Austin

in Partial Fulfillment

of the Requirements

for the Degree of

DOCTOR OF PHILOSOPHY

THE UNIVERSITY OF TEXAS AT AUSTIN

Decembert 2011

Acknowledgments

Special thanks to Hyejin Lee, my wife and Yoon-Ah Sung, my daughter for their love and support. Also to Professor Venkat Raman, my advisor, who has guided me to this point with his great passion, understanding, and patience.

Large Eddy Simulation of TiO_2 Nanoparticle Evolution in Turbulent Flames

Publication No. _____

Yonduck Sung, Ph.D.
The University of Texas at Austin, 2011

Supervisor: Venkat Raman
Co-supervisor: Robert D. Moser

Flame based synthesis is a major manufacturing process of commercially valuable nanoparticles for large-scale production. However, this important industrial process has been advanced mostly by trial-and-error based evolutionary studies owing to the fact that it involves tightly coupled multi-physics flow phenomena. For large scale synthesis of nanoparticles, different physical and chemical processes exist, including turbulence, fuel combustion, precursor oxidation, and nanoparticle dynamics exist. A reliable and predictive computational model based on fundamental physics and chemistry can provide tremendous insight. Development of such comprehensive computational models faces challenges as they must provide accurate descriptions not only of the individual physical processes but also of the strongly coupled, nonlinear interactions among them.

In this work, a multiscale computational model for flame synthesis of TiO_2 nanoparticles in a turbulent flame reactor is presented. The model is based on the large-eddy simulation (LES) methodology and incorporates detailed gas phase combustion and precursor oxidation chemistry as well as a comprehensive nanoparticle evolution model. A flamelet-based model is used to model turbulence-chemistry interactions. In particular, the transformation of $TiCl_4$ to the solid primary nucleating TiO_2 nanoparticles is represented using an unsteady kinetic model considering 30 species and 70 reactions in order to accurately describe the critical nanoparticle nucleation process. The evolution of the TiO_2 number density function is tracked using the quadrature method of moments (QMOM) for univariate particle number density function and conditional quadrature method of moments (CQMOM) for bivariate density distribution function. For validation purposes, the detailed computational model is compared against experimental data obtained from a canonical flame-based titania synthesis configuration, and reasonable agreement is obtained.

Table of Contents

List of Tables

List of Figures

Chapter 1

Introduction

1.1 Nanoparticles and their applications

Nanoparticles can be defined as a single or group of structured nano-sized (order of 1∼1000 nm) particles that serve as the building blocks of desired materials or devices. A wide range of important engineering applications of nanoparticles are recognized to date, including vehicle tires (carbon black) [8], gas detection sensors (SnO_2 and TiO_2) [9], optical fibers (SiO_2) [10], reinforcing agents (SiO_2 and carbon black) [11], flowing aids (SiO_2) [12], solutions for polishing processes (Al_2O_3) [6], calcium supplements ($Ca_3(PO_4)_2$) [13], and dentures (SiO_2) [6]. These examples constitute a mere fraction of the nanoparticle applications currently used in actual marketed products and/or industrial processes.

Of the many different types of nanoparticles, metal oxide particles such as titania (TiO_2) and zirconia (ZrO_2) draw particularly wide attention across diverse fields of engineering and science due to their multi-disciplinary usages. Titania nanoparticles alone have diversified industrial uses including catalyst supports [4], photo catalysts [14], ultra-violet blocking materials [15], surface treatments (e.g. antifog coating [16]), cosmetic applications [17], and paint

pigments (TiO_2) [4]. In addition, fine metal oxide particles exhibit potentially beneficial properties in environmental remediation. For example, titania nanoparticles can be used to reduce of automobile nitrogen oxide emission [18] and zirconia nanoparticle based fuel cell electrolytes can be used in fuel cell systems to generate higher power density and a longer life span [19]. Other examples include air treatment, water purification [20], and solar cell panels [21]. Several other environmental applications utilize nanoparticles as well [10, 17, 22–26]. A robust manufacturing process will have a direct and broad impact on the use of metal oxide nanoparticles.

1.2 Flame synthesis of nanoparticles

Although nanoparticles can be fabricated in several ways [27], combustion-based synthesis has been one of most successful techniques for industry level production of commercial grade nanoparticles [28]. This is attributed to favorable characteristics of flame synthesis as it provides high purity nanoparticles with a good production scalability [29] while utilizing a relatively simple "single-step" process without involving large quantities of wet chemicals. Besides, the high temperature flame in combustion-based synthesis is able to provide the driving energy for the precursor (a raw material used to create the target nanoparticles) conversion process without requiring additional energy sources (e.g. heaters [30], plasma [31], electricity [32], or lasers [33]), making the flame synthesis a more economical route over competing methods for high-rate synthesis. Combustion-based methods are also favorable for the

mass production of metal oxide nanoparticles because a flame is one of the most economical and readily accessible sources for fast metal oxidation processes. Therefore, it is not surprising that all of the aforementioned (Sec. 1.1) metal oxide nanoparticles are currently produced by combustion-based methods.

Fig .1.1 shows a generalized schematic of the flame synthesis process of nanoparticles. Here, the liquid or gas-phased precursor of the target nanoparticles is introduced into a pre-existing high temperature flame, which is highly turbulent in large scale industrial reactors. In general, the liquid precursor is dissolved in a fuel prior to ejection. For gas-phase precursors, the fuel is pre-vaporized before mixing with the precursor vapor flow. The precursor-fuel mixture, either gaseous or liquid, is often carried by an inert diluent gas stream to ensure consistent delivery. Once introduced into a pre-existing flame, the fuel is rapidly evaporated (for liquid precursors) and consumed to sustain the flame, exposing the precursor to the high temperature environment. The subsequent formation of solid nanoparticles from individual and/or clustered precursor molecules follows via both gas-phase chemical reactions and surface reactions. The nucleated particles are subject to collisions with other nanoparticles as well as surface reactions, resulting in larger individual particles or clustered particle structures called agglomerates (physically bonded) or aggregates (chemically bonded) [24]. Sintering or coalescence usually occurs concurrently when particles collide in the high temperature region of the reaction. This type of sintering-involved collision process is referred to as coagulation [34] and is largely responsible for the particle size increase as well as

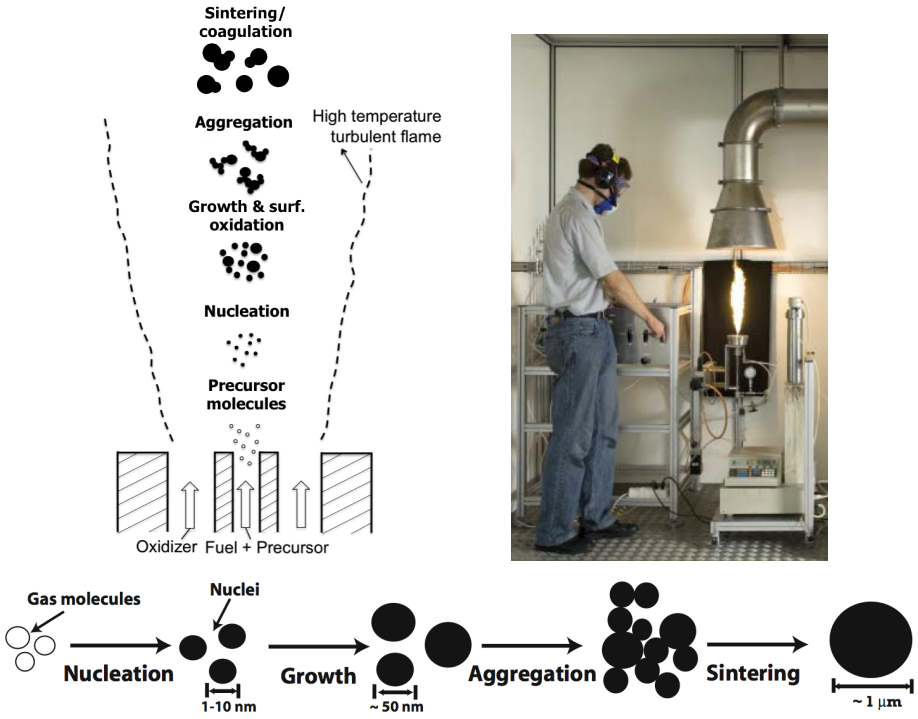

Figure 1.1: Generalized schematic of flame synthesis process and an actual laboratory facility used at ETH Zürich [6].

the formation of aggregates during flame synthesis.

1.2.1 Flame aerosol synthesis (FAS) and flame spray pyrolysis (FSP) of nanoparticles

In general, there are two types of nanoparticle flame synthesis methods which depend on the precursor phase, either gaseous or liquid. The former is often referred to as vapor-fed aerosol synthesis or gas-phase flame aerosol synthesis (FAS) [6, 24, 28], where volatile nanoparticle precursors are vaporized and converted to nanoparticles by gas phase nucleation. FAS is an impor-

tant industrial process, being responsible for substantial amounts of current commercial nanoparticle production. By volume, over 90% of titania nanoparticles is annually manufactured in this way [8]. The latter case is known as liquid-fed aerosol synthesis [6], where the liquid precursor solution is sprayed into pre-existing gas phase flames, evaporated, and nucleated to nanoparticles. For non-premixed liquid aerosol spray flames, a pilot flame is often used to sustain and stabilize spray combustion and to facilitate precursor solution evaporation. This type of pilot assisted liquid-fed aerosol synthesis is usually referred to as flame spray pyrolysis (FSP) [6, 35, 36]. Unlike gas phase synthesis, FSP can utilize non-volatile liquid precursors and hence is suitable for the nanoparticle production that require liquid precursors [37]. Besides, liquid precursors are advantageous when producing multicomponent nanoparticles from multiple precursors because a homogenous precursor solution can be obtained [38]. FSP has been used to successfully produce a wide range of nanoparticles [25, 39–43] and is a highly promising tool for large-scale production of important novel metal oxide nanoparticles [23, 44].

1.3 Literature survey

Because of its practical importance, flame synthesis of nanoparticles has been an important topic for engineers and scientists and many computational investigations have been made. The computational modeling of such flows usually requires flow field description, chemistry, and population balance modeling. In CFD, the flow field is described solving discretized versions of the

flow continuity and momentum equations. For particle-laden flows, population balance model is used to model the evolution of nanoparticles (nucleation, aggregation, surface growth, and sintering) in the flow fields with convection and diffusion effects considered.

Johannessen et al. [7, 45] studied flame synthesis of alumina (Al_2O_3) and titania (TiO_2) in laboratory flame reactors. In this study, simple one-step chemistry models were used for both particle formation chemistry as well as flame chemistry, which was decoupled from the particle oxidation chemistry. The flow field was described using a $k - \epsilon$ Reynolds-averaged Navier Stokes (RANS) approach. The particle characteristics were obtained solving separate transportation equations about the particle number density, particle volume, and particle surface area simultaneously with nucleation, aggregation, surface growth, and sintering effects considered. The importance of this study lies in the fact it is the first meaningful CFD-based investigation of flame synthesis of nanoparticles using actual flame configurations. However, the model used in the study cannot provide the particle number density function (NDF), a particle distribution in terms of particle quantities of interest, such as particle volume and surface area. The NDF can be found by solving a population balance equation. The study done by Kim et al. [46] solved this equation in a reactive flow field. The study was similar to that of Johanessen et al. except that it was about the silica (SiO_2) nanoparticles. Unlike Johanessen et al. [7, 45], however, Kim et al. [46] computed the particle number density function (NDF), which was discretized in two coordinate directions (bivariate

population balance) using a sectional method. Besides, they used a multistep chemistry to describe a H_2/O_2 flame while using a two-step mechanism for the precursor oxidation chemistry. The study was the first application of a bivariate population model in a CFD-based study of a real flame synthesis configuration. However, only a laminar flow reactor was considered, and the model is not directly applicable to turbulent flows.

Since turbulence affects the transport of species, the evolution of particles in a turbulent flow is considerably more complex than that in a laminar flow. Hence, detailed modeling of the turbulent flow field is crucial for predicting nanoparticle characteristics. Wang and Garrick [47, 48] used direct numerical simulation (DNS)-based flow field description to model flame synthesis of titania nanoparticles. However, their study was limited in that the flow was simulated in a two dimensional computational domain. Besides, only a one-step chemistry mechanism was used, which only accounts for the heat release effects but the interaction of the free-radicals with precursor oxidation and nucleation processes are not captured. Later, Zucca et al. [49] and Marchisio and Barresi [50] reported detailed studies about soot formation using a bivariate population balance model. Their models were based on RANS for turbulence modeling and direct quadrature method of moments (DQMOM) for population balance modeling. These studies are important in that the models successfully described NDF using an effective bivariate modeling approach with DQMOM. However, no realistic flame configuration was studied and no direct comparison with measurements were made.

Table 1.1 shows a list of studies in past ten years concerning the numerical modeling of particle-laden flows in the context of nanoparticle synthesis. Although significant amount of research has been carried out on the computational modeling of nanoparticle evolution, relatively less attention has been paid to the modeling of particle transport in turbulent flow. To develop a reliable computational model, it is necessary to consider 1) accurate gas-phase turbulence description using LES or direct numerical simulation (DNS), 2) detailed chemistry-turbulence interaction model, including combustion and particle nucleation, and 3) advanced multi-dimensional (i.e. number density function is described by two or more parameters) population balance model with important nanoparticle evolution events, such as nucleation, aggregation, and sintering, considered. This is because the particle evolution process is extremely sensitive to local thermochemical states and therefore advanced modeling for turbulence is highly desirable. Besides, the evolution process has to be described by at least two parameters (e.g. particle volume and surface area in order to account for surface-based processes such as sintering) for a model to become physically sound. To the author's knowledge, such detailed description of flame synthesis of nanoparticles has not been carried out so far. In this regard, the proposed work considers all three requirements listed above.

Table 1.1: Prior studies on computational modeling of nanoparticle synthesis using CFD

Paper	**Material**	**Precursor (phase)**	**Reactor geometry**	**Turb. model**	**Combust. model (fuel/ox)**	**PBE model**	**Precursor chemistry**	**Particle dynamics**	**Actual config.***
Johannessen et al. '00 [7]	Al_2O_3	ATSB (gas)	Cyl. coflow jet	RANS (k-ϵ)	One-step (CH_4/Air)	Kruis [51]	One-step	Nucl., growth, coag., coales.	Same paper [7]
Johannessen et al. '01 [45]	TiO_2	$TiCl_4$ (gas)	Cyl. coflow jet	RANS	One-step (CH_4/Air)	Kruis [51]	One-step	Nucl., growth, coag., coales.	Pratsinis et al. [4]
Modem et al. '02 [52]	N/A (coag. only)	N/A (coag. only)	2D mixing layer	DNS (2D)	N/A	Sectional	N/A (coag. only)	Coag. only	N/A
Settumba & Garrick '03 [53]	N/A (coag. only)	N/A (coag. only)	2D mixing layer	DNS (2D)	N/A	MOM	N/A (coag. only)	Coag. only	N/A
Moody & Collins '03 [54]	TiO_2	$TiCl_4$ (gas)	Isotropic turb.	DNS	N/A	QMOM	One-step	Nucl., coag.	N/A
Jeong & Choi '03 [55]	TiO_2	$TiCl_4$ (gas)	Cyl. tube	N/A (laminar)	N/A (heated wall)	Sectional (2D)	One-step	Nucl., coag., coales.	Ahktar et al. [56]
Kim et al. '03 [46]	SiO_2	$SiCl_4$ (gas)	Cyl. coflow jet	N/A (laminar)	20 spcs, 15 rxns. (H_2/O_2)	Sectional (2D)	Two-step	Nucl., coag., coales.	Hwang et al. [57]
Wang & Fox '03 [58]	$BaSO_4$	Ba, SO_4 (liquid)	PFR	RANS (k-ϵ)	N/A (precipitation)	QMOM	One-step	Nucl., growth, coag.	N/A
Marchisio et al. '03 [59]	N/A (coag. only)	N/A	Taylor-Couette	RANS (k-ϵ)	N/A (precipitation)	QMOM	N/A (coag. only)	Coag. only	N/A
Miller & Garrick '04 [60]	N/A (coag. only)	N/A	Planar coflow jet	DNS	N/A	Sectional	N/A (coag. only)	Coag. only	N/A
Pitkänen et al. '05 [42]	SiO_2	TEOS (spray)	Cyl. coflow jet	RANS (k-ϵ)	Eddy dissip. (H_2/O_2)	N/A (nucl. only)	One-step	Nucl. only	N/A
Wang & Garrick '05 [47]	TiO_2	$TiCl_4$ (gas)	Planar coflow jet	DNS (2D)	One-step (CH_4/O_2)	Sectional	One-step	Nucl., growth, coag.	N/A
Wang et al. '05 [61]	Soot	PAHs	Cyl. coflow jet	RANS (k-ϵ)	122 spcs, 677 rxns. (CH_4/Air)	QMOM	Detailed	Nucl., growth, coag. coales.	Wang et al. [62]
Zucca et al. '06 [49]	Soot	C_2H_2	Cyl. coflow jet	RANS (k-ϵ)	19 spcs equilbrium (C_2H_2/Air)	DQMOM	One-step	Nucl., growth, coag.	N/A
Wang & Garrick '06 [48]	TiO_2	$TiCl_4$ (gas)	2D mixing layer	DNS (2D)	N/A	Sectional	One-step	Nucl., coag.	N/A

Paper	**Material**	**Precursor (phase)**	**Reactor geometry**	**Turb. model**	**Combust. model (fuel/ox)**	**PBE model**	**Precursor chemistry**	**Particle dynamics**	**Actual config.***
Yu et al. '06 [63]	N/S (coag. only)	N/A (coag. only)	Planar jet	LES	N/A	MOM	N/S (coag. only)	Coag. only	N/A
Soos et al. '07 [64]	N/A (coag. only)	N/A (coag. only)	Taylor-Couette	RANS	N/A	Sectional	N/A (coag. only)	Coag. only	Same paper [64]
Yu et al. '08 [65]	TiO_2	TTIP (gas)	Cyl. coflow jet	RANS (k-ϵ)	Eddy dissip. (CH_4/Air)	QMOM	One-step	Nucl., growth, coag., coales.	Wenger & Pratsinis [28]
Yu et al. '08 [66]	TiO_2	$TiCl_4$ (gas)	Cyl. coflow jet	RANS (k-ϵ)	Eddy dissip. (CH_4/Air)	QMOM	One-step	Nucl., growth, coag., coales.	Pratsinis et al. [4]
Mueller et al. [67] '09	Soot	PAHs	1D counter diffusion	N/A (laminar)	149 spcs, 1651 rxns.. (C_2H_2/Air)	HMOM, DQMOM (2D)	Blanquart & Pitsch [14]	Nucl., growth, coag., coales.	Pels & Peters [68]
Marchisio & Barresi '09 [50]	Soot	C_2H_2	Cyl. coflow jet	RANS (k-ϵ)	Flamelet	DQMOM (pseudo 2D)	One-step	Nucl. growth, coag.	N/A
Petitti et al. [69]	Bubble	N/A	Stirred reactor	RANS (k-ϵ)	N/A	QMOM	N/A	Aggregation	Laakkonen et al. [70]
Veroli & Rigopoulos [71]	$BaSO_4$	$BaCl_2$	Concentric pipes	RANS	N/A	Joint PDF (1D)	One-step	Nucl.,coag.	Balyga & Orciuch [72]

(Table 1.1 continued)

1.4 Motivation and objective

Large-scale production of commercial grade nanoparticles in flames involves the precise control of the desired characteristics of final nanoparticles, such as particle size, morphology, and composition. Obtaining satisfactory control over these characteristics is, however, a challenging task for they are determined by highly complicated and strongly interlinked chemical and physical processes, including turbulence, gas-phase (FAS) or spray (FSP) combustion, precursor chemistry, and nanoparticle dynamics. The formation and evolution of nanoparticles are determined by the chemical reactions as well as the particle history in flames. Hence, they are dependent on both the thermochemical states of the participating chemical species and their transportation processes, which are generally dictated by a strong turbulent flow in a large scale industrial reactor. Besides, combustion heat release has significant effects on the flow characteristics and chemical reactions, thereby substantially affecting the final state of the nanoparticles. For FSP, additional complexity is added on top of these with droplet evaporation, transportation processes and spray combustion. Without doubt, this is a highly complex process involving tightly coupled chemical and physical phenomena with wide ranges of length and time scales. Not surprisingly, a complete understanding of the comprehensive physics behind this system has not been available and even today evolutionary trial-error based approaches are used by the industry to design these flow systems. This trial-error based optimization is often uneconomical and time consuming. A reliable and predictive computational model, however, can al-

ter this design process. Such a model based on fundamental chemistry and physics will be able to provide valuable insights and understanding of the underlying physics of the flame synthesis process. This will consequently lead to an efficient optimization process for large scale production. Hence, to develop such a computational tool with proper multiphysical model is of significant importance and our research effort has been focusing on this goal. Our research activities have drawn promising results including successful simulation of FSP of titania nanoparticles [73] and LES of titania particle evolution in actual experimental flame configurations [2].

Chapter 2

LES-based modeling of flame synthesis of TiO_2 nanoparticles

2.1 General modeling approach

The comprehensive description of nanoparticle evolution will utilize four key components: 1) A flow-field description based on the LES methodology, 2) a description of gas-phase combustion, 3) a methodology to include detailed precursor chemistry in LES computations, and 4) the evolution of nanoparticle population. In this study, we focus on gas-phase synthesis in a non-premixed flame reactor. Below, the individual components and the coupling between the models are described.

2.2 Gas-phase turbulence and LES

In typical flame synthesis, TiO_2 nanoparticles are formed through oxidation of the gas-phase precursor ($TiCl_4$) via a series of chemical reactions in a high-temperature environment. Precursor chemistry has significant importance in nanoparticle synthesis since it is responsible for both solid nanoparticle nucleation and surface reactions. This nucleation and other chemical reactions are extremely sensitive to the local thermochemical state of the flow field as

well as the transport history of the participating chemical species. Therefore, in models for flame synthesis, it is of paramount importance to have an accurate description of flow dynamics and turbulence in presence of chemical reactions. Large eddy simulation (LES), with its ability to accurately capture energy-containing large scale motions, has become a promising tool for turbulent reactive flow and hence used in this study.

2.2.1 Flow field decomposition and Favre-filtering

LES resolves all large scale motions of a turbulent flow. The filtering operation separates the turbulent length scales into resolved and unresolved portions, separated by a pre-defined filter-width [74]. LES directly tracks the motions larger than the size set by the filter, removing the turbulent scales smaller than the filter size, called sub-filter scales, from the direct calculation. These unresolved, sub-filter scales are modeled and therefore their effect on the flow field is determined indirectly. Although combustion occurs exclusively at the small scales and needs to be modeled in LES [75], chemical reaction are controlled by the large scale mixing process, which is captured accurately in LES. Consequently, LES exhibits superior performance as compared to RANS [76].

In LES, an instantaneous turbulent flow field is decomposed into resolved and sub-filter fields, and only the resolved field is directly computed on Eulerian grid. For an arbitrary variable Q, this decomposition is defined as

$$Q = \widetilde{Q} + Q'', \tag{2.1}$$

where $\widetilde{Q} = \overline{\rho Q}/\overline{\rho}$ is the Favre-filtered variable and Q'' is the unresolved field.

Here, $\overline{\rho}$ is the filtered density, which will be described shortly after introducing the filtering concept. A tilde (e.g. $\widetilde{Q}$) on a variable indicates the variable is either Favre-filtered or composed of Favre-filtered variables. A flat bar (e.g. $\overline{\rho}$) is used to indicate a filtered variable.

The flow field decomposition is done by a procedure called spatial filtering operation. In variable-density flows, this can be represented for a variable Q as

$$\widetilde{Q}(\mathbf{y},t) = \frac{1}{\overline{\rho}} \int_{-\infty}^{+\infty} \rho Q(\mathbf{x},t) G(\mathbf{x}-\mathbf{y}) d\mathbf{x}, \tag{2.2}$$

where G is the filtering kernel and t is time and $\mathbf{x}$ and $\mathbf{y}$ are the vectors representing the physical space. $\overline{\rho}$ is the filtered density and found by

$$\overline{\rho} = \overline{\rho}(\mathbf{y},t) = \int_{-\infty}^{+\infty} \rho(\mathbf{x},t) G(\mathbf{x}-\mathbf{y}) d\mathbf{x}. \tag{2.3}$$

In most LES computations, G is assumed to be a box filter [77]. It is also assumed that the filtering operation commutes with differentiation, thereby eliminating filter width as an explicit parameter in the simulations.

2.2.2 LES flow equations

Derivation of the LES governing equations starts from the original, unfiltered Navier-Stokes equation. Neglecting body forces, the conserative form of the equation is

$$\frac{\partial \rho}{\partial t} + \frac{\partial \rho u_j}{\partial x_j} = 0 \quad \text{(continuity)} \tag{2.4}$$

$$\frac{\partial \rho u_i}{\partial t} + \frac{\partial \rho u_i u_j}{\partial x_j} = -\frac{\partial P}{\partial x_i} + \frac{\partial \tau_{ij}}{\partial x_j} \quad \text{(momentum)}, \tag{2.5}$$

where u_i is i-th component of the velocity vector, P is pressure, and τ_{ij} is the viscous stress tensor given by

$$\tau_{ij} = 2\mu\left(S_{ij} - \frac{1}{3}\frac{\partial u_k}{\partial x_k}\delta_{ij}\right) \quad \text{with } S_{ij} = \frac{1}{2}\left(\frac{\partial u_i}{\partial x_j} + \frac{\partial u_j}{\partial x_i}\right), \tag{2.6}$$

where μ is viscosity, δ_{ij} is the Kronecker delta function. Repeated indices imply summation in the equations presented here, unless otherwise mentioned.

The LES flow equations can be obtained by applying the filtering operations (Eq.(2.2)) to the original continuity and momentum equations (Eq.(2.4) and (2.5)). This results in

$$\frac{\partial \overline{\rho}}{\partial t} + \frac{\partial \overline{\rho}\widetilde{u}_j}{\partial x_j} = 0\,, \tag{2.7}$$

$$\frac{\partial \overline{\rho}\widetilde{u}_i}{\partial t} + \frac{\partial \overline{\rho}\widetilde{u}_i\widetilde{u}_j}{\partial x_j} = -\frac{\partial \overline{P}}{\partial x_i} + \frac{\partial \widetilde{\tau}_{ij}}{\partial x_j} - \frac{\partial T_{ij}}{\partial x_j}\,, \tag{2.8}$$

where $\widetilde{\tau}_{ij}$ is the viscous stress tensor based on the filtered variables and given by

$$\widetilde{\tau}_{ij} = 2\overline{\mu}\widetilde{S}_{ij}. \tag{2.9}$$

Here $\widetilde{S}_{ij}$ is the anisotropic part of the strain rate tensor with Favre-filtered velocities and is defined as

$$\widetilde{S}_{ij} = \frac{1}{2}\left(\frac{\partial \widetilde{u}_i}{\partial x_j} + \frac{\partial \widetilde{u}_j}{\partial x_i}\right) - \frac{1}{3}\frac{\partial \widetilde{u}_k}{\partial x_k}\delta_{ij}. \tag{2.10}$$

Note that the isotropic part of the strain rate tensor is combined into the pressure term and not used in the modeling. The next term in the r.h.s of Eq.(2.8) includes the sub-filter stresses T_{ij}, defined as follows:

$$T_{ij} = \overline{\rho}(\widetilde{u_i u_j} - \widetilde{u}_i\widetilde{u}_j). \tag{2.11}$$

This term contains the important information about the effect of sub-filter scale fluctuations. Since the sub-filter scales are not directly solved for, this effect is unknown and hence has to be modeled. For this purpose, the unknown velocity correlation term $\widetilde{u_i u_j}$ is modeled and closed. Providing a closure for this term has been an important subject of LES theory and several models have been suggested [78, 79]. Among them, the most widely used ones are those based on a gradient diffusion hypothesis [78, 80]. Using this hypothesis, the sub-filter stress is modeled as

$$T_{ij} = -2\mu_t \widetilde{S}_{ij}, \tag{2.12}$$

where μ_t is the turbulent eddy viscosity and is obtained from the Smagorinsky model [78]

$$\mu_t = \overline{\rho} C_s \Delta^2 \mathcal{S} \quad \text{or} \quad \nu_t = \mu_t/\overline{\rho} = C_s \Delta^2 \mathcal{S} \tag{2.13}$$

by assuming the local equilibrium of the dissipation and production rates in the sub-filter scales. Here, $\mathcal{S} = \sqrt{\widetilde{S}_{ij}\widetilde{S}_{ij}}$ is the magnitude of the rate-of-strain tensor and Δ is the characteristic filter size. The coefficient C_s is determined using a dynamic procedure [81, 82], which locally adjusts the coefficient based on the LES solution.

2.3 Gas-phase combustion and LES

In present study, the fuel/precursor mixture and oxidizer enter in two different streams, corresponding to a non-premixed flow configuration. Below, the modeling approach for a non-premixed configuration are presented. The

modifications necessary to account for the presence of nanoparticles are also described in detail.

2.3.1 Laminar flamelet approach for LES

Combustion is a phenomenon by which fast oxidation of fuels is used to release stored chemical energy into heat. Therefore, a fundamental basis of any combustion model is the conservation of chemically reactive species mass and energy [75]. The balance equation for the i-th species among n reactive species in a flow field is

$$\frac{\partial \rho y_i}{\partial t} + \nabla \cdot (\rho \mathbf{u} y_i) = \nabla \cdot (\rho \Gamma_i \nabla y_i) + \omega_i(\Phi) \quad (i = 1, 2, \ldots, n), \tag{2.14}$$

where ρ is the density of a species mixture and y_i is the mass fraction of species i, Γ_i is the diffusivity of species i, and Φ=$\{y_1, \ldots, y_n, T\}$ is the entire thermochemical vector. This equation is usually either averaged (in RANS-based approaches) or filtered (in LES-based approaches) in CFD computation. The fundamental issue in combustion modeling lies in the closure of the chemical source term, ω_i, because the filtered source term is not identical to the source term evaluated using the filtered thermochemical composition vector. In other words,

$$\widetilde{\omega_i(\Phi)} \neq \omega_i(\widetilde{\Phi}) \quad \text{(LES)}. \tag{2.15}$$

In the laminar flamelet approach, this problem is overcome by representing a turbulent diffusion flame as an ensemble of strained laminar flame sheets [75]. This allows the gas-phase composition to be represented as a

function of a non-reacting scalar called the mixture fraction (Z), its variance dissipation rate (χ), and the spatial distribution of this scalar. This approach is valid when the reaction zone is sufficiently thin such that it can reside within the smallest eddies of the turbulent flow. Inside these sub-Kolmogorov scales, the flow field is essentially laminar because of the dominant viscous forces. Flamelet-based models assume a laminar flame structure in this quasi-laminar flow field, such as the one obtained from a one-dimensional counter-diffusion flame [75]. In such a flame, gradient-driven reactive diffusion is balanced by flow-field stretching and this balance determines the characteristic reaction zone thickness.

Under such conditions, a non-premixed system can be described by two parameters: the mixture-fraction variable (Z) and the scalar variance dissipation rate (χ). The former serves as a parameter for the local equivalence ratio and the latter serves as a parameter for intensity of flow-field strain. Using these two quantities, a steady-state flamelet equation is obtained [75]:

$$\frac{\rho}{Le_i}\frac{\chi}{2}\frac{d^2 y_i}{dZ^2} + \dot{\omega}_i = 0, \tag{2.16}$$

where ρ is the density of the species mixture and $Le_i = \alpha_i / D_i$ is the Lewis number of chemical species i and equal to the ratio of thermal diffusivity (α_i) to mass diffusivity (D_i). $\dot{\omega}_i$ indicates the chemical source term of y_i and is typically in Arrhenius form. Hence multi-step chemical kinetics can be readily implemented into this equation via $\dot{\omega}_i$. χ is the scalar variance dissipation rate

and is given as

$$\chi = 2D \left(\frac{\partial Z}{\partial x_j} \frac{\partial Z}{\partial x_j} \right), \tag{2.17}$$

where D is the diffusivity of the mixture-fraction variable. Eqn.(2.16) can be solved numerically to yield a tabulated solution that maps the gas-phase composition given the mixture fraction and dissipation rate:

$$y_i = y_i(Z, \chi). \tag{2.18}$$

Typically, the boundary conditions for solving the set of partial differential equations are based on the inflow conditions in the flow problem being considered. Essentially, the composition and temperature of the two streams corresponding to mixture fraction of 0 and 1 need to be specified in order to solve Eq.(2.16).

Given the flamelet solution, in the LES computation it is then sufficient to only solve for mixture fraction and dissipation rate, thereby reducing the computational cost significantly. It should be noted that in LES, only the filtered mixture fraction and dissipation rate can be obtained. If the variations of quantities within a filter volume is viewed as a statistical distribution in LES, the filtered values will then represent the mean of this distribution. Consequently, the filtered gas-phase composition can be obtained if this statistical distribution is modeled using the joint probability density function (PDF) of mixture fraction and dissipation rate:

$$\widetilde{y_i} = \int_0^\infty \int_0^1 y_i(Z, \chi)\, \widetilde{P}(Z, \chi)\, dZ\, d\chi, \tag{2.19}$$

where $\widetilde{P}(Z,\chi) = \rho P(Z,\chi)/\overline{\rho}$, with P being the joint-PDF of mixture fraction and dissipation rate. The PDF can be further written in conditional form as

$$\widetilde{P}(Z,\chi) = \widetilde{P}(\chi|Z)\,\widetilde{P}(Z). \tag{2.20}$$

In general, presumed functional forms are used for these PDFs. Here, the conditioned sub-filter distribution of χ given Z is assumed to be a delta function at $\chi = \widetilde{\chi}$ and the sub-filter distribution of Z is modeled using a β distribution, which is defined by two parameters that are functions of the filtered mixture fraction $\widetilde{Z}$ and filtered mixture-fraction variance $\widetilde{Z''^2} = \widetilde{Z}^2 - \left(\widetilde{Z}\right)^2$. For $0 \leq Z \leq 1$, $\widetilde{P}(Z)$ is

$$\widetilde{P}(Z) = \beta(Z;a,b) \equiv Z^{\,a-1}(1-Z)^{b-1}\frac{\Gamma(a+b)}{\Gamma(a)\Gamma(b)}, \tag{2.21}$$

where the two parameters a and b are given by

$$a = \widetilde{Z}\left(\frac{\widetilde{Z}(1-\widetilde{Z})}{\widetilde{Z''^2}} - 1\right), \quad b = (1-\widetilde{Z})\left(\frac{\widetilde{Z}(1-\widetilde{Z})}{\widetilde{Z''^2}} - 1\right). \tag{2.22}$$

As a consequence, the steady laminar flamelet approach allows $\widetilde{y_i}$ to be parameterized using three filtered quantities $\widetilde{Z}$, $\widetilde{Z''^2}$, and $\widetilde{\chi}$ such that

$$\widetilde{y_i} = \widetilde{y_i}(\widetilde{Z}, \widetilde{Z''^2}, \widetilde{\chi}). \tag{2.23}$$

Other thermochemical parameters are obtained in a similar manner to define the flamelet-based LES state relation:

$$\overline{\rho} = \overline{\rho}(\widetilde{Z}, \widetilde{Z''^2}, \widetilde{\chi}), \quad \widetilde{T} = \widetilde{T}(\widetilde{Z}, \widetilde{Z''^2}, \widetilde{\chi}) \tag{2.24}$$

The quantities $\widetilde{y_i}$, $\overline{\rho}$ and $\widetilde{T}$ are pre-computed and stored in a look-up table. With the three input parameters $(\widetilde{Z}, \widetilde{Z''^2}, \widetilde{\chi})$ obtained from the resolved flow

field, which will be discussed shortly, the look-up table provides the filtered thermochemical state variables to each computational grid cell to model a non-premixed turbulent flame.

The main advantage of the flamelet approximation, therefore, is to obviate the need for solving separate transport equations for the different chemical species. Consequently, only the filtered mixture-fraction equation is evolved in the LES code:

$$\frac{\partial \overline{\rho}\widetilde{Z}}{\partial t} + \frac{\partial \overline{\rho}\widetilde{u}_j\widetilde{Z}}{\partial x_j} = \frac{\partial}{\partial x_j}\left(\overline{\rho}\widetilde{D}\frac{\partial \widetilde{Z}}{\partial x_j}\right) - \frac{\partial \mathbf{M}_j}{\partial x_j}, \tag{2.25}$$

where $\widetilde{D}$ is the filtered molecular diffusivity of the mixture fraction and $\mathbf{M}_j = \overline{\rho}(\widetilde{u_j Z} - \widetilde{u}_j\widetilde{Z})$ is the sub-filter scalar flux that accounts for the effect of unresolved scalar and velocity correlation. This term also requires a closure similar to the sub-filter stresses (Eq.(2.10)). A widely used scalar gradient-diffusion-based closure is chosen here [83]:

$$\mathbf{M}_j = -\overline{\rho}D_t\frac{\partial \widetilde{Z}}{\partial x_j}, \tag{2.26}$$

where D_t is the turbulent diffusivity that needs to be modeled. Similar to the eddy viscosity ν_t (Eq.(2.13)), we use the Smagorinsky model [78] together with the dynamic procedure to determine D_t:

$$D_t = C_Z\Delta^2\mathcal{S}, \tag{2.27}$$

where C_Z is a modeling coefficient determined by the dynamic procedure. The same $\mathcal{S}$ and Δ as in Eq.(2.13) are used.

The other two input parameters for the flamelet look-up table – sub-filter scalar variance and dissipation rate – are modeled using the resolved mixture-fraction fields by assuming local equilibrium of production and dissipation of scalar variance [84]:

$$\widetilde{Z''^2} = C_V \Delta^2 \left(\frac{\partial \widetilde{Z}}{\partial x_j} \frac{\partial \widetilde{Z}}{\partial x_j} \right), \tag{2.28}$$

where C_V is a model coefficient that is obtained dynamically [85]. The filtered dissipation rate is modeled as

$$\widetilde{\chi} = 2\big(\widetilde{D} + D_t\big) \left(\frac{\partial \widetilde{Z}}{\partial x_j} \frac{\partial \widetilde{Z}}{\partial x_j} \right). \tag{2.29}$$

Using the three input parameters obtained from the resolved scalar field via Eqs. (2.25), (2.28), and (2.29), the thermochemical states of the computational grid cells can be retrieved from the prebuilt flamelet look-up table. The flamelet table is constructed using the FlameMaster code [86] with a detailed nucleation mechanism, which is discussed in the next section.

2.4 Unsteady nucleation model with a comprehensive chemical mechanism

2.4.1 Multistep $TiCl_4$ oxidation kinetics

Nucleation is an important sub-step in the formation of the nanoparticles, and needs to be accurately represented in any predictive computational tool. In the past, nucleation has been modeled primarily using a single-step oxidation mechanism for the $TiCl_4$ [55, 66, 87]. However, recent studies by West et al. [1] suggest that the oxidation mechanism proceeds through a large set

of intermediate reactions, and it is important to include these reactions when describing nanoparticle nucleation. However, due to difficulties in obtaining thermochemical data [2], it is only recently that the first detailed chemical kinetics for $TiCl_4$ oxidation process has been proposed [88, 89]. The detailed mechanism proposed by West et al. [88] contains 25 species and 51 reactions and it has been recently extended to 30 species and 66 reactions [1], where the molecules with up to three Ti atoms are considered. However, at 600 K or higher, it is suggested that a nucleus contains at least five Ti atoms [88] and, therefore, additional reactions must be added to account for this. Following the suggestion of West et al. [89], three collision-limited reactions have been added to the extended mechanism to represent the particle nucleation event [2]:

$$\begin{aligned} &Ti_2O_2Cl_4(g) + Ti_3O_4Cl_4(g) \longrightarrow Ti_5O_6Cl_8(s), \\ &Ti_2O_2Cl_5(g) + Ti_3O_4Cl_4(g) \longrightarrow Ti_5O_6Cl_8(s) + Cl(g), \\ &Ti_2O_2Cl_6(g) + Ti_3O_4Cl_4(g) \longrightarrow Ti_5O_6Cl_8(s) + Cl_2(g). \end{aligned} \tag{2.30}$$

In this augmented mechanism, the formation of $Ti_5O_6Cl_8$ molecule is considered as a nucleation event of a solid nanoparticle with following reaction.

$$Ti_5O_6Cl_8 + 2O_2 \longrightarrow 5TiO_2 + 4Cl_2 \tag{2.31}$$

The resulting detailed $TiCl_4$ oxidation mechanism includes 30 species and 70 reactions and shown in Table 2.1.

No.	Reaction	A ($\mathrm{cm^3/(s\,mol\,K)}$)	n	E_a (cal/mol)
1	$TiCl_4$+M $\rightleftharpoons$ $TiCl_3$+Cl+M	5.40E+18	0.00	80236.8
2	$TiCl_3$+M $\rightleftharpoons$ $TiCl_2$+Cl+M	7.70E+18	0.00	92415.6
3	$TiCl_2$+M $\rightleftharpoons$ TiCl+Cl+M	3.20E+17	0.00	122026.8
4	Ti+Cl $\rightleftharpoons$ TiCl	1.00E+13	0.00	0.00
5	$TiCl_2$+Cl_2 $\rightleftharpoons$ $TiCl_4$	1.00E+13	0.00	0.00
6	TiCl+Cl_2 $\rightleftharpoons$ $TiCl_3$	1.00E+13	0.00	0.00
7	$TiCl_3$+Cl_2 $\rightleftharpoons$ $TiCl_4$+Cl	1.00E+13	0.00	0.00
8	$TiCl_2$+Cl_2 $\rightleftharpoons$ $TiCl_3$+Cl	1.00E+13	0.00	0.00
9	TiCl+Cl_2 $\rightleftharpoons$ $TiCl_2$+Cl	1.00E+13	0.00	0.00
10	Ti+Cl_2 $\rightleftharpoons$ TiCl+Cl	1.00E+13	0.00	0.00
11	$TiCl_4$+TiCl $\rightleftharpoons$ $TiCl_3$+$TiCl_2$	1.00E+13	0.00	0.00
12	$TiCl_4$+Ti $\rightleftharpoons$ $TiCl_3$+TiCl	1.00E+13	0.00	0.00
13	$TiCl_2$+TiCl $\rightleftharpoons$ $TiCl_3$+Ti	1.00E+13	0.00	0.00
14	TiCl+TiCl $\rightleftharpoons$ $TiCl_2$+Ti	1.00E+13	0.00	0.00
15	Cl_2+TiO_2Cl_2 $\rightleftharpoons$ Cl+TiO_2Cl_3	1.00E+13	0.00	0.00
16	Cl_2+$Ti_2O_2Cl_3$ $\rightleftharpoons$ Cl+Ti2O_2Cl_4	1.00E+13	0.00	0.00
17	2$TiCl_3$ $\rightleftharpoons$ $TiCl_2$+$TiCl_4$	9.60E+12	0.00	8358.0
18	$TiCl_3$+TiCl $\rightleftharpoons$ 2$TiCl_2$	1.00E+13	0.00	0.00
19	$TiCl_3$+O_2(+M) $\rightleftharpoons$ TiO_2Cl_3(+M) k_∞	1.925E+35	-6.577	9890.9
	k_0	1.06E+36	-6.32	0.0
	$a_0 = 0.1183$ $a_1 = 26.93$ $a_2 =$ 1E+05 $a_3 = 5219$			
20	$TiOCl_3$+ClO $\rightleftharpoons$ TiO_2Cl_3+Cl	1.00E+13	0.00	0.00
21	$TiOCl_2$+Cl $\rightleftharpoons$ $TiOCl_3$	1.00E+13	0.00	0.00
22	$TiOCl_3$+O $\rightleftharpoons$ TiO_2Cl_3	1.00E+13	0.00	0.00
23	TiO_2Cl_2+Cl $\rightleftharpoons$ TiO_2Cl_3	1.00E+13	0.00	0.00
24	TiO_2Cl_2+Cl $\rightleftharpoons$ $TiCl_3$+O_2	1.00E+13	0.00	0.00
25	$TiOCl_3$+O $\rightleftharpoons$ $TiCl_3$+O_2	1.00E+13	0.00	0.00
26	$TiCl_2$+O_2 $\rightleftharpoons$ $TiOCl_2$+O	1.00E+13	0.00	0.00
27	TiO_2Cl_2+O $\rightleftharpoons$ $TiOCl_2$+O_2	1.00E+13	0.00	0.00
28	$TiCl_3$+ClO $\rightleftharpoons$ $TiCl_4$+O	1.00E+13	0.00	0.00
29	$TiCl_2$+ClO $\rightleftharpoons$ $TiCl_3$+O	1.00E+13	0.00	0.00
30	TiCl+ClO $\rightleftharpoons$ $TiCl_2$+O	1.00E+13	0.00	0.00
31	Ti+ClO $\rightleftharpoons$ TiCl+O	1.00E+13	0.00	0.00

Table 2.1: Detailed multistep $TiCl_4$ oxidation chemistry used in this study. The mechanism is based on West et al. [1] and Mehta et al. [2]

No.	Reaction	A ($cm^3/(s\,mol\,K)$)	n	E_a (cal/mol)
32	$TiCl_3+O \rightleftharpoons TiOCl_2+Cl$	1.00E+13	0.00	0.00
33	$TiCl_3+Cl_2O \rightleftharpoons TiCl_4+ClO$	1.00E+13	0.00	0.00
34	$TiCl_3+ClO \rightleftharpoons TiOCl_3+Cl$	1.00E+13	0.00	0.00
35	$TiO_2Cl_2+Cl \rightleftharpoons TiOCl_2+ClO$	1.00E+13	0.00	0.00
36	$O+O_2+M \rightleftharpoons O_3+M$	1.84E+21	-2.80	0.00
37	$ClOO+M \rightleftharpoons Cl+O_2+M$	1.69E+14	0.00	3613.04
38	$Cl+O_2+M \rightleftharpoons ClOO+M$	8.68E+21	-2.90	0.00
39	$Cl+O_3 \rightleftharpoons ClO+O_2$	1.75E+13	0.00	520.584
40	$Cl_2O+Cl \rightleftharpoons Cl_2+ClO$	3.73E+13	0.00	-260.29
41	$Cl+O_2 \rightleftharpoons ClO+O$	8.79E+14	0.00	55043.4
42	$O+Cl_2 \rightleftharpoons ClO+Cl$	4.46E+12	0.00	3278.72
43	$2Cl+M \rightleftharpoons Cl_2+M$	2.23E+14	0.00	-1798.16
44	$2TiOCl_2 \rightleftharpoons Ti_2O_2Cl_4$	1.00E+13	0.00	0.00
45	$TiO_2Cl_2+TiCl_3 \rightleftharpoons Ti_2O_2Cl_4+Cl$	1.00E+13	0.00	0.00
46	$TiO_2Cl_2+TiOCl_2 \rightleftharpoons Ti_2O_3Cl_3+Cl$	1.00E+13	0.00	0.00
47	$TiOCl_2+TiOCl_3 \rightleftharpoons Ti_2O_2Cl_4+Cl$	1.00E+13	0.00	0.00
48	$Ti_2O_3Cl_3+TiOCl_2 \rightleftharpoons Ti_3O_4Cl_4+Cl$	1.00E+13	0.00	0.00
49	$Ti_2O_3Cl_2+Cl \rightleftharpoons Ti_2O_3Cl_3$	1.00E+13	0.00	0.00
50	$Ti_2O_2Cl_3+TiCl_4 \rightleftharpoons Ti_2O_2Cl_4+TiCl_3$	1.00E+13	0.00	0.00
51	$TiO_2Cl_3+TiCl_3 \rightleftharpoons Ti_2O_2Cl_6$	1.00E+13	0.00	0.00
52	$2TiOCl_3 \rightleftharpoons Ti_2O_2Cl_6$	1.00E+13	0.00	0.00
53	$Cl_2+Ti_2O_2Cl_5 \rightleftharpoons Cl+Ti_2O_2Cl_6$	1.00E+13	0.00	0.00
54	$Cl+Ti_2O_2Cl_5 \rightleftharpoons Cl_2+Ti_2O_2Cl_4$	1.00E+13	0.00	0.00
55	$TiCl_3+Ti_2O_2Cl_5 \rightleftharpoons TiCl_4+Ti_2O_2Cl_4$	1.00E+13	0.00	0.00
56	$TiCl_3+Ti_2O_2Cl_6 \rightleftharpoons TiCl_4+Ti_2O_2Cl_5$	1.00E+13	0.00	0.00
57	$TiCl_2OCl \rightleftharpoons TiOCl_2+Cl$	1.00E+13	0.00	0.00
58	$TiCl_2OCl+Cl \rightleftharpoons TiCl_3+ClO$	1.00E+13	0.00	0.00
59	$TiCl_2OCl+Cl \rightleftharpoons TiOCl_3+Cl$	1.00E+13	0.00	0.00
60	$TiCl_2OCl+Cl \rightleftharpoons Cl_2+TiOCl_2$	1.00E+13	0.00	0.00
61	$ClOO+Cl \rightleftharpoons CL_2+O_2$	1.39E+14	0.00	0.00
62	$TiCl_3+ClOO \rightleftharpoons TiCl_4+O_2$	1.00E+13	0.00	0.00
63	$TiCl_4+O_3 \rightleftharpoons TiCl_3+ClO+O_2$	1.00E+13	0.00	53992.1

Table 2.1 (continued): Detailed multistep $TiCl_4$ oxidation chemistry used in this study. The mechanism is based on West et al. [1] and Mehta et al. [2]

No.	Reaction	A ($\mathrm{cm}^3/(\mathrm{s\,mol\,K})$)	n	E_a (cal/mol)
64	$O_3+O \rightleftharpoons 2O_2$	5.47E+12	0.003	4156.9
65	$TiOCl_3+O_3 \rightleftharpoons TiO_2Cl_3+O_2$	1.00E+13	0.00	0.00
66	$TiO_2Cl_2+ClOO \rightleftharpoons TiO_2Cl_3+O_2$	1.00E+13	0.00	0.00
67	$Ti_2O_2Cl_4+Ti_3O_4Cl_4 \rightleftharpoons Ti_5O_6Cl_8$	1.00E+13	0.00	0.00
68	$Ti_2O_2Cl_6+Ti_3O_4Cl_4 \rightleftharpoons Ti_5O_6Cl_8+Cl_2$	1.00E+13	0.00	0.00
69	$Ti_2O_2Cl_5+Ti_3O_4Cl_4 \rightleftharpoons Ti_5O_6Cl_8+Cl$	1.00E+13	0.00	0.00
70	$Ti_5O_6Cl_8+2O_2 \rightleftharpoons 5TiO_2(ru)+4Cl_2$	1.00E+25	0.00	0.00

Table 2.1 (continued): Detailed multistep $TiCl_4$ oxidation chemistry used in this study. The mechanism is based on West et al. [1] and Mehta et al. [2]

2.4.2 Unsteady nucleation model using local precursor concentration

Inclusion of a detailed chemistry mechanism for precursor oxidation faces two problems. First, solving filtered transport equations for the intermediate species in the precursor chemistry faces the same problem as combustion species, in that the filtered source term needs closure. Second, if combustion is described using a flamelet approach, the precursor oxidation should be consistently coupled with the flame chemistry.

The most obvious path is to extend the flamelet approach to precursor oxidation chemistry. However, this is not very straightforward for the following reasons. First, the end result of precursor oxidation is the irreversible formation of solid-phase nanoparticles. Unlike combustion reactions, there exists no equilibrium state for the precursor chemistry, and is not amenable to flamelet assumptions. Second, the time scales associated with precursor oxidation may

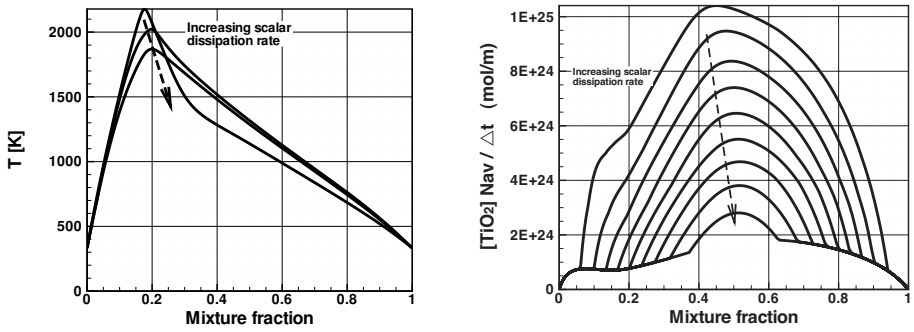

Figure 2.1: Temperature (left) and nucleation rate (right) profiles computed from the flamelet solutions of one dimensional canonical flame.

be very different from combustion chemistry. This can be verified by considering a sample flamelet calculation. Here, the gas-phase chemistry is described using the GRI-Mech 2.11 [90], while the precursor evolution is described using a detailed kinetic mechanism [1] for titanium tetrachloride oxidation and includes the additional reactions described in [2] for nucleation. Fig. 2.1 shows the nucleation rate represented in mixture-fraction coordinates for a range of scalar dissipation rates ($10^{-5}s^{-1}$ to $80s^{-1}$). It can be seen that the irreversible nucleation process occurs over a wide range of mixture-fraction values. This implies that if the nanoparticle formation consisted solely of nucleation, the moments cannot be represented in terms of the local mixture fraction and dissipation rate. Physically, this indicates that the intermediates involved in the nucleation process evolve slowly, while the flame species reach the flamelet limit almost instantaneously.

These problems can be partially alleviated by treating the precursor consumption explicitly through a global transport equation. This allows the ir-

reversible phase transfer through nucleation to be accounted for in the flamelet description. In order to use the flamelet model for precursor evolution, we introduce a global transport equation for the mass fraction of $TiCl_4$:

$$\frac{\partial \overline{\rho}\widetilde{y}_p}{\partial t} + \frac{\partial \overline{\rho}\,\widetilde{u}_j\widetilde{y}_p}{\partial x_j} = \frac{\partial}{\partial x_j}\left(\overline{\rho}(\widetilde{D} + D_t)\frac{\partial \widetilde{y}_p}{\partial x_j}\right) + \widetilde{S}_p, \tag{2.32}$$

where $\widetilde{y}_p$ is the filtered mass fraction of $TiCl_4$ and $\widetilde{S}_p$ is a chemical source term that needs to be provided. This equation essentially accounts for the removal of the precursor from the gas phase. Note that in a multi-step precursor oxidation process, a significant part of the titanium tetrachloride is converted to intermediate species other than titania. The source term for this equation and the nucleation rate are then determined as follows.

At each LES time step, the chemical source term is based on the total titanium-containing species computed from the flamelet table. Note that the flamelet table is constructed using a combined mechanism consisting of detailed hydrocarbon chemistry [90] and detailed $TiCl_4$ oxidation chemistry [1]. Using the local values of the filtered mixture fraction and its variance and dissipation rate, the sum of mass fractions of all titanium species other than titanium tetrachloride is computed. It is then assumed that the complete conversion from the precursor to the titanium species in the look-up table happens within the discrete time determined by the LES numerical time step (which essentially corresponds to instantaneous conversion to the flamelet values). With increasing downstream distance from the inlet, the titanium-chloride concentration will decrease monotonically due to precursor consumption. Consequently, the flamelet-determined rate will have to be adjusted if

insufficient titanium tetrachloride is present to accommodate the tabulated consumption rate. The modeled consumption rate for titanium tetrachloride is thus given by

$$\widetilde{S}_p = -\min\left(\sum_i [\mathrm{Ti}]_i \, W_{\mathrm{Ti}}/\Delta t \, , \, [\mathrm{TiCl_4}] \, W_{\mathrm{TiCl_4}}/\Delta t\right), \tag{2.33}$$

where $\sum_i [\mathrm{Ti}]_i$ is the sum of molar concentrations of all Ti-containing species except $TiCl_4$ and is obtained from the flamelet table. W_i and $W_{\mathrm{TiCl_4}}$ are the molecular weights of titanium and titanium tetrachloride, respectively. $[\mathrm{TiCl_4}]$ is the precursor concentration and is obtained from the transport equation (Eq.(2.32)) as

$$[\mathrm{TiCl_4}] = \overline{\rho}\,\widetilde{y}_p \,/\, W_{\mathrm{TiCl4}} \ \ (\mathrm{mol/m^3}). \tag{2.34}$$

As noted earlier, in order to obtain complete conversion over the time step in the LES code, the source term depends on the time step used to advance the flow solver (Δt). However, formally, this is equivalent to taking the limit $\Delta t \rightarrow 0$ on the right-hand side of Eq.(2.33) so that the precursor mass fraction rests on a manifold consistent with the flamelet table and the inlet concentration without solving for the detailed chemical mechanism in the LES code.

Nucleation of TiO_2 nanoparticles is determined in a similar manner to the precursor source term (Eq.(2.33)). Essentially, the nucleation rate with detailed chemistry is found from the titania concentration obtained from the flamelet table. However, if the titania concentration exceeds the local titanium tetrachloride concentration (i.e. its value is unphysical), then it is limited by

the latter quantity, which is necessary to account for the precursor being removed from the gas phase. Note that the flamelet table is constructed *a priori* and does not have information about the history of the precursor evolution in the flame. Therefore, this step is essential to account for local consumption of the precursor. The nucleation rate used in the LES flow solver is given by

$$J = \min\left([\mathrm{TiO_2}]\, N_{\mathrm{av}}/\Delta t\,,\, [\mathrm{TiCl_4}]\, N_{\mathrm{av}}/\Delta t\right), \tag{2.35}$$

where N_{av} is the Avogadro constant, $[\mathrm{TiO_2}]$ is the molar concentration of $\mathrm{TiO_2}$ obtained from the flamelet table, and $[\mathrm{TiCl_4}]$ is the precursor molar concentration from Eq.(2.34). As explained above, the appearance of Δt in Eq.(2.35) is a model artifact that simply ensures that all of the precursor consumption is correctly accounted for within each time step of the flow solver.

The methodology explained above consists of two implicit assumptions. First, the gas-phase flame is assumed to be unaffected by the presence of the nanoparticle phase and the removal of mass from the gas phase during the formation of nanoparticles. In real flames, the most significant effect will be the radiation effects from the presence of nanoparticles. To remove this assumption, an unsteady flamelet approach could be used but will be computationally expensive. Alternatively, a probability density function (PDF) method [77, 91, 92] could be used. Second, once the larger molecules of oxidated-titanium species are produced, the conversion to solid nanoparticles is assumed to proceed instantaneously [2]. This assumption is justified by the thermodynamic stability of titania nanoparticles containing five or more Ti atoms relative to the other gas-phase precursor species [1].

2.5 Population balance model for nanoparticle dynamics

In flame synthesis, nucleated particles experience further development via coagulation, growth via surface oxidation, and sintering. During these events, significant changes in nanoparticle size, morphology, and quantity (number density) take place and each stage of these processes is strongly affected by various factors including species concentration, turbulent transport, precursor chemistry, and combustion. The goal of this work is to predict the nanoparticle evolution process under such conditions through determination of a number density function (NDF). The NDF is essentially a distribution function in terms of the particle characteristics of interest (e.g. particle size, surface area, and/or mass). It is a function of one or more of those characteristics, each of which serves as an internal coordinate for the particle distribution. The evolution of NDF in flow fields with particle dynamics is described by a population balance equation (PBE). In this study, we develop two different LES-based NDF modeling approaches, using either one or two internal coordinates. Solving the NDF transport equation (discussed below) is non-trivial since the dimensionality of the equation depends on the number on internal coordinates. Even when using a single coordinate, the equation spans 5 dimensions making conventional discretization approaches intractable. Typically, the internal coordinate dimension is handled using an adaptive quadrature scheme, where select moments of the NDF equation are used to reconstruct the NDF function in internal coordinate dimension. In this work, a similar technique

is used. The univariate case is modeled using the quadrature method of moments (QMOM) [93] while the bivariate case is modeled using the conditional QMOM (CQMOM) [3]. Below, numerical details pertaining to both these approaches are discussed.

2.5.1 Univariate model with quadrature method of moments (QMOM)

2.5.1.1 Univariate number density function (NDF) and population balance equation (PBE)

For the univariate NDF, the particle distribution is described by a single internal coordinate. In general, particle size information is one of the most important factors for commercial nanoparticles and, therefore, we use volume-based particle size distribution (PSD) to describe titania particle evolution. With nucleation, surface growth, and aggregation considered, a PBE in terms of the volume-based PSD can be expressed as [34]

$$\begin{aligned}\frac{\partial\, n(v)}{\partial t} + \nabla\cdot\big(\mathbf{u}\, n(v)\big) \;&= \nabla\cdot\big(\Gamma(v,\Phi)\,\nabla n(v)\big)\\ &\quad + J(v,\Phi) f(v_0,\epsilon) - \frac{\partial\, G_v(v,\Phi)\, n(v)}{\partial v}\\ &\quad + \frac{1}{2}\int_0^v \beta(v-v',v')\, n(v-v')\, n(v')\, dv'\\ &\quad - \int_0^\infty \beta(v,v')\, n(v) n(v')\, dv',\end{aligned} \tag{2.36}$$

where $n(v) = n(v;\mathbf{x},t)$ $[\#/m^3]$ is the one-point, one-time PSD in terms of particle volume v. $\Gamma(\phi)$ denotes the mass diffusivity of nanoparticles. The following four terms (from the second to the last terms) in the r.h.s are the source terms for the PBE and, in the order shown in the equation, they indicate the effects of nucleation, surface growth, and birth and death by aggregation,

respectively. The aggregation processes (birth and death) are described by the Brownian collisions between two particles with the sizes v and v' and its frequency kernel is denoted by $\beta(v, v')$. Each of these terms involves the rate expression (nucleation rate J, surface growth rate G, and aggregation rate β) and requires modeling. Models for these rates will be explained shortly. Finally, $f(v_0, \epsilon)$ is a uniform distribution with the size range $[v_0\,(1-\epsilon),\, v_0\,(1+\epsilon)]$, which implies particle formation within this range. ϵ=0.3 is used throughout this study.

$$f(v_0, \epsilon) = \frac{v_0^k((1+\epsilon)^{k+1} - (1-\epsilon)^{k+1})}{2(k+1)\,\epsilon}, \tag{2.37}$$

where v_0 is the volume of a spherical TiO_2 monomer nuclei and its value is set by 1.66×10^{-28} (m^3) [2].

In LES, the above transport equation needs to be filtered to obtain the corresponding LES equation. Assuming the filtering and differentiation and integration commute, the PBE transforms into

$$\begin{aligned}
\frac{\partial\,\overline{n}}{\partial t} + \nabla\cdot\left(\overline{\mathbf{u}}\,\overline{n}\right) \;=\; & \nabla\cdot\left(\overline{\Gamma\,\nabla n}\right) - \nabla\cdot\left(\overline{\mathbf{u}\,n} - \overline{\mathbf{u}}\,\overline{n}\right) \\
& + \overline{J}\,f(v_0, \epsilon) - \frac{\partial\,\overline{G_v n}}{\partial v} \\
& + \frac{1}{2}\int_0^v \overline{\beta(v-v', v')\,n(v-v')\,n(v')}\,dv' \\
& - \int_0^\infty \overline{\beta(v, v')\,n(v)n(v')}\,dv'\,,
\end{aligned} \tag{2.38}$$

where $\overline{n}$ is the filtered PSD and $\overline{\mathbf{u}}$ is the filtered velocity. Note that the velocity is not Favre-filtered. In the LES formulation discussed earlier (Sec. 2.2.2), the velocity field was Faver-filtered. This difference is important in regions of large

density gradient. However, as a first step, this difference is neglected in this work.

The filtered PBE faces a closure problem and this time it poses additional level of difficulty because of the NDF's dependency on the internal coordinate v. Despite of this, some of the open terms in the r.h.s. still can be closed using previously used approaches. For example, the sub-filter number density flux can be closed using

$$(\overline{\mathbf{u}\, n} - \overline{\mathbf{u}}\, \overline{n}) = -D_t \nabla \overline{n}, \tag{2.39}$$

where D_t is the turbulent eddy diffusivity in Eq.(2.27). The diffusion term is closed assuming negligible correlation between particle diffusivity Γ and the spatial NDF gradient.

$$\nabla \cdot \left(\overline{\Gamma\, \nabla n}\right) = \nabla \cdot \left(\overline{\Gamma}\, \nabla \overline{n}\right), \tag{2.40}$$

where $\overline{\Gamma}$ is the filtered particle diffusivity and set to zero because for solid nanoparticles the transport by diffusion is negligibly small compared to turbulent transport.

Although the above terms can be closed, the source terms cannot be closed because they require additional level of closure for the internal coordinate v. For example, the integration and differentiation terms in the r.h.s. in Eq.(2.38) can be closed only when the closure model for the NDF about v is provided. This second level closure is necessary to reduce the high dimensional manifold of the NDF ($n = n(v; \mathbf{x}, t)$) to the same level as other flow field

variables (e.g. $\mathbf{u}(\mathbf{x}, t)$) such that it can be described by a partial differential equation with respect to $(\mathbf{x}, t)$ only. Besides this, the closure model should consider nonlinearity of the source terms. For example, the filtered nucleation source $\overline{J}$ is usually a highly nonliear function of thermochemical state and therefore cannot be simplified further without a closing model. Inherent nonlinearity in the correlation terms such as $\overline{G_v n}$ and $\overline{\beta(v, v')\, n(v) n(v')}$ is also a concern for the closure modeling. Dealing with these nonlinear characteristics of source terms is a challenging topic and tend to require in-depth knowledge about quantum physics and other area of research [18]. One way to deal with the correlation is to introduce a joint PDF of the NDF and thermochemical state with a filtered-density function approach [18, 71, 91, 94] but this is left for the future study. In the present work, the NDF correlations are ignored and simply closed using laminar closure using the filtered quantities .

$$\begin{aligned}
&\overline{J(v, \Phi)} = \; J(\overline{v}, \overline{\Phi}) \\
&\overline{G_v(v, \Phi) n(v)} = \; \overline{G}_v(v, \Phi)\, \overline{n}(v) = \; G_v(\overline{v}, \overline{\Phi}) n(\overline{v}) \\
&\overline{\beta(v, v')\, n(v) n(v')} = \; \overline{\beta}(v, v')\, \overline{n}(v)\, \overline{n}(v') = \; \beta\big(\overline{v}, \overline{v'}\,\big)\, n(\overline{v}) n(\overline{v'}\,)
\end{aligned} \tag{2.41}$$

Although this is a radical assumption in some degree, it can still work as a beginning stage for the LES-based modeling. With Eq.(2.39), (2.40), and

(2.41) applied to the filtered PBE (Eq.(2.38)), we obtain

$$\begin{aligned}\frac{\partial \overline{n}}{\partial t} + \nabla \cdot \left(\widetilde{\mathbf{u}}\, \overline{n}\right) \;=\; & \nabla \cdot \left(D_t \nabla n\right) \\ & + \overline{J}\, f(v_0, \epsilon) - \frac{\partial\, \overline{G}_v\, \overline{n}}{\partial v} \\ & + \frac{1}{2} \int_0^v \overline{\beta}(v - v', v')\, \overline{n}(v - v')\; \overline{n}(v')\, dv' \\ & - \int_0^\infty \overline{\beta}(v, v')\, \overline{n}(v)\; \overline{n}(v')\, dv' \,.\end{aligned} \tag{2.42}$$

Note that $\overline{\mathbf{u}}$ is approximated to $\widetilde{\mathbf{u}}$ by assuming passively transported nanoparticles. The source terms are still open and they need to be closed with respect to the second level closure. In this study, QMOM is used for the purpose. Before discussing how QMOM is applied to the above equation, more details about the the source term modeling are presented below.

2.5.1.2 Modeling of nucleation

As explained in Sec. 2.4.2, the nucleation rate is described by the unsteady kinetics using the flamelet approach with the separately evolving precursor transport equation. Hence, the nucleation rate expression introduced in Eq.(2.35) is used.

$$J = \min\left(\left[\mathrm{TiO_2}\right] N_{\mathrm{av}}/\Delta t\,,\; \left[\mathrm{TiCl_4}\right] N_{\mathrm{av}}/\Delta t\right)$$

2.5.1.3 Modeling of surface reaction and particle growth

Even after the particle formation, consumption of the precursor still proceeds via surface reactions. The precursor molecules colliding with nucleated titania particles are decomposed, leading to absorption and consequent

oxidation of Ti atoms on the particle surface [95]. In this work, this process is described by an one-step based model proposed by Ghoshtagore [96]. According to the model, the growth rate is represented by

$$G_v = \mathrm{k_{surf}}[\mathrm{TiCl_4}]\, N_{\mathrm{av}}\, v_0\, a, \tag{2.43}$$

where $\mathrm{k_{surf}} = 49\exp(-8993/T)$ (m/s) [87] is surface reaction rate constant and $a = \pi m_0(6m_1/(\pi m_0))^{2/3}$ is the surface area concentration. As in nucleation, the precursor concentration is obtained from the precursor transport equation via Eq.(2.34).

2.5.1.4 Modeling of aggregation

Collision between nanoparticles is an important process that is responsible for the formation of structured particle clusters, such as aggregates and agglomerates. Generation as well as breakage of the structured particles are made by these random collision-based particle aggregation. The collision frequency of this aggregation process can be modeled with a Brownian collision kernel. For collisions between two particles with volume v and v', it is given as [34]

$$\beta(v, v') = \frac{2RT}{3\mu N_{\mathrm{av}}}\left(\frac{1}{v^{1/d_f}} + \frac{1}{v'^{\,1/d_f}}\right)\left(v^{1/d_f} + v'^{\,1/d_f}\right), \tag{2.44}$$

where R is the universal gas constant, μ the gas viscosity. In this study μ is approximated to the sum of molecular viscosity and turbulent viscosity (Eq.(2.13)) to account for the effect of turbulence. T is the gas temperature and approximated to the Favre-filtered temperature $\widetilde{T}$. d_f is the fractal

dimension for particle morphology and set to 2.5 assuming diffusion-limited aggregation [97]. Note that the aggregation rate is proportional to the gas-phase temperature, and therefore the aggregation will be significantly faster near the flame surface [2].

2.5.1.5 Quadrature method of moment (QMOM) approach for univariate NDF modeling

In this work, two different techniques for solving the NDF equations are used. The first method, described here, is useful for univariate descriptions such as the one described in the previous section (Sec. 2.5.1).

A PBE (Eq.(2.36)) for titania nanoparticles in a flow field has been solved by several methods including a sectional method [55, 60, 64, 98, 99], Monte-Carlo method with stochastic notional particles [89, 94, 100, 101], and method of moments (MOM) [2, 3, 49, 65, 67, 69, 102–107]. Although detailed PSD information can be obtained from the former two techniques, they often suffer from high computational cost as a large number of sectional bins (sectional methods) or notional particles (Monte-Carlo) is required to ensure sufficient statistical accuracy. Therefore, such a model is likely to be an infeasible option for LES, where a large number of computational grid cells are required. Models based on method of moments (MOM) offer attractive alternatives to these approaches. Here, instead of solving for the full PSD, selected moments of the PSD are tracked. Among MOM-based models, quadrature method of moment (QMOM) has been successfully used for many interesting

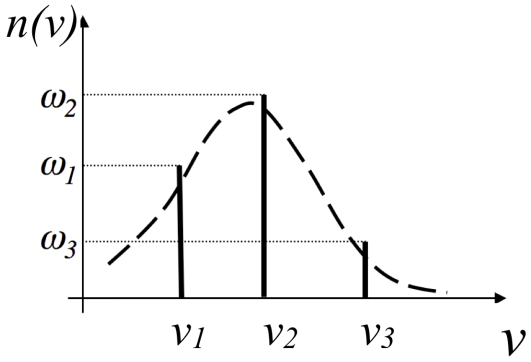

Figure 2.2: An example of a QMOM-approximated particle size distribution using three nodes.

engineering and science applications [54, 58, 66, 100, 107–117]. In QMOM, the PSD is represented by a finite number of delta peaks, each which is described by a weight and abscissa (Fig. 2.2). This method is especially useful for CFD computation of a particle-laiden flow as it requires the solution of a relatively small number of scalars (selected moments of PSD) at each grid point, while successfully providing accurate evaluation for the important statistical quantities of interest. Thus, QMOM provides us a reliable method to solve the PBE while being computationally viable.

In QMOM, the one-point, one-time PSD is approximated as

$$n(v; \mathbf{x},\, t) = \sum_{i=1}^{N} w_i\,(\mathbf{x}, t)\,\delta\,(v - v_i\,(\mathbf{x}, t)), \tag{2.45}$$

where w_i and v_i are the weight and abscissas of the i-th node, respectively. With this approximation, the k-th moment of the volume-based PSD can be evaluated as

$$m_k(v; \mathbf{x},\, t) \equiv \int_0^\infty v^k\, n(v; \mathbf{x},\, t)\, dv = \sum_{i=1}^{N} w_i\,(\mathbf{x}, t)\,(v_i\,(\mathbf{x}, t))^k, \tag{2.46}$$

where N is the number of delta peaks. N=3 is used throughout this study, thereby requiring total of six moments ($k = 0, 1, \ldots, 5$) to determine three weights (w_i, i=1,2,3) and three abscissas (v_i). Note that, for the quadrature approximation, the repeating index i does not imply the summation rule.

These moments have physical significance and can be compared to experimental data. For example, the zero-order moment m_0 is the particle number density (or particle concentration), and m_1 is the particle volume density, which is directly proportional to the mass concentration since the density of the solid particle is constant [2].

Using QMOM, the LES moment transport equation for the k-th moment is derived by applying the QMOM-based moment integration (Eq.(2.46)) to the filtered PBE (Eq.(2.38)).

$$\frac{\partial \overline{m}_k}{\partial t} + \frac{\partial \widetilde{u}_i \overline{m}_k}{\partial x_i} = \frac{\partial}{\partial x_j}\left(D_t \frac{\partial \overline{m}_k}{\partial x_j} \right) + \overline{J}_k + \overline{G}_{v,k} + \overline{B}_k - \overline{D}_k, \tag{2.47}$$

where

$$\begin{aligned}
\overline{J}_k &= \overline{J}\, \frac{v_0^k \left((1+\epsilon)^{k+1} - (1-\epsilon)^{k+1} \right)}{2(k+1)\epsilon}, \\
\overline{G}_{v,k} &= k\, \overline{G}_v\, \overline{m}_{k-1} \\
\overline{B}_k &= \frac{1}{2} \sum_{i=1}^{N} \sum_{j=1}^{N} \beta(\overline{v}_i, \overline{v}_j)\, \overline{w}_i \overline{w}_j \left(\overline{v}_i + \overline{v}_j \right)^{k-1}, \\
\overline{D}_k &= \sum_{i=1}^{N} \sum_{j=1}^{N} \beta(\overline{v}_i, \overline{v}_j)\, \overline{w}_i \overline{w}_j \left(\overline{v}_i^{k-1} + \overline{v}_j^{k-1} \right).
\end{aligned} \tag{2.48}$$

The "filtered" weights and abscissas ($\overline{w}_i$, $\overline{v}_i$) are obtained from a set of the filtered PSD moments utilizing the product-difference algorithm [118]. It is important to note that $\overline{w}_i$ and $\overline{v}_i$ do not correspond to the filtered values

of w_i and v_i since the former are found by inverting the nonlinear QMOM representation of the filtered moment. As mentioned earlier, we neglect the sub-filter correlations between the different weights and abscissas (and hence the moments) when closing the birth and death source terms in Eq.(2.47).

2.5.2 Bivariate expansion of NDF using conditional quadrature method of moment (CQMOM)

The second method used for solving the NDF transport equation is described here. The CQMOM approach is especially useful for bivariate description of the NDF transport equation.

Depending on materials and synthesis conditions, nanoparticles exhibit a wide variety of shapes and morphologies. For example, typical TiO_2 particles show a chained structure consisting of one or more round beads, while ZrO particles show rod-shaped structures as shown in Fig. (2.3). Important particle characteristics such as adsorption and solubility are heavily dependent on the morphology and structure of final particles. Although particle size is one of key parameters to be sought, the size alone is not sufficient enough to fully describe the complicated particle morphology and structure. Description of these important characteristics require additional information such as particle surface area. In modeling of NDF, this additional information is introduced as a new internal coordinate. For a one-point, one-time distribution, a multivariate density function with N internal coordinates (ζ_1, $\zeta_2, \ldots \zeta_N$) is expressed

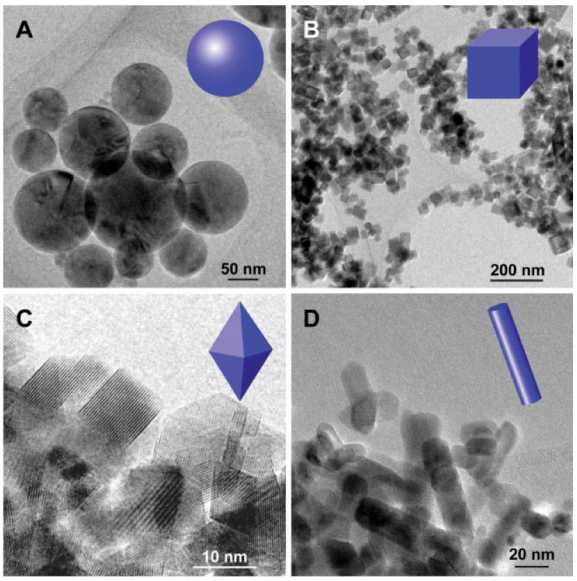

Figure 2.3: Various shapes of nanoparticles made in a flame reactor. A: TiO_2, B: BaF_2, C: CeO_2, D: ZnO. Images are taken from Strobel and Pratsinis [6].

as

$$n = n(\zeta_1, \zeta_2, \ldots \zeta_N; \mathbf{x}, t). \tag{2.49}$$

In this study, we consider bivariate $n(v, a)$ with particle volume as the first coordinate (ζ_1=v) and particle surface area as the second coordinate (ζ_2=a) because these two parameters allow us the prediction of the shape of TiO2 nanoparticle aggregates. In this bivariate description, it is assumed that the primary particles in an aggregate are all equal-sized spheres, which is a reasonable supposition for TiO_2 population (Fig. 2.3). Considering a NDF with the two internal coordinates and sintering process, the population balance

equation (PBE) shown in Eq.(2.36) now becomes

$$\underbrace{\frac{\partial\, n(v,a)}{\partial t}}_{\binom{\text{Rate of}}{\text{change}}} + \underbrace{\nabla\cdot\big(\mathbf{u}\, n(v,a)\big)}_{\text{(Convection)}} =$$
$$\underbrace{\nabla\cdot\big(\Gamma(v,\Phi)\,\nabla n(v,a)\big)}_{\text{(Particle diffusion)}} + \underbrace{J(\Phi)\, f(v_0,a_0,\epsilon_1,\epsilon_2)}_{\text{(Nucelation)}}$$
$$- \underbrace{\frac{\partial}{\partial v}\big(G_v(v,a,\Phi)\, n(v,a)\big)}_{\text{(Volume growth)}} - \underbrace{\frac{\partial}{\partial a}\big(G_a(v,a,\Phi)\, n(v,a)\big)}_{\text{(Area growth)}}$$
$$+ \underbrace{\int_0^a\int_0^v \beta(v-v',v',a-a',a')\, n(v-v',a-a')\, n(v',a')\, dv'\, da'}_{\text{(Aggregation-birth)}}$$
$$- \underbrace{\int_0^\infty\int_0^\infty \beta(v,v',a,a')n(v,a)n(v',a')\, dv'\, da'}_{\text{(Aggregation-death)}}$$
$$+ \underbrace{\frac{\partial}{\partial a}\big(S_a(v,a,\Phi)\, n(v,a)\big)}_{\text{(Sintering)}},$$
(2.50)

where the particle diffusivity Γ is modeled using Brownian diffusion [60].

$$\Gamma(v,\Phi) = k_b T \frac{C_c}{3\mu\pi d}, \tag{2.51}$$

where C_c is the Cunningham correction factor and assumed to be 1. k_b is the Boltzmann constant and d=$(6m_{10}/(\pi m_{00}))^{1/3}$ is the effective collision diameter of an particle aggregate based on volume v. μ and T are fluid viscosity and temperature, respectively. $f(v_0,a_0,\epsilon_1,\epsilon_2)$ is a 2D uniform distribution function for particle formation that is used to describe the nucleated particle

distribution.

$$f(v_0, a_0, \epsilon_1, \epsilon_2) = \frac{v_0^k\, a_0^l \big((1+\epsilon_1)^{k+1} - (1-\epsilon_1)^{k+1}\big)\big((1+\epsilon_2)^{2(l+1)/3} - (1-\epsilon_2)^{2(l-1)/3}\big)}{2\epsilon_1(k+1)(l+1)\big((1+\epsilon_2)^{2/3} - (1-\epsilon_2)^{2/3}\big)}. \tag{2.52}$$

ϵ_1=0.3 and ϵ_1=0.2 are used in present study, meaning that particle nuclei with volume $v \in [v_0\,(1-\epsilon_1),\ v_0\,(1+\epsilon_1)]$ and area $a \in [a_0\,(1-\epsilon_2),\ a_0\,(1+\epsilon_w)]$ are formed with equal possibility. J, β, G_v, G_a, and S_a, are the rates of nucleation, aggregation, volume growth, area growth, and sintering, respectively. Each of the source term rate expressions is explained below in more detail.

2.5.2.1 Modeling of nucleation and volume growth rates

The nucleation rate (J) and volume growth rate (G_v) are identical to the univariate QMOM case and the same equations (Eq.(2.5.1.2) and Eq.(2.43), respectively) are used here.

$$J(\Phi) = \min\left([\mathrm{TiO_2}]\, N_{\mathrm{av}}/\Delta t\,,\ [\mathrm{TiCl_4}]\, N_{\mathrm{av}}/\Delta t\right)\,,$$

$$G_v(v, a, \Phi) = \mathrm{k_{surf}}[\mathrm{TiCl_4}]\, N_{\mathrm{av}}\, v_0\, a\,,$$

where the total particle surface area a is determined from $a = \pi m_{00}(6m_{10}/(\pi m_{00}))^{2/3}$ when G_v is used for moment transport equation (Eq.(2.47) or (2.62)). When it is used for ODE splitting scheme, which is to be discussed in Sec. 4.1, the conditional area node a_{ij} is used for a. This will be discussed with more detail (Sec. 4.1).

2.5.2.2 Modeling of aggregation rate

The Brownian particle collision kernel β for the bivariate NDF is modeled as

$$\beta(v, v', a, a') = \frac{2RT}{3\mu N_{av}} \left(\frac{1}{v^{1/d_f}} + \frac{1}{v'^{1/d'_f}} \right) \left(v^{1/d_f} + v'^{1/d'_f} \right) , \tag{2.53}$$

which appears identical to that of QMOM (Eq.(2.44)) as well. A main difference, however, is that it considers a collision of particles with two different fractal dimensions d_f and d'_f. The fractal dimensions are determined by assuming linear variation from $d_{f_{min}} = 1.7$, (maximum particle surface area) to $d_{f_{min}} = 3.0$ (mnimum particle surface area) [119].

$$d_f(v, a) = \frac{1.3a + d_{f_{max}} a_{\min} - d_{f_{min}} a_{\max}}{a_{\min} - a_{\max}}, \tag{2.54}$$

where $a_{\min} = (36\pi v^2)^{1/3}$ assuming a perfect spherical particle with volume v and $a_{\max} = A_0(v/v_0)$ assuming a particle cluster consisting of primary particles with volume v_0, the volume of a TiO_2 monomer. For constant fractal dimensions of $d_f = d'_f = d_{f,\text{constant}}$, the collision kernel β reduces to Eq.(2.44).

2.5.2.3 Modeling of surface area growth rate

The net change rate of particle surface area is governed by the surface reaction and sintering. Robert et al. [120] have suggested that the surface growth rate of particles is correlated to the volume growth rate as

$$G_a(v, a, \Phi) = G_v(v, a, \Phi) \frac{da}{dv} = G_v(v, a, \Phi) \frac{2}{r}, \tag{2.55}$$

where $r = (a/4\pi)^{1/2}$ is the effective particle radius [119].

2.5.2.4 Modeling of sintering rate

Sintering describes the surface transformation that alters an aggregate of primary particles into an aggregate of fewer particles by minimization of the surface energy of a particle aggregate [7]. In the present study, the point of contact (POC) model proposed by Johannessen et al. [7, 45] is used. As the name implies, the model assumes single contact point among equal-sized spherical primary particles (Fig. 2.4). In this model, the sintering rate is based on the number of contact points, primary particle size, and corresponding characteristic coalescence time. For a particle cluster with two primary particles, the sintering rate is described by a contacting-particle rate expression in the form of S_a=(excessive surface area)/(characteristic time) [7, 121]. If more than two primary particles are subject to coalescence, the rate is dependent on the number of contact points as well and the rate expression in general can be given as S_a=(number of contact points)×(excessive surface area)/(characteristic time). Based on this argument, the sintering rate is modeled as

$$S_a(v, a, \Phi) = \begin{cases} \dfrac{a - a_s}{\tau_f(d_p^*)}, & \text{if } n_p \leq 2 \\ (n_p - 1)\left(\dfrac{0.41 a_p}{\tau_f(d_p)}\right), & \text{if } n_p > 2\,, \end{cases} \tag{2.56}$$

where a_s is the surface area of a perfect spherical particle (i.e. minimum surface area for a single round particle with volume v) and $\tau_f(d)$ is the characteristic sintering time of two identical spherical particles with the diameter d. a_p and d_p are the surface area and the diameter of a single primary particle, respectively, and n_p is the number of them per an aggregate. In the POC

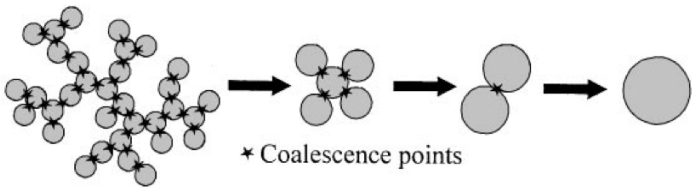

Figure 2.4: Point of contact (POC) model for sintering process. The image is from Johannessen et al [7].

model, these quantities are found as [45, 66]

$$\begin{aligned} &a_s = (36\pi v^2)^{1/3},\ a_p = 36\pi v^2/a^2\,, \\ &d_p^* = (3v/\pi)^{1/3},\ \ d_p = 6v/a\,, \\ &n_p = a^3/(36\pi v^2)\,, \\ &\tau_f(d_p) = k_0\, d_p^{\mathrm{m}} \frac{T}{T_0} \exp\left(\frac{E_A}{R}\left(\frac{1}{T} - \frac{1}{T_0}\right)\right)\,, \end{aligned} \tag{2.57}$$

where k_0=1×10^{28} (m^{-4}) is a pre-exponential term at T_0=1400 (K) and m=4 is an exponential power for two identical contacting particles with size d_p. E_A=1.5×10^5 (J/mol) is the activation energy and R is the gas constant.

2.5.2.5 CQMOM numerical approach for bivariate NDF transport equation

A bivariate NDF involves a 6-dimensional transport equation and requires the handling of the additional internal coordinate as opposed to the univariate case. The QMOM method is not directly applicable since the product-difference algorithm used to obtain the weights and abscissas is not extendible to multivariate NDFs. To overcome this challenge, we use the newly introduced method called conditional quadrature method of moments (CQMOM)

proposed by Cheng and Fox [3]. CQMOM is similar to QMOM in that it utilizes quadrature-approximated delta functions to model the NDF and uses the production-difference algorithm to recover the weights and abscissas information from selected NDF moments. The main idea of CQMOM is to add a new internal coordinate, being conditioned on a pre-existing internal coordinate. In the bivariate case, the second coordinate a is conditioned on the first coordinate v. From this, NDF in CQMOM can be represented as

$$n(v, a; \mathbf{x}, t) = n_V(v)\, n_{A/V}(a|v) = \sum_{i=1}^{N_v} \sum_{j=1}^{N_a} w_i\, w_{ij}\, \delta(v - v_i)\, \delta(a - a_{ij}), \quad (2.58)$$

where N_v and N_a are the number of nodes in volume and area directions, respectively. w_i and v_i are the weight and abscissa in the first internal coordinate (volume) and w_{ij} and a_{ij} are the weight and abscissa of the second internal coordinate (area), respectively. The first subscript i in w_{ij} and a_{ij} indicates the j-th node of the second coordinate is conditioned on the i-th node on the first coordinate. As in QMOM, these weights and abscissas are determined using a select set of NDF moments. In CQMOM, the general NDF moment m_{kl} with the k-th order in volume and the l-th order in area is defined as

$$m_{kl} \equiv \int_0^\infty \int_0^\infty v^k\, a^l\, n(v, a)\, dv\, da = \sum_{i=1}^{N_v} \sum_{j=1}^{N_a} w_i\, w_{ij}\, v_i^k\, a_{ij}^l, \quad (2.59)$$

The NDF moments are obtained by solving the moment transport equations. The filtered CQMOM moment transport equations are found in a similar manner to that used for the univariate QMOM moment transport equation (Eq.(2.47)). First, we obtain the filtered transport equation for n by applying

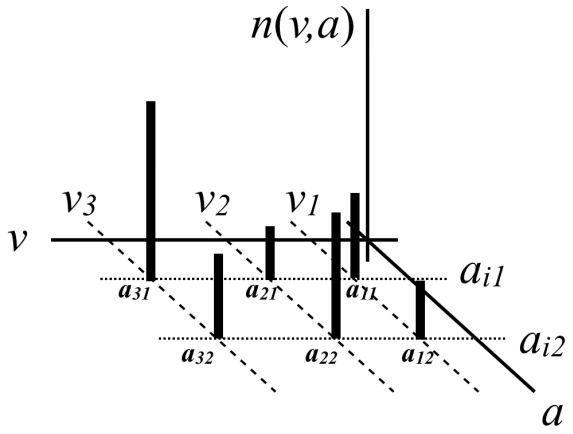

Figure 2.5: An exemple of a CQMOM-approximated bivariate particle size distribution $n(v,a)$ using three volume nodes (N_v=3) and two conditional area nodes (N_a=2).

the filtering operation (Sec. 2.2.1) . Similar to the QMOM case, this procedure yields several unclosed terms.

$$\begin{aligned}\frac{\partial \overline{n}}{\partial t}+\nabla\cdot\left(\overline{\mathbf{u}}\,\overline{n}\right) &= \nabla\cdot\left(\overline{\Gamma\nabla n}\right)-\nabla\cdot\left(\overline{\mathbf{u}\,n}-\overline{\mathbf{u}}\,\overline{n}\right)\\ &+\overline{J}_{kl}\,f(v_0,a_0,\epsilon_1,\epsilon_2)-\frac{\partial\overline{G_v n}}{\partial v}-\frac{\partial\overline{G_a n}}{\partial a}\\ &+\int_0^a\int_0^v \overline{\beta(v-v',v',a-a',a')\,n(v-v',a-a')\,n(v',a')}\,dv'\,da'\\ &-\int_0^\infty\int_0^\infty \overline{\beta(v,v',a,a')\,n(v,a)n(v',a')\,dv'\,da'}+\frac{\partial\overline{S_a n}}{\partial a},\end{aligned} \tag{2.60}$$

The unclosed terms are modeled similat to the QMOM case. For example, identical closures are used to close the sub-filter NDF flux term (Eq.(2.39)) and particle diffusion term (Eq.(2.40)). Then the filtered moment transport equation for m_{kl} is found by integrating the NDF equation over volume and surface area dimensions as follows:

$$\int\int v^k a^l \times (\text{Eq.}(2.60))dv\,da \tag{2.61}$$

by assuming negligible correlations and laminar closure. The resulting filtered LES transport equation can be written as follows:

$$\begin{aligned}\frac{\partial \overline{m}_{kl}}{\partial t} + \nabla \cdot \left(\widetilde{\mathbf{u}}\, \overline{m}_{kl}\right) &= \nabla \cdot \left(\left(\overline{\Gamma} + D_t\right) \nabla\, \overline{m}_{kl}\right) \\ &\quad + \overline{J}_{kl} + \overline{G}_{v,kl} + \overline{G}_{a,kl} + \overline{B}_{kl} - \overline{D}_{kl} - \overline{S}_{a,kl},\end{aligned} \tag{2.62}$$

where

$$\begin{aligned}
\overline{J}_{kl} &= \overline{J}\, \frac{v_0^k\, a_0^l \left((1+\epsilon_1)^{k+1} - (1-\epsilon_1)^{k+1}\right)\left((1+\epsilon_2)^{2(l+1)/3} - (1-\epsilon_2)^{2(l-1)/3}\right)}{2\epsilon_1 (k+1)(l+1)\left((1+\epsilon_2)^{2/3} - (1-\epsilon_2)^{2/3}\right)}, \\
\overline{G}_{v,kl} &= \sum_{i=1}^{N_v} \sum_{j=1}^{N_a} k\, \overline{w}_i \overline{w}_{ij}\, \overline{v}_i^{k-1}\, \overline{a}_{ij}^{l}\, \overline{G}_v, \\
\overline{G}_{a,kl} &= \sum_{i=1}^{N_v} \sum_{j=1}^{N_a} l\, \overline{w}_i \overline{w}_{ij}\, \overline{v}_i^{k}\, \overline{a}_{ij}^{l-1}\, \overline{G}_a, \\
\overline{B}_{kl} &= \frac{1}{2} \sum_{i=1}^{N_v} \sum_{j=1}^{N_a} \sum_{m=1}^{N_v} \sum_{n=1}^{N_a} \beta(\overline{v}_i, \overline{a}_{ij}, \overline{v}_m, \overline{a}_{mn})\, \overline{w}_i \overline{w}_{ij}\, \overline{w}_m \overline{w}_{mn} (\overline{v}_i + \overline{v}_m)^k\, (\overline{a}_{ij} + \overline{a}_{mn})^l, \\
\overline{D}_{kl} &= \frac{1}{2} \sum_{i=1}^{N_v} \sum_{j=1}^{N_a} \sum_{m=1}^{N_v} \sum_{n=1}^{N_a} \beta(\overline{v}_i, \overline{a}_{ij}, \overline{v}_m, \overline{a}_{mn})\, \overline{w}_i \overline{w}_{ij}\, \overline{w}_m \overline{w}_{mn} \left(\overline{v}_i^k\, \overline{a}_{ij}^l + \overline{v}_m^k\, \overline{a}_{mn}^l\right), \\
\overline{S}_{a,kl} &= \sum_{i=1}^{N_v} \sum_{j=1}^{N_a} l\, \overline{w}_i \overline{w}_{ij}\, \overline{v}_i^{k}\, \overline{a}_{ij}^{l-1}\, \overline{S}_a.
\end{aligned} \tag{2.63}$$

As in QMOM, the source terms are closed using a laminar chemistry assumption. Again, it is important to note that the "filtered" weights and abscissas in the above equations ($\overline{w}$, $\overline{v}$, and $\overline{a}$) are computed from the filtered moments and therefore they are not equivalent to the filtered weight and abscissa values. With the moment information known from Eq.(2.62), the weights and abscissas are found by using the following steps [3]. The filtering notation is removed for brevity.

1. First, find the volume node weights and abscissas ($w_1, \ldots, w_{N_v}$ and v_1, $\ldots$, v_{N_v}) from $2N_v$ number of the pure volume moments (m_{00}, m_{10}, $\ldots$, $m_{2(N_v-1),0}$) via the product-difference algorithm. This procedure is identical to that of the univariate QMOM case (Sec. 2.5.1.5).

2. Once the volume nodes are found, the conditional area node information can be determined by following the substeps listed below:

   (a) Using the CQMOM definition of m_{kl}

   $$m_{kl} = \sum_{i=1}^{N_v} \sum_{j=1}^{N_a} w_i \, w_{ij} \, v_i^k \, a_{ij}^l = \sum_{i=1}^{N_v} w_i \, v_i^k \, A_{il} \, , \tag{2.64}$$

   construct a linear equation system for $A_{il} = \sum_{j=1}^{N_a} w_{ij} a_{ij}^l$, the l-th area moment for the i-th volume node, and solve it for each $l = 1, 2, \ldots, 2N_a - 1$. For example, for $l = 1$ when $N_v = 3$, following linear system is constructed with a Vandermonde matrix:

   $$\begin{bmatrix} m_{01} \\ m_{11} \\ m_{21} \end{bmatrix} = \begin{bmatrix} 1 & 1 & 1 \\ v_1 & v_2 & v_3 \\ v_1^2 & v_2^2 & v_3^2 \end{bmatrix} \begin{bmatrix} w_1 & & \\ & w_2 & \\ & & w_3 \end{bmatrix} \begin{bmatrix} A_{11} \\ A_{21} \\ A_{31} \end{bmatrix}$$
   $$\implies \begin{bmatrix} A_{11} \\ A_{21} \\ A_{31} \end{bmatrix} = \begin{bmatrix} 1/w_1 & & \\ & 1/w_2 & \\ & & 1/w_3 \end{bmatrix} \begin{bmatrix} 1 & 1 & 1 \\ v_1 & v_2 & v_3 \\ v_1^2 & v_2^2 & v_3^2 \end{bmatrix}^{-1} \begin{bmatrix} m_{01} \\ m_{11} \\ m_{21} \end{bmatrix} . \tag{2.65}$$

   (b) At each volume node i, retrieve the conditional weights and abscissas (w_{ij}, a_{ij}) from $A_{il} = \sum_{j=1}^{N_a} w_{ij} a_{ij}^l$ using the product difference algorithm.

From the above procedure, it is clear that the goal of CQMOM is to seek a QMOM-approximated area distribution ($w_{i1}, w_{i2}, \ldots, w_{ij}$ and $a_{i1}, a_{i2}, \ldots, a_{ij}$) for each volume node (w_i, v_i), which is computed ahead of time by using ordinary QMOM. Consequently, the product difference algorithm must be applied at each volume node to determine the conditional area nodes. As a result, in CQMOM, the total number of moments required is only $2N_v + 2N_v(N_a - 1)$, where $2\,N_v$ is the number of pure volume moments needed to find the volume nodes (w_i, v_i), and $2N_v(N_a - 1)$ is the number of pure area and mixed volume-area moments needed to find the conditional area nodes (w_{ij}, a_{ij}). An example moment set required for a case with N_v=N_a=3 is presented in Table. (2.2). Compared to the univariate case, the cost of bivariate expansion is equal to $2N_v(N_a - 1)$ additional number of equations. which does not impose a large cost since scalar transport equations are relatively inexpensive compared to momentum equations. Besides, CQMOM takes advantage of QMOM routines such as the product difference algorithm and requires no additional modifications for the bivariate case. In other words, CQMOM offers a very attractive approach for a low-cost expansion to bivariate NDF modeling as compared to the univariate QMOM. In this study, three volume nodes and one conditional area node is used. This particular setup requires a total of nine NDF moments, six for the pure volume moments ($m_{00}, m_{10}, \ldots, m_{50}$, which are the same for the single variable QMOM case), and three for the area or volume-area mixed moments (m_{01}, m_{11}, m_{21}). Compared to QMOM, only three additional equations are solved and hence the computational cost increase is rather mild for

m_{00}	m_{01}	m_{02}	m_{03}	m_{04}	m_{05}	
m_{10}	m_{11}	m_{12}	m_{13}	m_{14}	m_{15}	
m_{20}	m_{21}	m_{22}	m_{23}	m_{24}	m_{25}	
m_{30}	$\downarrow$	$\downarrow$	$\downarrow$	$\downarrow$	$\downarrow$	
m_{40}	A_{11}	A_{12}	A_{13}	A_{14}	A_{15}	$\rightarrow \{w_{1j}, a_{1j}\}$
m_{50}	A_{21}	A_{22}	A_{23}	A_{24}	A_{25}	$\rightarrow \{w_{2j}, a_{2j}\}$
$\downarrow$	A_{31}	A_{32}	A_{33}	A_{34}	A_{35}	$\rightarrow \{w_{3j}, a_{3j}\}$
$\{w_i, a_i\}$						

Table 2.2: An example of the required list of CQMOM moments for bivariate NDF modeling with N_v=N_a=3 [3].

the accrued benefits of bivariate modeling.

Chapter 3

Simulation of a TiO_2 flame-synthesis experiment using QMOM

Two types of the multiscale LES models with univariate QMOM and bivariate CQMOM are used to simulate TiO_2 nanoparticle synthesis in a turbulent diffusion flame that was studied experimentally by Pratsinis et al. [4]. In this chapter, the details of the simulation and the numerical methods for QMOM-based simulation are provided. The discussion of results will be presented in Section 3.3

3.1 Flame configuration

In this study, the flame configuration corresponding to Flame D in Pratsinis et al. [4] is used. A schematic of the reactor geometry is shown in Fig. 3.1. The reactor consists of a central jet (4mm inner diameter) and two surrounding annular rings (1 mm) with three surrounding walls (1 mm thick). Issuing from the central jet is a mixture of vaporized precursor ($TiCl_4$) and fuel (CH_4) diluted in argon. The oxidizer (air) is delivered from the second annular ring into the flame. No working fluid is issued from the inner ring except a minimal amount of air, just enough to prevent burner clogging from

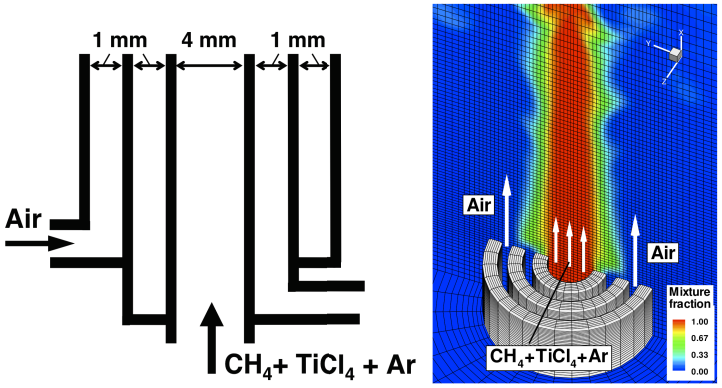

Figure 3.1: Configuration of the flame reactor (left) and part of the cylindrical grid-cell system (right) used for the simulation of flame reactor. Background contour shown is the mixture-fraction variable. All walls are 1 mm-thick.

Fluid	Flow rate
CH_4	312 ml/min
$TiCl_4$	5.8×10^{-4} mol/min
Ar	250 ml/min
Air	3800 ml/min

Table 3.1: Flow rates of the ETH Zürich flame reactor [4]

nanoparticle deposition. In the simulation, this is accounted for by supplying a small amount of air, which is less than 3% of the main oxidizer stream from the second annular ring. The flow conditions used are shown in Table 3.1. The mixture-fraction variable is defined such that its value is 1 for the central precursor-fuel stream and 0 for the coflow air stream and the ambient fluid. This configuration constitutes a conventional non-premixed diffusion flame.

3.2 Simulation setup

The LES-based model is solved in cylindrical coordinates using a computational domain with 45D in the axial direction and 30D in the radial direction, where D is the main jet diameter (4 mm). A structured cylindrical grid system with 256×112×32 finite-volume cells is used for the LES computation. A schematic of the flow configuration as well as the computational mesh used is shown in Fig. 3.1. Note that the grid cells are heavily clustered near the nozzle exit in order to capture the turbulent jet dynamics accurately as well as to adequately resolve the shear layer between the jets. The simulation is run for approximately two residence times, where a residence time is calculated based on the inlet bulk jet velocity and the computational domain length. This time is found to be sufficient to reach statistical stationarity. Then, statistics of the flow are collected for three additional residence times. Using MPI-based parallel computing systems, the flow code is run on 128-512 processors. On 256 processors, the simulation takes approximately takes a five days.

3.2.1 Numerical methods

The LES transport equations are solved using a low-Mach-number, variable-density approach [84, 122]. A second-order, energy-conserving scheme is used to discretize the momentum equations. The scalar equations, including the moment transport equations, are solved using the bounded third-order upwind QUICK scheme [123]. Time-consistent advancement of the momentum and scalar equations is made utilizing a predictor-corrector-based pressure-

solving scheme. Here, the density is estimated from the mixture-fraction equation. The density is then used in the momentum equation to obtain the interim velocities, which are corrected by continuity enforcement. More details of the flow solver can be found in [124].

The non-premixed flame structures are described by the steady laminar flamelet model. Here, a look-up table is made from the solution of the flamelet equations prior to the LES computations. The flamelet solutions are found using the FlameMaster code [86] by solving one-dimensional counter diffusion flames. A detailed hydrocarbon chemistry (GRI-2.11, [90]) is used to describe the flame-related chemical reactions. For the oxidation process of titania tetrachloride, a detailed chemical mechanism proposed by [2] is used. The mechanism includes 34 species and 70 reactions and is extended from the mechanism made by [1] to account for the nuclei that consist of five or more Ti atoms at temperature higher than 600 K. The resulting comprehensive chemistry consists of 76 species and 348 reactions and used to create the flamelet table. The flamelet table stores the concentrations needed to compute the precursor source term (Eq.(2.33)). The three dimensions of the flamelet table (mixture fraction, mixture-fraction variance, and the mixture-fraction-variance dissipation rate) are finely discretized using 200–500 points in each direction to minimize interpolation-related errors. In the given experimental flow configuration, flame extinction is observed near a scalar dissipation rate (χ_{ext}) of 90 s^{-1}. The flamelet table is constructed from multiple flamelet solutions, which are obtained by gradually increasing the mixture-fraction dissipation

rate χ from a small value close to zero to χ_{ext}. As explained in Sec. 2.3.1, the subfilter distribution of mixture fraction is modeled using a β-function, which is parameterized using the filtered mixture fraction and its variance. The look-up table constructed in this manner contains all of the species mass fractions as well as density, temperature, and the physical properties of the fluid, such as viscosity and diffusivity.

In this study, indirect solutions of the PBE are sought by tracking the selected moments of the PSD and applying QMOM to compute the source terms. The transport equations for the six integer moments (Eq.(2.47)) are solved by utilizing the scalar scheme employed in the LES solver. The moment equations contain source terms corresponding to nucleation and aggregation, which are highly sensitive to the local gas-phase composition as well as the moments of the PBE. Invariably, these source terms are numerically stiff, requiring very small time steps to be used. To remedy this problem, a time-splitting technique is employed in our code. At each time step, the following set of ordinary differential equations are solved for each computational cell:

$$\overline{m^*}_k^{\,t+\Delta t} = \int_0^{\Delta t} \left(\overline{J}_k + \overline{B}_k - \overline{D}_k\right) dt, \tag{3.1}$$

for $k = 1, \cdots, 6$, where m^* denotes an intermediate moment value and Δt is the LES time step. The numerical integration is carried out using a stiff ODE solver [125] with initial conditions at $t = 0$ set as $\overline{m}_k$ at the beginning of the time step. The source term to be used in Eq.(2.47) is then determined as follows:

$$S_k^{total} = \frac{\overline{m^*}_k - \overline{m}_k}{\Delta t}, \tag{3.2}$$

where S_k^{total} is the sum of all source terms due to nucleation and aggregation for the $k-$th moment. The ODEs are solved at the start of the time step, and the source term computed above is then used when advancing the moment equations in space (Eq.(2.47)). The numerical integration of these ODEs is computationally expensive, and accounts for nearly 50% of the total computational time.

3.3 Results and discussion

3.3.1 Flame characteristics

Fig. 3.2 shows the mixture fraction, and temperature contours as well as the time-averaged streamwise velocity contours. Since the annular spacing next to the central jet does not issue any substantial mass, it acts as a bluff-body, setting up a small recirculation zone over the top of this spacing. This feature is prominent in the time-averaged velocity profiles that show the recirculation bubble. This flow feature provides entrainment and mixing of the coflow, resulting in a stable flame anchored to the nozzle exit. The Reynolds numbers of the main jet and coflow are ∼200 and ∼1000, respectively, which make the flow only mildly turbulent. Consequently, the central jet breakdown is more gradual, with complete breakdown seen only near $x/D = 10$. The temperature snapshot shows a high-temperature zone in the shear layer between the main fuel jet and the coflow, corresponding to regions that contain near-stoichiometric mixture fraction. In Fig. 3.2, it can be seen that the maximum temperature occurs around the stoichiometric contour as dictated by the

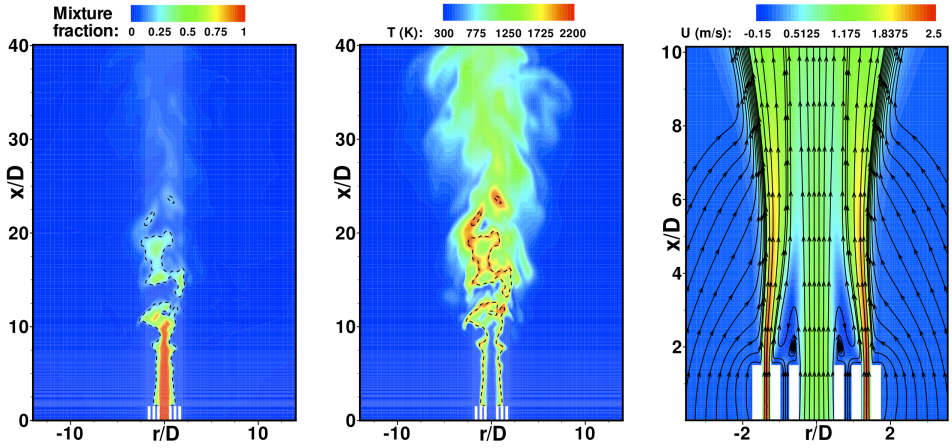

Figure 3.2: Instantaneous snapshots of (left) temperature, (middle) mixture fraction, and (right) close-up of the mean axial velocity with stream lines superimposed. The dotted lines indicate the location of the stoichiometric mixture fraction.

flamelet model. Further downstream, dilution of the fuel jet with the coflow pushes the mixture fraction below stoichiometric values and reduces the flame temperature.

Fig. 3.3 shows the time-averaged mixture fraction and temperature along the centerline. The mixture-fraction values confirm that the jet breakdown occurs around $x/D = 10$. Although the instantaneous temperatures are as high as 2100 K, the time-averaged temperature peaks at 1327 K, implying that the large-scale unsteadiness in the flame moves the stoichiometric flame surface with time. This ability to predict the large-scale motions is an important feature of LES. Table 3.2 shows the experimentally measured and computed flame lengths, defined as the location of the peak temperature measured along the centerline. LES is able to predict both the location of the peak

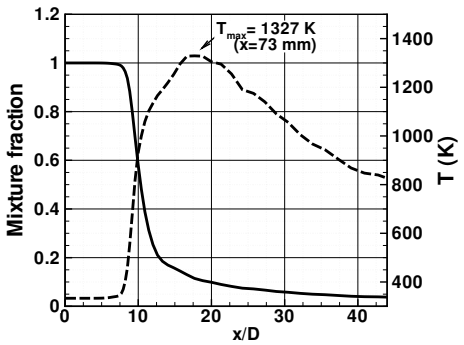

Figure 3.3: Mean mixture fraction and temperature along the centerline.

	LES	Exp.
Flame length	73 mm	75 mm
T_{max}	1327 K	1294 K

Table 3.2: Flame length and temperature obtained from LES and experiments [4].

value and the peak temperature quite accurately.

3.3.2 Evolution of nanoparticles

The evolution of the gas-phase precursors is shown in Fig. 3.4 and is obtained by solving the precursor transport equation (Eq.(2.32)). It can be seen that the precursor is consumed very rapidly close to the nozzle exit. Based on Eq.(2.33), the consumption of titanium tetrachloride depends on the oxidation kinetics from the flamelet table. Fig. 3.4 also shows the sum of the titanium species that is used in the computation of the precursor source term. This is obtained directly from the flamelet table. It can be seen that the titanium tetrachloride oxidation starts on the rich side of the flame, where mixture-

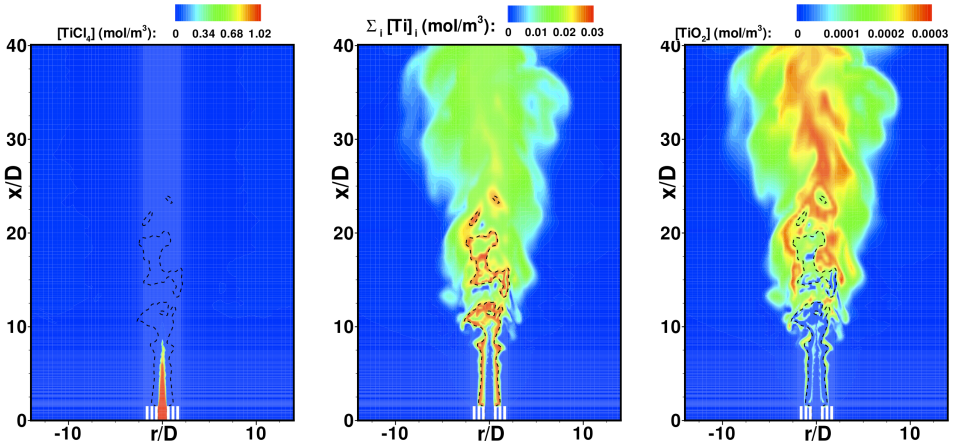

Figure 3.4: Instantaneous contour plots of (left) the precursor concentration, (middle) Ti-atom concentration obtained from the Ti-containing species, and (right) TiO_2 concentration with the the dotted lines indicating the stoichiometric mixture composition.

fraction values are larger than the stoichiometric value. Nearly all of the precursor is consumed before the jet reaches the stoichiometric flame surface. It should be noted that the nucleation model proposed here will limit particle formation to regions where there is non-zero precursor concentration. Fig. 3.4 shows the titania concentration obtained from the flamelet table. Since the flamelet table is not aware of the total precursor consumption and treats each point in the computational domain as a pure diffusion flame, there is significant titania concentration very far downstream. However, particle nucleation is suppressed at these locations since the precursor concentration obtained from the transport equation (Eq.(2.32)) is negligible.

Fig. 3.5 shows the particle nucleation rate and the evolution of the particle number density close to the nozzle exit. As expected, the number

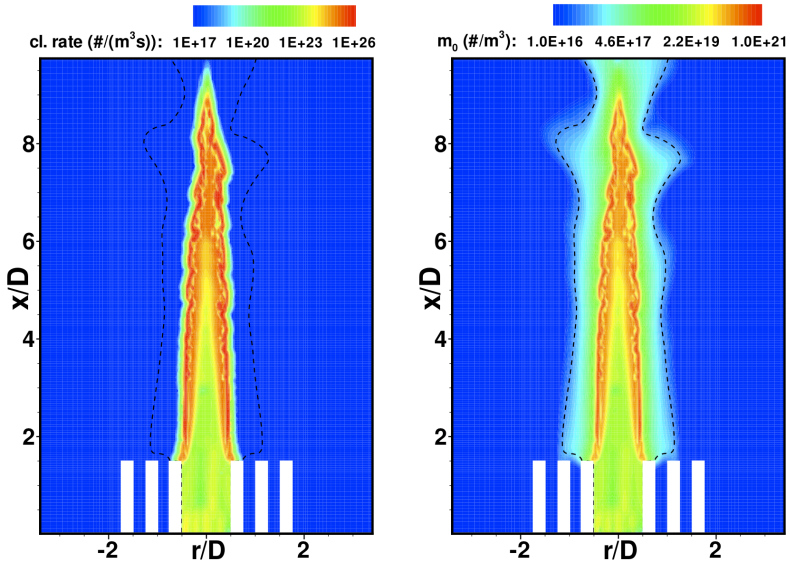

Figure 3.5: Instantaneous contour plots of (left) nucleation rate and (right) particle number density obtained from the LES computation with the dotted lines showing the stoichiometric mixture fraction.

density peaks at locations where the precursor concentration drops to near zero values. The nucleation rate shows that significant nucleation occurs on the very rich side of the flame, indicating that modestly high temperatures are sufficient to oxidize the precursor. Outside of this region, nucleation rates drop to very small values due to the near total consumption of precursor. Fig. 3.6 shows an instantaneous snapshot of particle size and number density. The particle diameter has been calculated based on Mehta et al. as [2]

$$D_p = D_0 \left(\frac{m_1}{m_0 \; v_0} \right)^{1/d_f} , \tag{3.3}$$

where D_0 is the corresponding particle size to the reference particle volume v_0.

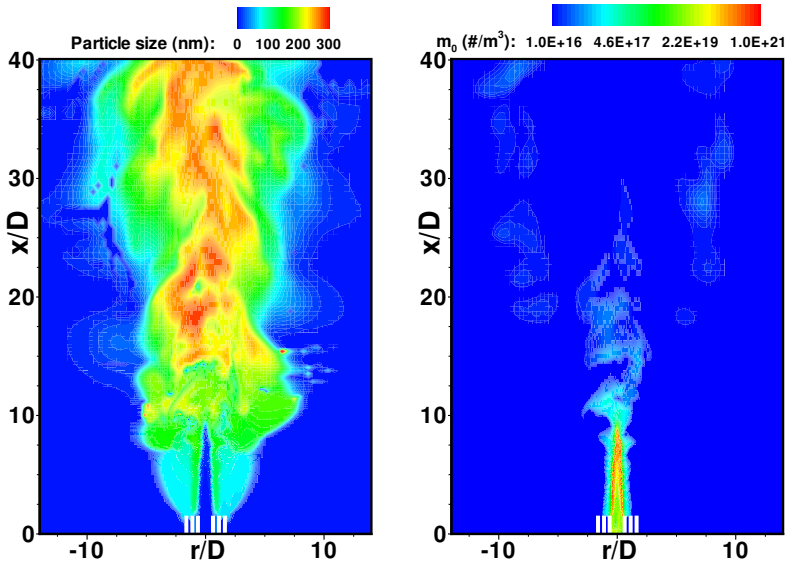

Figure 3.6: Instantaneous snapshots of (left) particle size and (right) particle population density obtained from the LES computation.

The nucleation process produces nanoparticles of size ∼10 nm near the burner exit. The high number density in the vicinity of the nucleation region combined with the high temperature as the nanoparticles pass through the flame result in extensive aggregation that increases the size of the particles while reducing the number density. It can be seen that the major increase in size occurs in regions with relatively high temperatures, since aggregation rates are directly proportional to the gas-phase temperature. As the nanoparticles move downstream, dilution with the coflow decreases the nanoparticle number density and the collision rates, leading to decreased aggregation rates. Fig. 3.7 shows the time-averaged centerline evolution of number density and nanoparticle size. The number density drops significantly around $x/D = 10$, where the

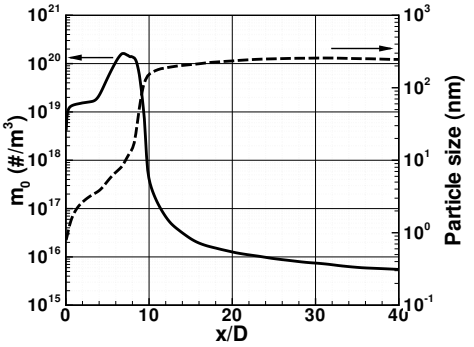

Figure 3.7: Mean particle population density and particle size along the centerline obtained from the LES computation.

fuel jet breaks down fully leading to increased mixing and reduced temperatures. Consequently, nanoparticle sizes reach a maximum of roughly 110 nm at around $x/D = 15$, but no significant further growth is seen downstream.

The time-averaged nanoparticle diameter plot (Fig. 3.8) shows that the particle diameter is large near the centerline but drops off with radial distance. Aggregation seems to be most active at the flame tip, where high temperatures combined with high number density drive the collisional process. The larger nanoparticles are formed closer to the centerline, and move along streamlines that weakly spread along the radial directions. Consequently, larger nanoparticles are not found near the outer edge of the flame. This study also demonstrates that nanoparticle size is almost independent of the reactor length for the investigated flow configuration, and that both nucleation and aggregation occur very close to the nozzle exit.

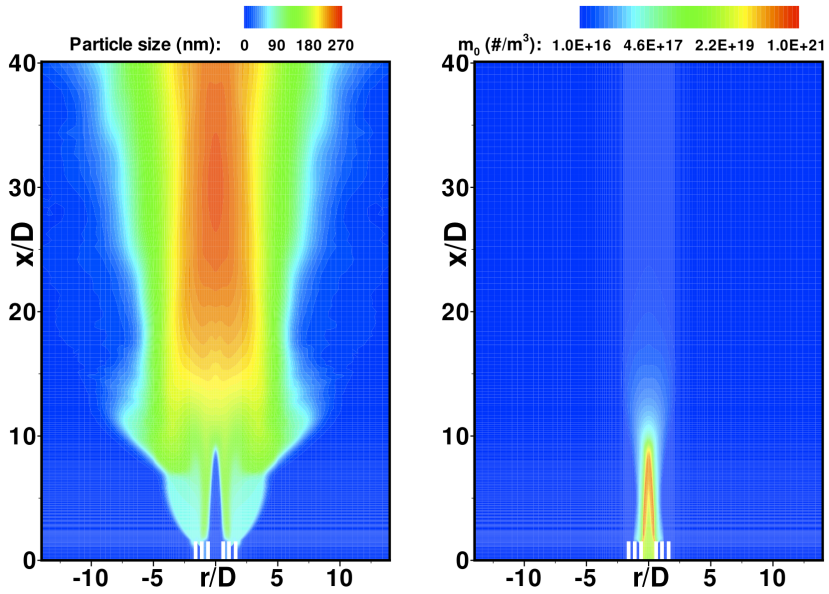

Figure 3.8: Mean particle size (left) and population density (right) from LES computation.

3.3.3 Evolution of particle size distribution

The size distribution of the nanoparticles can be further understood in terms of the PSD. Fig. 3.9 shows variation of the time-averaged weights and abscissas along the centerline. The PSD is initially a unimodal distribution, indicating the region where nucleation is active. As aggregation becomes important, the PSD shifts towards larger nanoparticle diameters. The weights corresponding to the smaller abscissas decrease while the weight of the largest abscissa increases in value. As seen in the number density and nanoparticle size plots, there is an asymptotic approach to steady-state values with downstream location, and there is very little change in the PSD beyond $x/D = 15$ for this flow configuration.

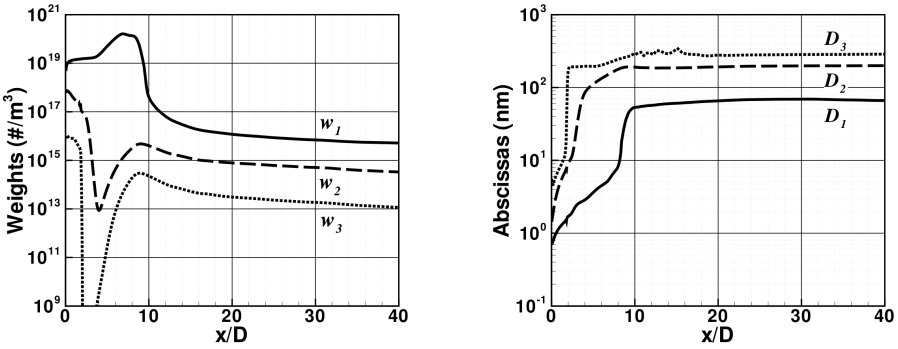

Figure 3.9: Variation of (left) mean weights and (right) abscissas along the centerline as a function of axial distance. The size, D_i, is based on the corresponding volume abscissas.

3.3.4 Comparison against the experiment

Important particle characteristics including the size of nanoparticles and specific surface area (SSA) are available from the experiment. The SSA is defined as total particle surface area per unit mass of nanoparticles and therefore can be formulated using the PSD volume moments.

$$\mathrm{SSA} = \frac{\left(\pi D_p^2\right) \times m_0}{\rho_{\mathrm{TiO_2}}\, m_1}, \tag{3.4}$$

where D_p is from Eq.(3.3). Table 3.3 shows the radially averaged values of the particle size and the SSA from the LES computation and the corresponding experimental data. The LES values are taken at $x/D = 30$, at which the titania particles were captured by a collecting filter in the actual synthesis. Compared to the experiment, LES makes a very good prediction on the particle size. However, the SSA is significantly overpredicted. This is because surface reaction and sintering models are not considered in the current LES model and

	LES	Exp.
Particle size	108 nm	100∼105 nm
SSA	129 m^2/g	17 m^2/g

Table 3.3: Comparison of LES results of particle size and specific surface area (SSA) against experimental data [4]

therefore particles can only form long chain-like structures with the primary particles, which exhibit high area to volume ratio.

3.4 Conclusions

A detailed LES-based computational model for simulating flame synthesis of nanoparticles has been developed and tested with univariate volume-based QMOM. The new methodology uses a comprehensive chemical kinetic mechanism for gas-phase combustion as well as precursor oxidation. An unsteady model for nucleation is proposed that consistently couples the flamelet-based gas-phase combustion description with the multi-species oxidation process. This computational model is then used to simulate a flame-based titania synthesis experiment. The LES computations are able to predict the large-scale unsteadiness in the flow accurately, leading to accurate predictions of the peak flame temperature measured in the experiments. The simulations indicate that precursor oxidation occurs on the rich side of the flame, at temperatures lower than that observed at stoichiometric conditions. The nucleated particles pass through the flame front leading to intense aggregation that reduces the number density while increasing the particle diameter by an order

of magnitude. Aggregation is quickly quenched by the turbulent breakdown of the fuel jet that leads to a reduction in gas temperature. Consequently, particle sizes do not change beyond the aggregation zone. Comparison with experiments indicate that the particle sizes are predicted well by the simulations but the surface area from computations are significantly higher. The addition of sintering and surface growth models will improve these results. In the next section, bivariate NDF modeling using CQMOM with sintering effect is discussed.

Chapter 4

Simulation of a TiO_2 flame-synthesis experiment using CQMOM

In this section, results from the CQMOM approach for modeling nanoparticles is presented. To recap, the CQMOM method allows the use of bivariate NDFs. In this work, the volume-area NDF is used to characterize the nanoparticle population. The use of area as an internal coordinate further allows the addition of particle sintering in high temperature regions. Sintering only affects the surface area but the particle mass, and consequently volume, does not change. The CQMOM model uses three volume nodes (N_v=3) and one conditional area node (N_a=1), requiring a total of nine NDF moments for the complete description. The evolution equations and the choice of moments were discussed in Sec. 2.5.2. These moment equations are solved in the LES framework along with the flamelet-based nucleation model described in Sec. 2.4. Based on the moment set, the weights, volume abscissas, and conditional area nodes are obtained using the procedure explained in Sec. 2.5.2.5.

4.1 Sintering source and operator-split source term integration

Using a bivariate NDF modeling allows us to track the particle surface area information and therefore more accurate prediction is made for particle structure and morphology. In the single variable QMOM case, only volume-based description was possible and, consequently, an important particle evolution process related to surface area has to be indirectly inferred from volume information (e.g. surface area obtained from an effective diameter corresponding volume v). In general, however, this may not be physically valid because the particle volume and surface area do not necessarily evolve correlated during an actual flame synthesis process. For example, the sintering process is characterized by significant reduction of particle surface area with no change in particle volume. Consequently, it is highly desirable to introduce particle surface as a new internal coordinate for modeling the sintering process.

Addition of sintering, however, poses numerical difficulty mainly due to the high sensitivity of the sintering rate expression (Eq.(2.56)) to the gas phase conditions, especially temperature. Numerically, this sensitivity increases the stiffness of the ODE solver, causing the solver to sometimes fail due to the exceedingly small inner time-step used. This technical difficulty has been overcome by utilizing a new operator-split ODE integration method [126]. The basic idea behind this method is that the CQMOM weights are not affected by volume growth (Eq.(2.43)), surface growth (Eq.(2.55)), or sintering process (Eq.(2.56)). In other words, only changes in surface area or volume occurs

during these processes. In this method, the ODE integration is divided into two parts. The first part of the ODE handles the nucleation and aggregation events, including the weights of the CQMOM discretization.

$$\overline{m^{(1)^*}}_{kl}^{\,t+\Delta t} = \int_0^{\Delta t} \left(\overline{J}_{kl} + \overline{B}_{kl} - \overline{D}_{kl}\right) dt, \tag{4.1}$$

where Δt denotes LES time step and $m^{(1)^*}$ denotes the interim moment solutions for the first part of the ODE split process. After the first integration, the weights (w_i^* and w_{ij}^*) are found using the product-difference algorithm [93]. These weights are then fixed in time for the second part of the ODE integration.

In the second part, volume and surface growth as well as sintering processes are considered. During this process, only the abscissas change, and therefore, the second ODE integration is carried out in terms of the abscissas instead of the moments. This is possible because the rate expressions are functions of abscissas only and independent of weights. In this step, following coupled integration is performed by the stiff ODE solver for the volume and conditional area abscissas.

$$\begin{aligned}
\overline{v_i^*}^{\,t+\Delta t} &= \int_0^{\Delta t} \left(\overline{G}_v(v_i, a_{ij}, \Phi) + \overline{G}_a(v_i, a_{ij}, \Phi) - \overline{S}_a(v_i, a_{ij}, \Phi)\right) dt, \\
\overline{a_{ij}^*}^{\,t+\Delta t} &= \int_0^{\Delta t} \left(\overline{G}_v(v_i, a_{ij}, \Phi) + \overline{G}_a(v_i, a_{ij}, \Phi) - \overline{S}_a(v_i, a_{ij}, \Phi)\right) dt,
\end{aligned} \tag{4.2}$$

where v_i^* and a_{ij}^* are the intermediate values of the volume and conditional area abscissas. In this study, only sintering is considered but the addition of

growth terms is straightforward. The above equations then simplify to:

$$\begin{aligned} \overline{v_i^*}^{t+\Delta t} &= -\int_0^{\Delta t} \overline{S}_a(v_i, a_{ij}, \Phi)dt, \\ \overline{a_{ij}^*}^{t+\Delta t} &= -\int_0^{\Delta t} \overline{S}_a(v_i, a_{ij}, \Phi)dt, \end{aligned} \tag{4.3}$$

The new solution of the abscissas then, together with the weights w_i^* found from the moments after the first ODE integration, are used to reconstruct a new moment set.

$$\overline{m^{(2)^*}}_{kl} = \sum_{i=1}^{N_v} \sum_{j=1}^{N_a} w_i^* \, w_{ij}^* \, (v_i^*)^k \, (a_{ij}^*)^l \tag{4.4}$$

The final source term for Eq.(2.62) is then determined as follows:

$$S_{kl}^{total} = \frac{\overline{m^{(2)^*}}_{kl} - \overline{m}_{kl}}{\Delta t}, \tag{4.5}$$

where S_{kl}^{total} is the sum of the all sources for m_{kl} in Eq.(2.62).

4.2 Results and discussion

4.2.1 Flame characteristics and nucleation behavior

The CQMOM simulation is an upgrade of the previously discussed QMOM computation by adding a two dimensional CQMOM-based NDF model with the sintering effect included. Consequently, it shares significant parts with the QMOM computation in terms of modeling and running a computational code. As in the QMOM simulation, the laminar flamelet-based turbulence-chemistry interaction model (Sec. 2.3.1) is employed to describe the thermo-chemical states of the identical flame configuration. The nucleation model used for the CQMOM computation is the detailed comprehensive chemistry

model introduced in Sec. 2.4.2, which is the one used previously. Consequently, the flame characteristics as well as nucleation behavior are expected to be the same. CQMOM utilizes precisely the same six QMOM volume moments to describe the NDF with the three volume nodes. With growth term neglected and using the constant fractal dimension d_f, the volume moments in both QMOM and CQMOM computations evolve with the nucleation and aggregation source terms. Besides, no change in the numerical schemes and the computational grid system has been made for this particular setup. Therefore, the particle evolution with respect to the six integer volume moments $(m_{00}, ..., m_{50})$ in CQMOM computation is the same as the QMOM computation and no further discussion is presented here. Below, the discussion is focused on the new features that are exclusive to CQMOM, and mainly concerns the bivariate NDF evolution including the sintering process.

4.2.2 Evolution of nanoparticles

4.2.2.1 Evolution of particle volume concentration and area concentration

Fig. 4.1 shows the normalized particle volume and surface area concentrations at an instantaneous moment. The volume concentration is normalized with respect to the monomer concentration, providing a measure of the growth of the nanoparticles. Without surface and volume growth considered in our CQMOM model and using constant fractal dimension (Eq.(2.54)), the increase of the normalized volume concentration is solely driven by aggregation, which increases particle volume by Brownian collisions. If aggregation is

the sole source of volume growth, the volume concentration m_{10} is determined only by nucleation, aggregation, and turbulent dispersion of particles. The same principle applies for the volume-based equivalent particle size (Eq.(3.3)). The increase of the total volume begins intensifying near the jet break point around x/D=10. Here, the enhanced mixing of the fuel and oxidizer forms relatively large high-temperature reaction zones which accelerates the aggregation process through the temperature dependent Brownian collision kernel (Eq.(2.53)). The aggregation, however, become less intense as the flow moves further downstream mainly due to the reduced number of particles available for aggregation. This trend is noticeable in Fig. 3.7, where minimal change in the equivalent particle size is observed approximately after x/D=15.

Fig. 4.1 shows the normalized surface area concentration normalized by the monomer surface area. without surface growth, only sintering changes the conditional area node location in the CQMOM representation. However, sintering itself is strongly dependent on gas phase temperature and the size of the nanoparticles, thereby linking the area moment evolution to the volume moments and the gas phase composition. Indirectly, aggregation also plays an important role in sintering through the use of volume in the sintering source term. This interaction is important since aggregation and sintering change surface area oppositely. Consequently, even in the presence of sintering, the local surface area concentration could increase due to the aggregation process. This trend is seen in Fig. 4.1, where a significant increase in surface area concentration is observed near the jet break point. This is due to the dominant effect

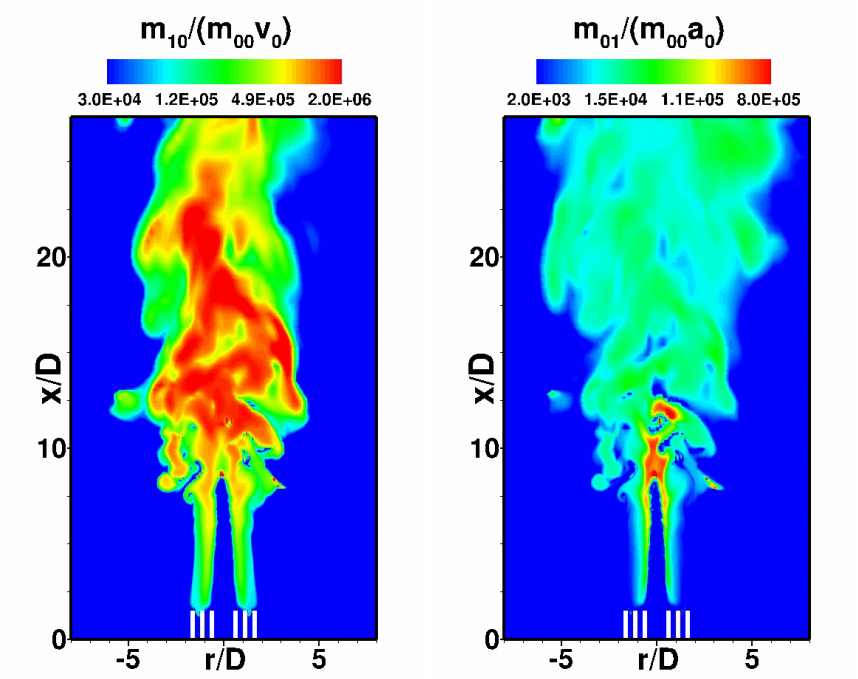

Figure 4.1: Instantaneous contour plots of the (left) normalized particle volume and (right) surface area concentrations.

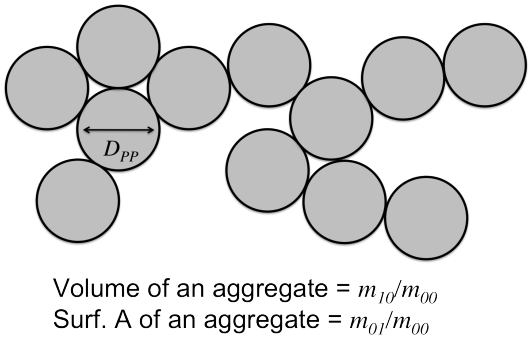

Figure 4.2: A schematic of the particle aggregate structure used to determine the primary particle characteristics. The aggregate is assumed to consist of equal-sized spherical primary particles with point-wise contact.

of aggregation with sintering effect not yet comparable to that of aggregation. However, after this point, the strong area increase is quickly suppressed by sintering process due to aggregation upstream and through turbulent dispersion. Consequently, much faster total surface area reduction rate is observed than that of the volume concentration. From approximately x/D=10 to x/D=20 along the centerline, the area concentration $m_{01}/(m_{00}V_0)$ reduces by two orders of magnitude but the volume concentration shows very little change.

4.2.2.2 Evolution of the size and the number of the primary particles

With the particle surface area information available, a study of particle aggregate structure can be made now. Assuming that each of m_{00} particle aggregates has a volume of m_{10}/m_{00} (m^3) and area of m_{01}/m_{00} (m^2) (i.e. monodisperse) and the each aggregate is composed of equal-sized spherical primary particles with point contact (Fig. 4.2), the number and size of primary

particles per aggregate are found from following equations:

$$N_{pp} = \frac{m_{01}^3}{36\pi\, m_{00} m_{10}^2}, \qquad D_{pp} = \frac{6\, m_{10}}{m_{01}}. \tag{4.6}$$

Fig. 4.3 shows the mean axial profiles of D_{pp} plotted along with the specific surface area (SSA, defined below), as well as N_{pp} plotted along with the sintering rate as a function of axial distance along the centerline. Using the total volume and area concentrations, the SSA is defined as

$$\mathrm{SSA} = \frac{m_{01}}{\rho_{\mathrm{TiO_2}}\, m_{10}}, \tag{4.7}$$

where $\rho_{\mathrm{TiO_2}}$ is the bulk density of solid TiO_2. The SSA is a quantitative measure of primary particle size. It can be also considered as a statistical quantity obtained from a large number of sampled particles. The plot shows sharp decrease of SSA at near x/D=10, where the jet breakdowns (see Fig. 4.1). From Fig. 4.1, it is clear that the most significant changes in particulate behavior occur near this location, where the primary particle number peaks and quickly reduces with particle sintering. This behavior is consistent with Fig. 4.1, where the area concentration was found to decrease rapidly due to a reduction of aggregation as well as nucleation processes beyond this jet breakdown point. While the particle diameter (D_{pp}) also changes rapidly, it is seen in Fig.. that the sintering rate and primary particle numbers are large over only a short axial distance. This indicates that aggregation as well as sintering affects particle diameter changes, while the primary particle number is predominantly controlled by sintering rates.

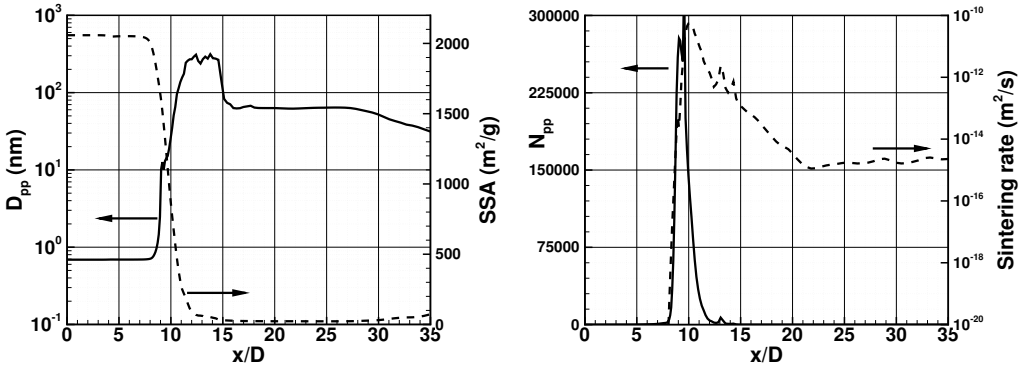

Figure 4.3: Mean axial profiles of (left) the primary particle size and specific surface area and (right) the number of primary particles per aggregates and sintering rate.

As shown in Fig. 4.1 and 4.3, it is noticed that the evolution of particle volume and surface area are closely related to the first volume moment m_{10} and the first area moment m_{01}, respectively. These quantities are statistical values comprising all possible sets of volumes and areas at a certain location and a time. Therefore, it should be noticed that the particle structures obtained from Eq.(4.6) does not reflect true statistical size and number of the primary particles. Rather, it should be understood as a modeled measurement for how particle cluster structure evolves during flame synthesis process. This limitation (i.e. track only the moments, not the distribution itself), on the other hand, can be viewed as an advantage of the method of moments (MOM) approaches (e.g. QMOM, CQMOM, DQMOM) because, if we are interested in certain statistical values rather than the distribution function itself, those statistics of interest can be obtained at a much lower cost than the entire particle density distribution.

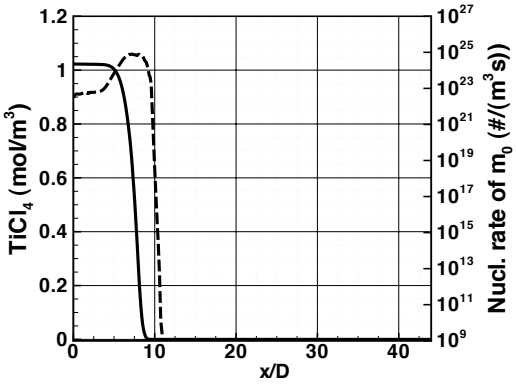

Figure 4.4: Mean axial profiles of the $TiCl_4$ precursor concentration (solid line) and particle nucleation rate (dashed line).

4.2.3 Evolution of bivariate NDF

The evolution of the NDF in a flame reactor is the result of combined effects of turbulence, combustion, precursor oxidation, and aggregation and sintering. Consequently, the evolution shows different development phases at different downstream locations of the flow fields. Fig. 4.5 shows the mean NDF at selected locations along the axisymmetric line. The initial phase of the NDF evolution is dominated by strong nucleation. At x/D=5, (Fig. 4.5a), the strong domination of the first node is noticed with its height approximately order of 6 and 8 time higher than those of the second and third, making the NDF almost unimodal. Because the volume and area associated with the first node are barely larger than those of nuclei, this unimodal NDF indicates that majority of the nanoparticles comes from nucleation with minimal aggregation and sintering. As the flow moves to x/D=10 (Fig. 4.5b), however, the domination of the particle formation is quickly lost mainly due to quick consumption

of the $TiCl_4$ precursor as shown in Fig 4.4. The reduction of nucleation is indicated in the weight associated with the first node, which reduces by two orders of magnitude compared to that at x/D=5. Instead, particle aggregation becomes significant due to the high gas phase temperature in this region. This increases the frequency of particle collisions for the small particles transported from upstream locations. At the same time, the sintering process also accelerates with intensive formation of the particle aggregates in high temperature environment. Yet, the effect of sintering is not as strong as aggregation at this location because the area and volume of all three nodes increase, which strongly suggests that the aggregation is more important process than sintering at this location. More specifically, the heights of the second and third nodes increase approximately order of 2 and 3, respectively, and the area associated with the first and third nodes increase more than order of 4 when compared to the previous location at x/D=5. Therefore, at this location, overall shape of the NDF becomes more uniform mainly due to aggregation. At x/D=20 (Fig. 4.5c), the node information shows the decrease of area (approximately order of 1 or 2 from x/D=10) with minimal change in volume for all the three nodes. This indicates that sintering has become more dominant, while the effect of aggregation reduces due to a reduction in particle number density. Further downstream (x/D=30, Fig. 4.5d), the area corresponding to all three nodes show further reduction, with little change in the volume nodes, which is typical of particle sintering. Therefore, the NDF at this location suggests that the sintering is a major contributor at the later stage of the NDF evolution.

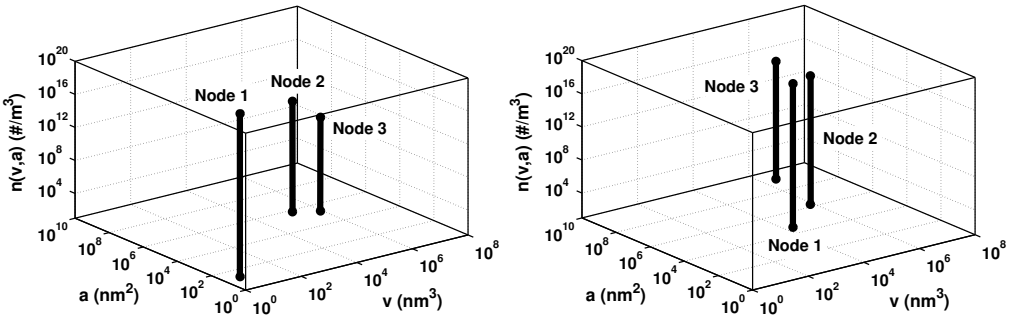

(a) $x/D = 5$

(b) $x/D = 10$

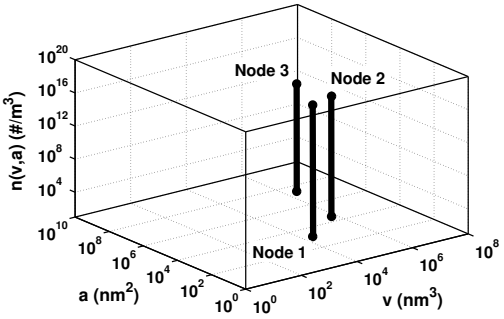

(c) $x/D = 20$

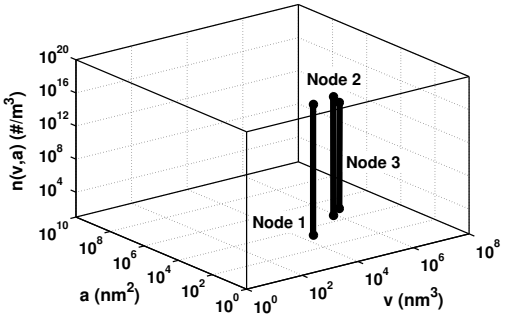

(d) $x/D = 30$

Figure 4.5: Mean axial NDF along various downstream locations.

	LES-QMOM (Ch.3)	LES-CQMOM (Ch.4)	Exp. [4]
Particle size (nm)	108 (Eq.(3.3))	61 (Eq.(4.6))	100∼105
SSA (m^2/g)	129 (Eq.(3.4))	25 (Eq.(4.7))	17

Table 4.1: Comparison of LES results of particle size and specific surface area (SSA) against the experimental data [4].

4.2.4 Comparison against experiment

The results of the new bivariate LES-CQMOM based modeling has been compared against the available experiment data. Table 4.1 shows the mean particle sizes and specific surface areas obtained from LES-QMOM and LES-CQMOM methods as well as those from the experiments. The simulation data are radially averaged at x/D=30, where actual particle collection was made during the experiment. With the sintering process considered, the CQMOM-based bivariate model exhibits significantly improved prediction for the specific surface area over the QMOM-based univariate model. The predicted value of 25 m^2/g is reasonably close to that found in the experiment. It should also be noted that in the CQMOM approach, the particle surface area can be directly obtained from the bivariate formulation, while in the QMOM approach, this information has to be inferred from the volume nodes. The assumptions used therein could also contribute to errors in the QMOM-based surface area reported here. However, the primary particle size is considerably underpredicted. These observations and their dependance on flow configuration will be the focus of future studies.

4.3 Summary

In this Chapter, the LES-CQMOM approach to nanoparticle simulation using a bivariate NDF was discussed. The new model presents a significant advance compared to the QMOM representation, adding surface area as a second coordinate. The NDF was described using three volume moments, and three mixed volume-area moments. This allowed sintering effect to be included in the description of nanoparticle evolution. In addition, the sintering effect was added to the moment transport equations to accurately track the change of the area-containing moments. The addition of the sintering source term increases the stiffness of the moment source terms, and leads to failure of the semi-implicit stiff ODE solvers. This problem has overcome by utilizing a novel operator-split ODE integration method, where the nucleation and aggregation sources are integrated in the first stage (Eq.(4.1)), followed by the direct integration of the volume and the conditional area abscissas in the second stage (Eq.(4.2)). The moments after ODE integration were found reconstructed based on the weights and abscissas after the second stage.

The LES-CQMOM model was found to produce interesting dynamics between the aggregation and sintering processes. While aggregation appears to be dominant near nucleation sites due to the high particle number density, the sintering process becomes more dominant with increasing gas phase temperature and particle volume concentration. At downstream locations, sintering remains dominant due to the relatively high temperature in the post-flame gas phase.

Finally, the results were compared with experimental data. While the CQMOM computations provided better specific surface area comparison with regard to experiments, the primary particle diameter was found to be lower. These results indicate that further analysis of the underlying models are necessary.

Chapter 5

Improved LES-based QMOM computation of TiO_2 flame synthesis with a moment correction algorithm

The advection of scalar moments invariably leads to inconsistencies, since the discretization algorithms cannot ensure realizability of the underlying number density function [5, 127]. Consequently, moment correction procedures are necessary to ensure that inconsistent moment sets do not propagate in space and contaminate the entire solution. In this chapter, an improved moment correction algorithm is presented.

5.1 Physical validity of NDF moments

5.1.1 NDF moment corruption and validity condition

The inconsistencies in the moment equation arise from a number of sources. First and foremost, the presence of sink terms in the equation arising from aggregation or sintering, lead to reduction of certain moments that can ultimately lead to negative values. Although this cannot happen theoretically, the use of the fractional time-stepping method can introduce such inconsistencies, especially if the timestep is large compared to the reaction timescales. Further, moments are transported independently, coupled only through the

reaction source terms, implying that truncation and dispersion errors associated with the numerical schemes for a given moment are virtually independent of other moments. This feature is one of the main sources of moment inconsistency [5, 127]. These errors are further amplified in the presence of steep spatial gradients or stiff reaction source terms due to nearly discontinuous jumps in the three-dimensional field.

This problem has been studied by a number of researchers, and a variety of mitigating techniques have been developed [5, 69, 127]. Although the individual methods vary in detail, the proposed techniques almost always involve local correction of the moment set once an inconsistent moment set has been identified. Hence, such techniques involve two steps: The identification of corrupt moment sets, and a correction technique to ensure validity.

For a moment set to be valid, the most important condition is that the number density function that corresponds to those values stays positive over the entire range of the sample space. This condition leads to the convexity test that must be met for a sequence of moments. For instance, for the volume moments with N_v nodes in a bivariate NDF,

$$\frac{d^2 \log m_k}{d\, k^2} \geq 0 \quad (k = 0,1,\ldots,2N_v\text{-}1), \tag{5.1}$$

which is equivalent to satisfying

$$m_{k+2} m_k - m_{k+1}^2 > 0 \quad (k = 0,1,\ldots,2N_v\text{-}3). \tag{5.2}$$

A similar condition should be satisfied for volume-area mixed moment sets such as $\{m_{01}, m_{11}, m_{21}\}$. The condition, which ensures non-negative curvature for

$\log m_k$ in terms of k, however, is a necessary but not a sufficient condition for a valid moment set. The necessary and sufficient requirement is to have non-zero values for all of the Hankel-Hadamard determinants [128] (i.e. invertible matrices):

$$\begin{gathered}
|m_0|,\ |m_1|, \ldots, |m_{2N_v-1}| \ > 0, \\
\begin{vmatrix} m_0 & m_1 \\ m_1 & m_2 \end{vmatrix}, \ldots, \begin{vmatrix} m_{2N_v-3} & m_{2N_v-2} \\ m_{2N_v-2} & m_{2N_v-1} \end{vmatrix} > 0, \\
\begin{vmatrix} m_0 & m_1 & m_2 \\ m_1 & m_2 & m_3 \\ m_2 & m_3 & m_4 \end{vmatrix}, \ldots, \begin{vmatrix} m_{2N_v-5} & m_{2N_v-4} & m_{2N_v-3} \\ m_{2N_v-4} & m_{2N_v-3} & m_{2N_v-2} \\ m_{2N_v-3} & m_{2N_v-2} & m_{2N_v-1} \end{vmatrix} > 0, \\
\vdots \\
\begin{vmatrix} m_0 & m_1 & \cdots & m_{N_v-1} \\ m_1 & m_2 & \cdots & m_{N_v} \\ \vdots & \vdots & \vdots & \vdots \\ m_{N_v} & m_{N_v+1} & \cdots & m_{2N_v-1} \end{vmatrix} > 0.
\end{gathered} \tag{5.3}$$

The non-zero condition for the matrix determinants for the first four moments is equivalent to the convexity condition (Eq.(5.2)). Again, a similar condition must be met for the volume-area mixed moment sets. For QMOM/CQMOM, the node information (weights and abscissas) have to be determined from the moment sets using the product-difference algorithm. For physically valid moment sets satisfying the above non-zero conditions, the product-difference (PD) algorithm is guaranteed to work and the node information are safely recovered. However, the corrupted moment sets often exhibit ill-conditioned weights and abscissas, meaning that one or more of these quantities tend to be very large or small compared to the other weights/abscissas. This is

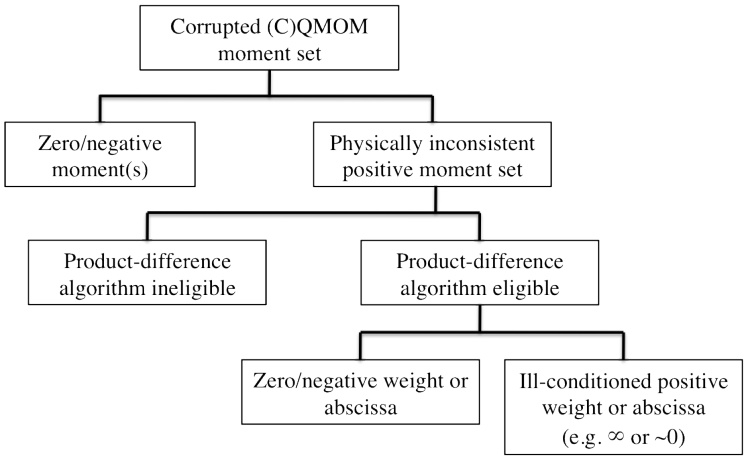

Figure 5.1: The different types of numerically-corrupted moments

detrimental to the numerical computations since the NDF source terms are highly sensitive to these quantities.

In the present study, a corrupted moment set refers a sequence of moments that fails to satisfy the above conditions. The occurrence of the corrupted moment sets cannot be avoided and should be minimized because 1. we are unable to obtain any valid meaningful information about NDF from them and 2. they are problematic to numerical computation. Fig. 5.1 shows types of such erroneous CQMOM moment sets occurring during the computation. The main reason for the generation of negative moments is the interpolation used in higher-order finite volume schemes to move the cell-centered scalar values to the cell faces. This interpolation cannot guarantee validity of the underlying NDF. Typically, the sink terms in the scalar transport equations reduce the moments to small values, at which point, the errors in interpolation corrupt the moment set. This issue is exacerbated by the fact that the

moments typically span a very large range of values. For instance, a typical moment set will contain values from 1–10^{-140}. Consequently, even small errors in ODE integration or scalar interpolation can render the moment set invalid.

To minimize the presence of negative moments, and to help compute moments with large disparity in values, the natural logarithm of the moments are used in the ODE time integration routines. It should be noted that the true moments are still used for the spatial transport part of the LES algorithm. At each time step, the true moments are log-scaled before entering the ODE integration routine. Negative or zero moments cannot be converted and have to be handled using the moment correction algorithm to be detailed next. The log-scaled moments can be integrated in time for each computational cell based on the following relations.

$$\begin{aligned} \frac{d\ln\overline{m}_k}{dt} &= \frac{1}{\overline{m}_k}\frac{d\overline{m}_k}{dt} = \frac{1}{\overline{m}_k}\left(\overline{J}_k + \overline{B}_k - \overline{D}_k\right) \quad \text{(for QMOM)}, \\ \frac{d\ln\overline{m}_{kl}}{dt} &= \frac{1}{\overline{m}_{kl}}\frac{d\overline{m}_{kl}}{dt} = \frac{1}{\overline{m}_{kl}}\left(\overline{J}_{kl} + \overline{B}_{kl} - \overline{D}_{kl} - \overline{S}_{a,kl}\right) \text{ (for CQMOM)}. \end{aligned} \tag{5.4}$$

The integrated values are converted back to true moments to obtain the source terms, which are then used in the scalar transport equations. The most important benefit of this log-scaled integration is that the moments are guaranteed to stay positive during the ODE integration. Besides, the final moment source terms computed in this way do not make moments go zero/negative, therefore significantly reducing the appearance of the zero/negative moments. Finally, it also effectively reduces huge difference in magnitudes of the low and high

order moments. For example, in the previous QMOM and CQMOM computations, m_{00} exhibits magnitude of O(1)–O(10^{21}), while m_{50} varies in a range of O(10^{-140})–O(10^{-67}). By doing the log scale, this huge difference is cut down to reasonable level and helps convergence behavior of the stiff ODE solver. In fact, this log-scaled integration is a key part to prevent non-positivity of the CQMOM moments and has been used for the simulations presented in Ch. 3 and 4.

5.1.2 Correction of corrupted moments

Although the non-positive moment can be minimized utilizing the log-scaled moments for the source term integration, the moment sets still can become physically inconsistent with all positive moments. This happens when the integrity of positive moment sets are destroyed by the scalar advection scheme, interpolation, and/or sharp gradients of the moments locally present in the flow field. In present study, this type of erroneous moment sets are corrected using the method proposed by McGraw [5], which tries to restore or maximize the smoothness of $\ln(m_{k0})$ sequence by identifying and adjusting problematic moments m_{k^*0} in a limited number of correction attempt iterations. To identify the suspicious moment index k^*, the method utilizes the so-called "difference table". Each column in the difference table is formed by the difference between the elements of the previous column. Examples of difference table for valid and invalid QMOM volume moment sets $\{m_{00}, m_{10}, \ldots, m_{50}\}$ are shown in Table 5.1. Columns d_i in the tables indicate the i-th order differ-

k	$\ln(m_{k0})$	d_1	d_2	d_3	d_4	d_5
0	0	1	2	0	0	0
1	1	3	2	0	0	–
2	4	5	2	0	–	–
3	9	7	2	–	–	–
4	16	9	–	–	–	–
5	25	–	–	–	–	–

k	$\ln(m_{k0})$	d_1	d_2	d_3	d_4	d_5
0	0	1	2	-3	12	-30
1	1	3	-1	9	-18	–
2	4	2	8	-9	–	–
3	6	10	-1	–	–	–
4	16	9	–	–	–	–
5	25	–	–	–	–	–

Table 5.1: Examples of difference tables for valid (top) and invalid (bottom) moment sequences [5].

ence of $\ln(m_{k0})$. The second order difference d_2 implies the convexity condition (the first two rows in Eq.(5.1.1)), which is a necessary (but not sufficient) condition for the validity of a moment set. Table 5.1 also provides an example of an invalid moment set, where some of the difference table elements become negative, violating the Hankel-Hadamard positivity condition. For the six moment set, the third order difference column d_3 is used to determine which moment to modify because it is this column that gives the information about the incorrect moment m_{k^*0}. Consequently, we define a vector $\mathbf{a}$ having the components in the d_3 column (e.g. $\mathbf{a} = (0; 0; 0)^{-1}$ and $(-3; 9; -9)^{-1}$ in Table 5.1). The moment correction is made by multiplying a constant c_k to the the target moment m_{k^*0}. In terms of the scaled moments, this leads to

$$\ln(m_{k^*0})_{\text{new}} = \ln(c_k) + \ln(m_{k^*0})_{\text{old}} \tag{5.5}$$

and the problem is now equivalent to determining the correction constant c_k, for which McGraw [5] has developed the minimum square gradient algorithm. The algorithm attempts to minimize the magnitude of $\mathbf{a}_{\text{new}}$, which corresponds to the new third order difference vector obtained after applying $\ln(m_{k^*0})_{\text{new}}$ to the difference table. The new vector $\mathbf{a}_{\text{new}}$ is determined from

$$\mathbf{a}_{\text{new}} = \mathbf{a}_{\text{old}} + \ln(c_k)\, \mathbf{b}_k, \tag{5.6}$$

where $\mathbf{b}_k$ are the "response" vectors, indicating the unit increment of the third order difference vector in $\ln(m_{k0})$. They are related to the elements in

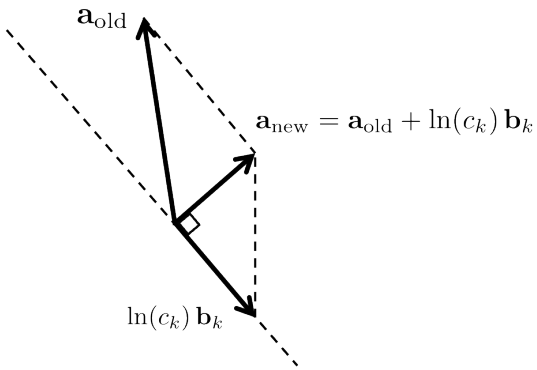

Figure 5.2: Minimum possible change of the third order difference vector **a** for moment correction [5].

the Pascal's triangle [5] and are given as

$$\mathbf{b}_0 = \begin{pmatrix} -1 \\ 0 \\ 0 \end{pmatrix}; \mathbf{b}_1 = \begin{pmatrix} 3 \\ -1 \\ 0 \end{pmatrix}; \mathbf{b}_2 = \begin{pmatrix} -3 \\ 3 \\ -1 \end{pmatrix}; \mathbf{b}_3 = \begin{pmatrix} 1 \\ -3 \\ 3 \end{pmatrix}; \mathbf{b}_4 = \begin{pmatrix} 0 \\ 1 \\ -3 \end{pmatrix}; \mathbf{b}_5 = \begin{pmatrix} 0 \\ 0 \\ 1 \end{pmatrix}. \tag{5.7}$$

Minimization of $|\mathbf{a}_{\text{new}}|$, or minimum possible change achievable from the modification of single moment m_{k^*0}, is obtained when the vector $\mathbf{a}_{\text{new}}$ is orthogonal to the vector $\ln(c_k)\,\mathbf{b}_k$ as shown in Fig. 5.2. The correction constant c_k is

$$\ln(c_k) = -\mathbf{cos}(\mathbf{a}_{\text{old}}, \mathbf{b}_k)\frac{|\mathbf{a}_{\text{old}}|}{|\mathbf{b}_k|} = -\frac{\mathbf{a}_{\text{old}} \cdot \mathbf{b}_k}{|\mathbf{b}_k|^2}. \tag{5.8}$$

Hence the maximum smoothness of $\ln(m_{k0})$ set is achievable when $\mathbf{cos}(\mathbf{a}_{\text{old}}, \mathbf{b}_k)$ is maximized. The suspicious moment index k^* then is determined from the index of $\mathbf{b}_k$ that gives the maximum cosine value. Once the corresponding c_{k^*} is determined in this way, a correction of m_{k^*0} is made using Eq.(5.5). This process is continued until the algorithm fixes all problematic elements.

The correction procedure used in LES-CQMOM code is shown in Fig. 5.3.

First, a volume moment set in each computational grid cell is checked for the physical consistency (Eq.(5.1.1)). If the consistency is not satisfied (e.g. a positive but inconsistent moment set or a set with one or more zero/negative moments), the correction procedure detailed above is attempted. For each of the problematic volume moment sequence, a correction trial is made with maximum 10 iterations. If the correction is successful, the moments are passed to the stiff ODE solver to compute moment source terms. If not, however, it is marked failed and the ODE source term computation is entirely skipped for that particular moment set. The moment correction is applied only to the volume moment sequence $\{m_{00}, \ldots, m_{50}\}$ and not to the three mixed volume/area moment sequence $\{m_{01}, m_{11}, m_{21}\}$ since a set of three moments is insufficient to be used with the correction algorithm. Increasing the number of CQMOM area nodes does not increase the length of the mixed moment sequence. However, the convexity condition is still checked for the mixed moment sets and the moment source term is skipped if the positivity condition is not met.

5.2 Effect of moment correction on LES solution

In this section, brief results of the moment correction effect is presented. Two simulations, one with the correction algorithm and the other without the correction algorithm are compared. The evolution of six QMOM volume moments in the $TiCl_4$ reactor is used to determine the effect of moment correction. The nanoparticle evolution model used is identical to that used in the QMOM formulation discussed in Ch. 3.

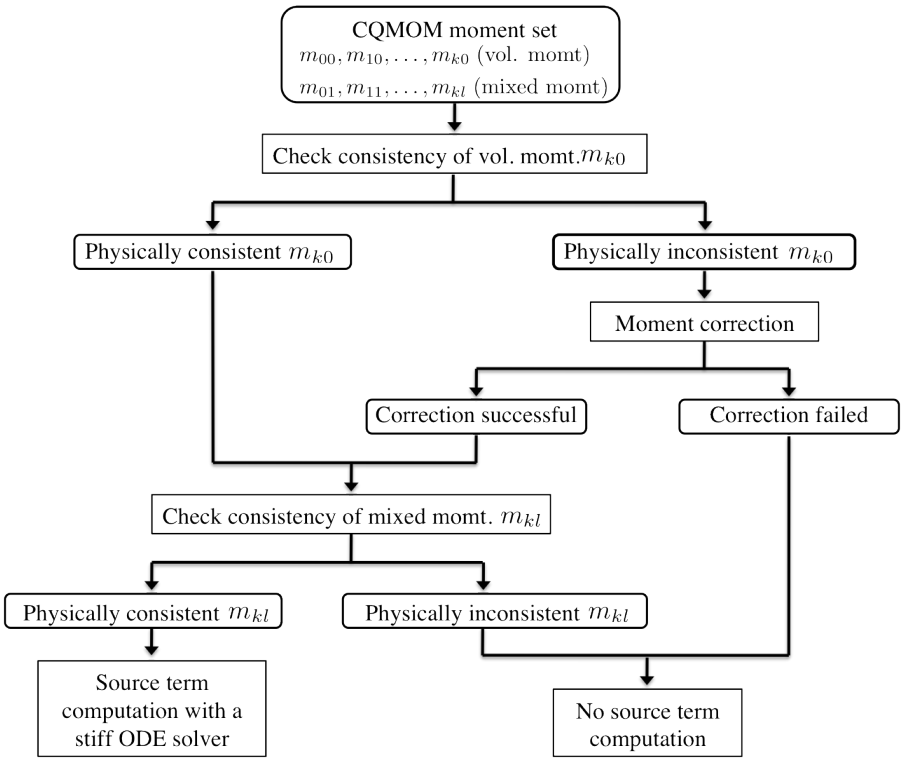

Figure 5.3: A flow chart of moment correction for CQMOM moment sets in an LES computation

5.2.1 Flame configuration

As in previous cases, the flame D configuration in Pratsinis et al. [4] is used. However, in this study, a higher flow rate (5500 ml/min) of the air stream is used than the previous computations (3800 ml/min). The former corresponds to the Flame number 11 and the latter corresponds to 7 in Pratsinis et al. [4], respectively. The higher flow rate allows earlier breakdown of the jet, which is desirable since the grid is very coarse further downstream. Apart from this modification, the flame configuration is identical to the cases reported in Ch. 3.

5.2.2 Simulation set up and numerical methods

For the sake of this study, certain simplifications are made. Since the focus is on demonstrating the usefulness of the correction approach, only the six volume moments of the QMOM approach are used. None of the mixed area/volume moments are transported. The simulation also used a smaller grid system of 96×32×16 spanning over a cylindrical domain of 38D×30D (Fig. 5.4), where D=4 mm is the main jet inner diameter. Although a smaller grid system is used, the grid density near the reactor exit is comparable to that of the previous case (Ch. 3). The computational domain starts from the burner exit and consequently it does not contain the physical walls used in the previous cases. This is mainly a numerical detail since the walls are now considered as zero velocity inlet streams, and the exact thickness is retained in the simulation. The scalar equations (mixture fraction variables, precursor

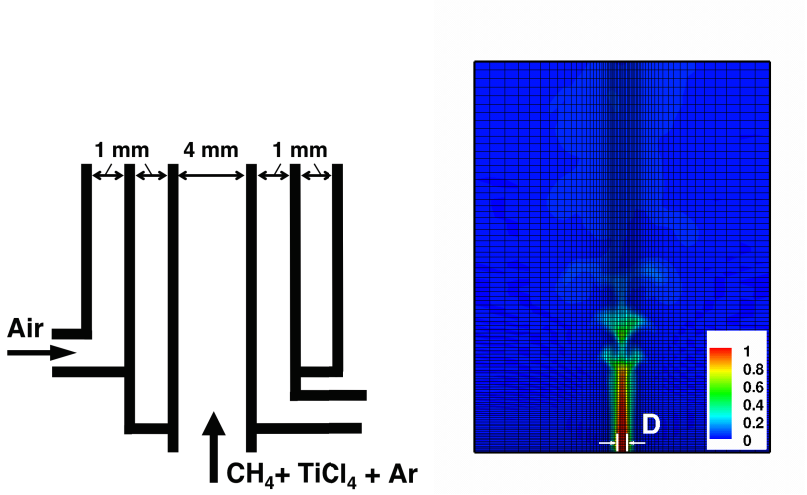

Figure 5.4: (Left) A schematic of the flame reactor and (right) cylindrical grid system used in the simulation. Mixture fraction is shown in the background contour scheme.

mass fraction, and 6 QMOM volume moments) are solved using the fifth-order weighted essentially non-oscillatory (WENO) scheme [124, 129] to compensate possible accuracy reduction caused by the coarser grid cell system. The momentum and continuity equations are advanced using the low-Mach number solver detailed previously (Ch. 3).

5.2.3 Results and discussion

Fig. 5.5 show instantaneous locations of the cells that contain the erroneous moment sets in early and later stages of QMOM volume moments evolution (approximately 0.1 and 5 flow residence time τ based on the main jet velocity and the axial domain length). In both cases, the corrupted moment sets are mostly observed in the regions with 1. active convective transport,

2. high moment gradients (e.g. interface of the jet and the ambient air), and 3. axisymmetric line in the early development. The author believes the cause of the moment corruption along the centerline is due to the radial velocity treatment at the centerline, which is to prevent the singularity $(1/r)$ in the momentum transport equation in the radial direction. Combined with the fact that a relatively coarse grid system used in the current study and the convection of each moment is made uncoupled, this centerline velocity adjustment may cause the local moment transport less favorable for the moment sets to stay physically consistent. However, problematic moment sets of this kind are expected to be significantly reduced when enough number of grid cells are used in the LES code because the radial velocity treatment is second order accurate in radial direction. In fact, they disappear almost entirely when tested on a much dense grid cell system. ($256\times128\times32$). In the later stage of the moment development, the corrupted moments caused by 1 and 2 are mostly convected away for both cases. Table 5.2 shows the number of computational grid cells that contain erroneous volume moment sets. The number found by averaging over 10 flow residence time. In general, the moment correction helps to reduce the number of the inconsistent moment set. The invalid moment sets are easily identified by the convexity and matrix inversion tests (Eq.(5.1.1)) in the correction algorithm. However, it primarily focuses on restoring the smoothness of a moment sequence and does not check the validity of the weights and abscissas obtained from the moment sequence. Although a set of moments can pass all the necessary validity tests, the resulting weights and abscissas still

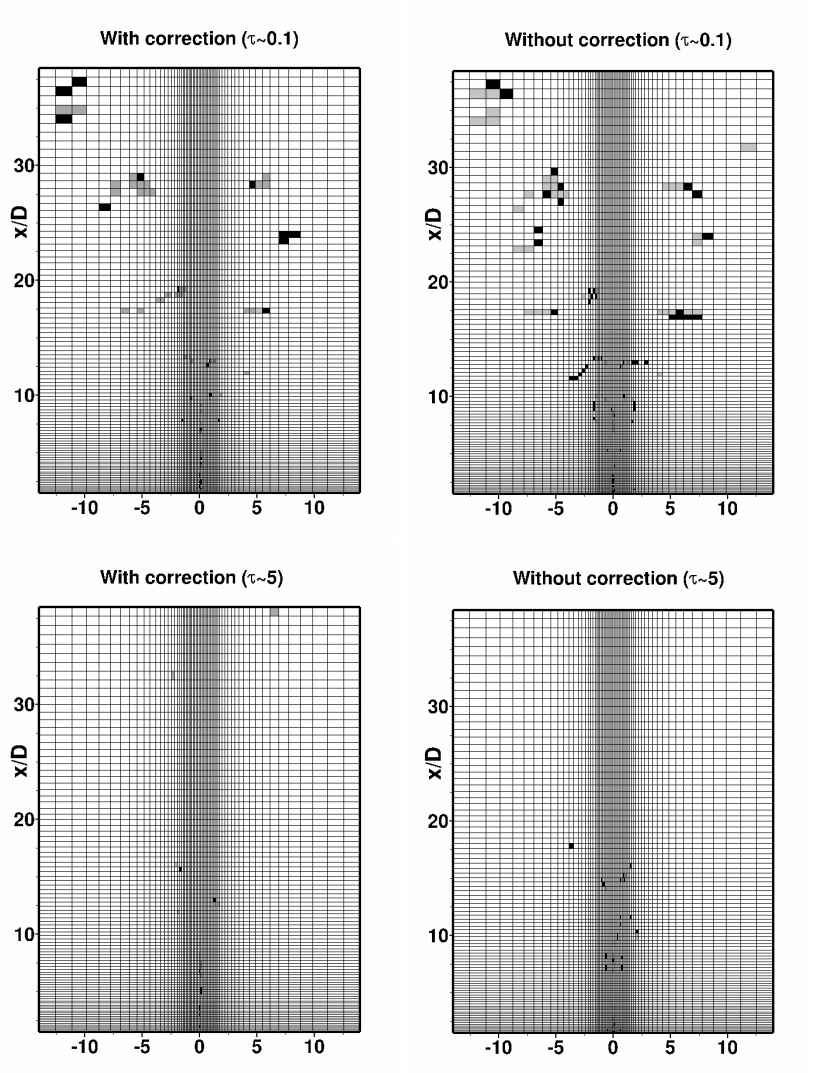

Figure 5.5: Instantaneous images of corrupt moment set locations at $\tau \sim 0.1$ (top row) and $\tau \sim 5$ (bottom row). For the plots obtained using moment correction methodology (left column), the gray and black colored cells indicates successful and failed correction trials for the physically invalid moment sets, respectively. For the case with no correction (right column), the gray and black colored cells indicate inconsistent moment sets with one or more zero/negative elements and with all positive elements, respectively.

	Number of inconsistent moment sets		
	Correction successful	Correction failed	Total
With correction	∼220	∼30	∼250
Without correction	–	–	∼580

Table 5.2: Number of computational grid cells with physically inconsistent moments.

could be problematic in some case. Fig. 5.6 shows the time averaged weights and abscissas along the centerline for the two cases. A notable difference is observed on the third node as the correction reduces w_3 while increases D_3, especially near the reactor exit ($x/D < 2$). Here, D_3 obtained from the corrected moments are up to three times larger than D_3 obtained from the case with no correction. At the same time, w_3 from the corrected moments shows much less values at $x/D \sim 2$. In fact, its values go down as low as 10^{-5} in this region. This implies that, in the near filed, the QMOM-based NDF distributions obtained from the corrected moments exhibit more binodal characteristics with its third node decreasing and "running away" faster from the other two than those obtained from the non-corrected moments. The correction algorithm also affects the NDF characteristics in the downstream. It is noticed that approximately twice larger D_3 are obtained when the correction is applied to the QMOM moments. Although not as noticeable as in the near field, w_3 from the correction also exhibits less values than w_3 without the moment correction. Another interesting observation is that the correction tends to provide more aggregation in the downstream than the other case. This is because the

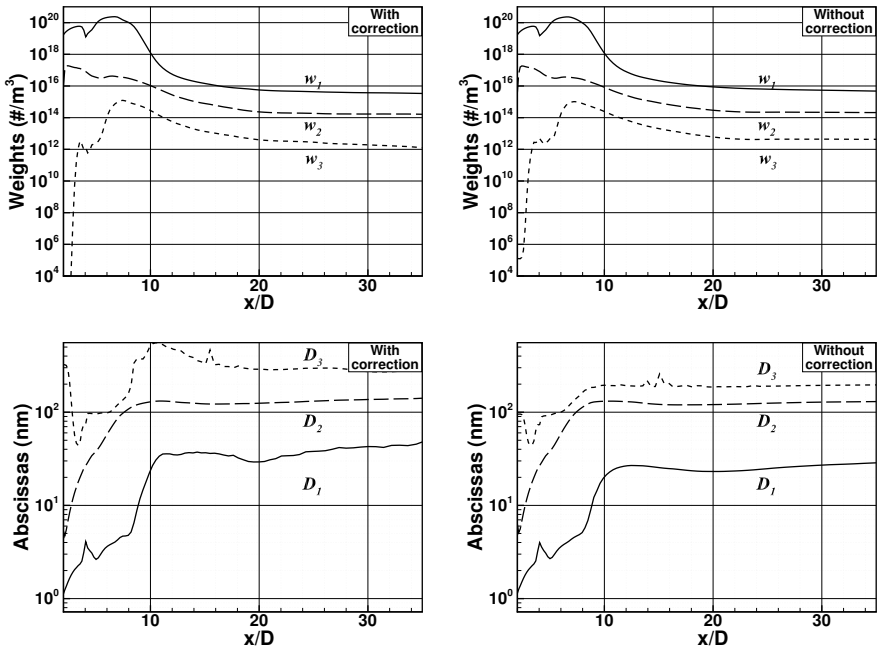

Figure 5.6: The mean weights (top) and abscissas (bottom) obtained along the centerline as a function of axial distance. The left column shows data with moment correction while the right column is based on simulation without moment correction.

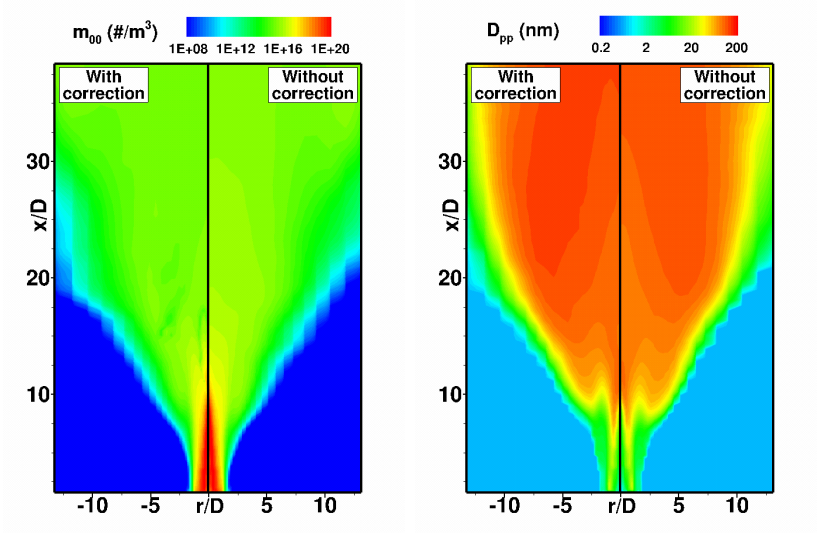

Figure 5.7: Comparison of (left) mean number density (m_{00}) and (right) particle size for the cases with and without moment correction.

aggregation is computed for the invalid moment sets whenever the correction is successful, while it is entirely skipped in the other case. Consequently, as shown in Fig 5.7, predicted TiO_2 particles are with less number density with larger particle size (Eq.(3.3)) when the correction algorithm is applied.

5.3 Summary

In this chapter, the symptoms and causes of the moment corruption are introduced, followed by its treatment method. Essentially, the corruption comes from 1. uncoupled, independent transportation of NDF moments, 2. sharp moment gradients, 3. (related to 2) numerical schemes including interpolation and derivation, 4. local out-of-bound moments (i.e. zero/negative moments) and 5. centerline velocity treatment for cylindrical coordinates,

which is specific to structured cylindrical grid systems only and can be virtually eliminated by increasing the number of grid cells. Restoration of a corrupted moment set can be done by identifying and modifying suspicious moment elements in the moment sequence using the minimum square gradient algorithm proposed by McGraw [5]. The correction algorithm attempts to maximize the smoothness of log-scaled moments based on log-normal distribution.

The effect of the correction algorithm has been studied for the ETH flame reactor used in Ch. 3. To focus on the effect of the correction, an economical simulation setup was used using smaller grid system with no reactor wall included. Under current nanoparticle synthesis model with nucleation and aggregation considered for six QMOM volume moments, it has been found that the correction tends to make the QMOM-approximated distribution exhibits more binodal characteristic by reducing the weights and increasing the abscissa of the third node. Also it has been noticed that less number of particles with larger sizes are predicted when the correction is applied to the model. This can be attributed to the additional aggregation from successful correction trials of the physically inconsistent moments.

Chapter 6

Conclusions

A novel computational tool based on the LES methodology has been developed and tested for gas-phase flame synthesis process of titania nanoparticles in a non-premixed diffusion flame. The proposed model consists of four components: 1) LES solver for the gas phase turbulent flow, 2) a steady laminar flamelet model for gas phase combustion, 3) an unsteady precursor oxidation model using detailed precursor chemistry, and 4) a PBE solver based on the method of moments. In this study, two different PBE solvers were developed based on the quadrature method of moments (QMOM) and the conditional quadrature method of moments (CQMOM). Different physical processes including nucleation, Brownian collision based aggregation, and sintering processes were considered. To the author's knowledge, this detailed model is the first such comprehensive simulation tool developed for flame synthesis of nanoparticles.

This novel computational tool was used to simulate an experimental flame studied at ETH Zürich. It was demonstrated that the LES model reproduces the general trends seen in the experiments, including the accurate prediction of the maximum axial temperature. The QMOM-based computa-

tions over predicted the specific surface area as compared to experiments while the primary particle diameters were reasonably well-predicted. The addition of sintering using the CQMOM approach significantly improved the prediction of specific surface area but also reduced the particle diameters. The lack of detailed experimental measurements similar to that found in the turbulent combustion field was a major hindrance in the effective validation of the computational model. However, it should be noted that these computations did not involve tuning or calibration of the underlying models, and were performed using published model coefficients. It is expected that more fundamental studies of the particulate evolution models combined with the availability of detailed experiments will significantly increase the predictive capability. Nevertheless, we can assert that this LES-based tool provides the most comprehensive computational framework for incorporating detailed models for the individual subprocesses.

In addition to the modeling component, a consistent population balance solution scheme was also developed. By modifying existing algorithms, a new algorithm to effectively reduce the occurrence of invalid or corrupt moments was developed. The progress made in this area will serve as the basis for future moment-transport algorithms that involved coupled-transport schemes with demonstrable realizability constraints.

List of accomplishments

- Development of a new conditional quadrature method of moment (CQ-MOM) based population balance solver tailored for large eddy simulation (LES).

- First large eddy simulation (LES)-based computation of the titania nanoparticle synthesis process in a gas-phase turbulent flame with an actual experimental setup.

- Development of the unsteady nucleation model based on detailed precursor kinetics.

List of publications and presentations

- Y. Sung, M. Mehta, V. Raman, R. O. Fox, Large eddy simulation modeling of flame synthesis of TiO_2 nanoparticles using bivariate population balance with conditional quadrature method of moments, In preparation.

- Y. Sung, V. Raman, R. O. Fox, Large-eddy-simulation-based multiscale modeling of TiO_2 nanoparticle synthesis in a turbulent flame reactor using detailed nucleation chemistry, Chemical Engineering Science, Accepted for publication and in print.

- M. Mehta, Y. Sung, V. Raman, R. O. Fox, Multiscale modeling of TiO_2 nanoparticle production in flame reactors: Effect of chemical mechanism, Industrial Engineering & Chemistry Research, 2010, 49(21), pp.10663-10673

- M. Mehta, Y. Sung, V. Raman, R. O. Fox, Multiscale simulation of titania nanoparticle evolution in a turbulent flame, International Journal of Multiscale Computational Engineering, Submitted

- Y. Sung, M. Mehta, V. Raman, R. O. Fox, LES-based multiscale modeling of nanoparticle synthesis in flame reactors, International Conference on Numerical Combustion (ICNC2011), Sep. 2011, Edinburgh, UK

- M. Mehta, Y. Sung, V. Raman, R. O. Fox, A multiscale modeling approach for TiO_2 nanoparticle production in flame reactors, 21st Interna-

tional Symposium on Chemical Reaction Engineering (ISCRE 21), Jun. 2010, Philadelphia, PA, USA

- Y. Sung, M. Mehta, V. Raman, R. O. Fox, Multiscale models for nanoparticle synthesis in turbulent flames, Symposium on Multi-Scale Modelling for Industrial Flow Systems – A CSIRO cutting edge science symposium (MSM 2009), Dec. 2009, Melbourne, Australia

- Y. Sung, M. Mehta, V. Raman, R. O. Fox, Large eddy simulation of nanoparticle formation in turbulent flames, AIChE Annual Meeting, Nov. 2010, Salt Lake City, UT, USA

- Y. Sung, M. Mehta, V. Raman, R. O. Fox, Large eddy simulations of titania nanoparticle evolution in a turbulent flame with detailed chemistry, AIChE Annual Meeting, Nov. 2009, Nashville, TN, USA

- Y. Sung, H. Koo, V. Raman, R. O. Fox, M. C. Heine, S. E. Pratsinis, Direct numerical simulation of nanoparticle evolution in turbulent flames, AIChE Annual Meeting, Nov. 2008, Philadelphia, PA, USA

- S. H. Kim, Y. Sung, V. Raman, Effect of inlet shape on transverse-jet mixing process, AIChE Annual Meeting, Nov. 2008, Philadelphia, PA, USA

- Y. Sung, H. Koo, V. Raman, Effect of exit shape on mixing efficiency in crossflow jets, AIChE Annual Meeting, Nov. 2007, Salt Lake City, UT, USA

Bibliography

[1] R. H. West, R. A. Shirley, M. Kraft, C. F. Goldsmith, and W. H. Green. A detailed kinetic model for combustion synthesis of titania from $TiCl_4$. *Combust. Flame*, 156(9):1764–1770, 2009.

[2] M. Mehta, Y. Sung, V. Raman, and R. O. Fox. Multiscale modeling of TiO_2 nanoparticle production in flame reactors: Effect of chemical mechanism. *Ind. Eng. Chem. Res.*, 49(21):10663–10673, 2010.

[3] J. Cheng and R. O. Fox. Kinetic modeling of nanoprecipitation using CFD coupled with a population balance. *Ind. Eng. Chem. Res.*, 49(21):10651–10662, 2010.

[4] S. E. Pratsinis, W. Zhu, and S. Vemury. The role of gas mixing in flame synthesis of titania powders. *Powder Technol.*, 86(1):87–93, 1996.

[5] R. McGraw. Correcting moment sequences for errors associated with advective transport. `http://www.ecd.bnl.gov/pubs/momentcorrection_mcgraw2006.pdf`, 2006.

[6] R. Strobel and S. E. Pratsinis. Flame aerosol synthesis of smart nanostructured materials. *J. Mater. Chem.*, 17:4743–4756, 2007.

[7] T. Johannessen, S. E. Pratsinis, and H. Livbjerg. Computational fluid-particle dynamics for the flame synthesis of alumina particles. *Chem. Eng. Sci.*, 55:177–191, 2000.

[8] H. K. Kammler, L. Mädler, and S. E. Pratsinis. Flame synthesis of nanoparticles. *Chem. Eng. Technol.*, 24(6):583–596, 2001.

[9] A. M. Ruiz, G. Sakai, A. Cornet, K. Shimanoe, J. R. Morante, and N. Yamazoe. Cr-doped TiO_2 gas sensor for exhaust NO_2 monitoring. *Sensor Actuat. B-Chem.*, 93(1-3):509–518, 8 2003.

[10] F. E. Kruis, H. Fissan, and A. Peled. Synthesis of nanoparticles in the gas phase for electronic, optical and magnetic applications-A review. *J. Aerosol Sci.*, 29(5-6):511–535, 6 1998.

[11] V. M. Litvinov and P. A. M. Steeman. EPDM-carbon black interactions and the reinforcement mechanisms, as studied by low-resolution 1H NMR. *Macromolecules*, 32(25):8476–8490, 11 1999.

[12] C. Zhu, Q. Yu, R. N. D., and R. Pfeffer. Gas fluidization characteristics of nanoparticle agglomerates. *AIChE J.*, 51(2):426–439, 2005.

[13] S. Loher, W. J. Stark, M. Maciejewski, A. Baiker, S. E. Pratsinis, D. Reichardt, F. Maspero, F. Krumeich, and D. Gunther. Fluoro-apatite and calcium phosphate nanoparticles by flame synthesis. *Chem. Mater.*, 17(1):36–42, 12 2004.

[14] A. Teleki and S. E. Pratsinis. Blue nano titania made in diffusion flames. *Phys. Chem. Chem. Phys.*, 11:3742–3747, 2009.

[15] E. Ukaji, T. Furusawa, M. Sato, and N. Suzuki. The effect of surface modification with silane coupling agent on suppressing the photocatalytic activity of fine TiO_2 particles as inorganic UV filter. *Appl. Surf. Sci.*, 254(2):563–569, 2007.

[16] A. Fujishima. Discovery and applications of photocatalysis - creating a comfortable future by making use of light energy. *Japan Nanonet Bulletin*, 44, May 2005.

[17] P. Roth. Particle synthesis in flames. *Proc. Combust. Inst.*, 31:1773–1788, 2007.

[18] V. Raman and R. O. Fox. Collaborative research: development of a predictive multiphysics computational model for nanoparticle synthesis using flame-spray pyrolysis. Proposal Number: CBET-0730612/CBET-0730369, August 2007.

[19] T. Hibino, S. Wang, S. Kakimoto, and M. Sano. Single chamber solid oxide fuel constructed from an yttria-stabilized zirconia electrolyte. *Electrochem. Solid. St.*, 2(7):317–319, 1999.

[20] L. Zhang, T. Kanki, N. Sano, and A. Toyoda. Development of TiO_2 photocatalyst reaction for water purification. *Sep. Purif. Technol.*, 31(1):105–110, 2003.

[21] U. Bach, D. Lupo, P. Comte, J. E. Moser, F. Weissörtel, J. Salbeck, H. Spreitzer, and M. Grätzel. Solid-state dye-sensitized mesoporous TiO_2 solar cells with high photon-to-electron conversion efficiencies. *Nature*, 395:583–585, 1998.

[22] G. D. Ulrich. Flame synthesis of fine particles. *Chem. Eng. News*, 62:22–29, 1984.

[23] T. Johannessen, J. R. Jensen, M. Mosleh, J. Johansen, U. Quaade, and H. Livbjerg. Flame synthesis of nanoparticles: Applications in catalysis and product/process engineering. *Chem. Eng. Res. Des.*, 82(11):1444–1452, 2004.

[24] S. E. Pratsinis. Flame aerosol synthesis of ceramic powder. *Prog. Ener. Combust. Sci.*, 24:197–219, 1998.

[25] L. Mädler, W. J. Stark, and S. E. Pratsinis. Rapid synthesis of stable ZnO quantum dots. *J. Appl. Phys.*, 92(11):6537–6540, 2002.

[26] R. W. Siegel, E. Hu, and M. C. Roco, editors. *Nanostructure Science And Technology: R & D Status And Trends In Nanoparticles, Nanostructured Materials And Nanodevices.* Kluwer Academic Publishers, 1999.

[27] M. C. Roco. Nanoparticles and nanotechnology research. *J. Nanopart. Res.*, 1:1–6, 1999.

[28] K. Wegner and S. E. Pratsinis. Scale-up of nanoparticle synthesis in diffusion flame reactors. *Chem. Eng. Sci.*, 58:4581–4589, 2003.

[29] D. E. Rosner. Flame synthesis of valuable nanoparticles: recent progress/current needs in areas of rate laws, population dynamics, and characterization. *Ind. Eng. Chem. Res.*, 44:6045–6055, 2005.

[30] K. Wegner, B. Walker, S. Tsantilis, and S. E. Pratsinis. Design of metal nanoparticle synthesis by vapor flow condensation. *Chem. Eng. Sci.*, 57(10):1753–1762, 5 2002.

[31] A. Kumar Gupta and M. Gupta. Synthesis and surface engineering of iron oxide nanoparticles for biomedical applications. *Biomaterials*, 26(18):3995–4021, 6 2005.

[32] H. K. Kammler, R. Jossen, P. W. Morrison, S. E. Pratsinis, and G. Beaucage. The effect of external electric fields during flame synthesis of titania. *Powder Technol.*, 135-136:310–320, 10 2003.

[33] D. B. Geohegan, A. A. Puretzky, G. Duscher, and S. J. Pennycook. Time-resolved imaging of gas phase nanoparticle synthesis by laser ablation. *Appl. Phys. Lett.*, 72(23):2987–2989, 1998.

[34] S. K. Friedlander. *Smoke, dust, and haze - Fundamentals of aerosol dynamics*. Oxford University Press, 2000.

[35] L. Mädler, H. Kammler, R. Mueller, and S. E. Pratsinis. Controlled synthesis of nanostructured particles by flame spray pyrolysis. *J. Aerosol Sci.*, 33:369–389, 2002.

[36] R. Müller, L. Mädler, and S. E. Pratsinis. Nanoparticle synthesis at high production rates by flame spray pyrolysis. *Chem. Eng. Sci.*, 58:1969–1976, 2003.

[37] T. Tani, N. Watanabe, and K. Takatori. Emulsion combustion and flame spray synthesis of zinc oxide/silica particles. *J. Nanopart. Res.*, 5(1):39–46, 04 2003.

[38] M. C. Heine and S. E. Pratsinis. Droplet and particle dynamics during flame spray synthesis of nanoparticles. *Ind. Eng. Chem. Res.*, 44:6222–6232, 2005.

[39] R. Baranwal, M. P. Villar, R. Garcia, and R. M. Laine. Flame spray pyrolysis of precursors as a route to nano-mullite powder: Powder characterization and sintering behavior. *J. Am. Ceram. Soc.*, 84(5):951–961, 2001.

[40] W. J. Stark, L. Mädler, M. Maciejewski, S. E. Pratsinis, and A. Baiker. Flame synthesis of nanocrystalline ceria-zirconia: effect of carrier liquid. *Chem. Commun.*, 5:588–589, 2003.

[41] J. M. Mäkelä, H. Keskinen, T. Forsblom, and J. Keskinen. Generation of metal and metal oxide nanoparticles by liquid flame spray process. *J.*

Mater. Sci., 39(8):2783–2788, 2004.

[42] A. Pitkänen, J. M. Mäkelä, M. Nurminen, A. Oksanen, K. Janka, J. Keskinen, H. Keskinen, J. K. Liimatainen, S. Hellstén, and T. Määttä. Numerical study of silica particle formation in turbulent H/O flame. *IFRF Combustion Journal*, page Article 200509, 2005.

[43] R. M. Laine, J. C. Marchal, H. P. Sun, and X. Q. Pan. Nano-alpha-Al_2O_3 by liquid-feed flame spray pyrolysis. *Nature Materials*, 5(9):710–712, 2006.

[44] H. Schulz, L. Mädler, R. Strobel, R. Jossen, S. E. Pratsinis, and Tue Johannessen. Independent control of metal cluster and ceramic particle characteristics during one-step synthesis of Pt/TiO_2. *J. Mater. Res.*, 20(9):2568–2577, 2005.

[45] T. Johannessen, S. E. Pratsinis, and H. Livbjerg. Computational analysis of coagulation and coalescence in the flame synthesis of titania particles. *Powder Technol.*, 118(3):242–250, 2001.

[46] H. J. Kim, J. I. Jeong, Y. Park, Y. Yoon, and M. Choi. Modeling of generation and growth of non-spherical nanoparticles in a co-flow flame. *J. Nanopart. Res.*, 5(3):237–246, 08 2003.

[47] G. Wang and S. C. Garrick. Modeling and simulation of titania synthesis in two-dimensional methane-air flames. *J. Nanopart. Res.*, 7:621–632, 2005.

[48] G. Wang and S. C. Garrick. Modeling and simulation of titania formation and growth in temporal mixing layers. *J. Aerosol Sci.*, 37:431–451, 2006.

[49] A. Zucca, D. L. Marchisio, A. A. Barresi, and R. O. Fox. Implementation of the population balance equation in CFD codes for modeling soot formation in turbulent flames. *Chem. Eng. Sci.*, 61:87–95, 2006.

[50] D. L. Marchisio and A. A. Barresi. Investigation of soot formation in turbulent flames with a pseudo-bivariate population balance model. *Chem. Eng. Sci.*, 64(2):294–303, 2009.

[51] F. E. Kruis, K. A. Kusters, S. E. Pratsinis, and B. Scarlett. A simple model for the evolution of the characteristics of aggregate particles undergoing coagulation and sintering. *Aerosol Sci. Tech.*, 19(4):514–526, 1993.

[52] S. Modem, S. C. Garrick, M. R. Zachariah, and K. E. J. Lehtinen. Direct numerical simulation of nanoparticle coagulation in a temporal mixing layer. *Proc. Combust. Inst.*, 29:1071–1077, 2002.

[53] N. Settumba and S. C. Garrick. Direct numerical simulation of nanoparticle coagulation in a temporal mixing layer via a moment method. *J. Aerosol Sci.*, 34:149–167, 2003.

[54] E. G. Moody and L. R. Collins. Effect of mixing on the nucleation and growth of titania particles. *Aerosol Sci. Tech.*, 37:403–424, 2003.

[55] J. I. Jeong and M. Choi. Analysis of non-spherical polydisperse particle growth in a two-dimensional tubular reactor. *J. Aerosol Sci.*, 34(6):713–732, 6 2003.

[56] M. Kamal Akhtar, Y. Xiong, and S. E. Pratsinis. Vapor synthesis of titania powder by titanium tetrachloride oxidation. *AIChE J.*, 37(10):1561–1570, 1991.

[57] J. Y. Hwang, Y. S. Gil, J. I. Kim, M. Choi, and S. H. Chung. Measurements of temperature and OH radical distributions in a silica generating flame using CARS and PLIF. *J. Aerosol Sci.*, 32(5):601–613, 5 2001.

[58] L. Wang and R. O. Fox. Application of in situ adaptive tabulation to CFD simulation of nano-particle formation by reactive precipitation. *Chem. Eng. Sci.*, 58:4387–4401, 2003.

[59] D. L. Marchisio, R. D. Vigil, and R. O. Fox. Implementation of the quadrature method of moments in CFD codes for aggregation-breakage problems. *Chem. Eng. Sci.*, 58(15):3337–3351, 2003.

[60] S. E. Miller and S. C. Garrick. Nanoparticle coagulation in a planar jet. *Aerosol Sci. Tech.*, 38:79–89, 2004.

[61] L. Wang, D. C. Haworth, S. R. Turns, and M.F. Modest. Interactions among soot, thermal radiation, and NOx emissions in oxygen-enriched turbulent nonpremixed flames: a computational fluid dynamics modeling study. *Combust. Flame*, 141:170–179, 2005.

[62] L. Wang, N. E. Endrud, S. R. Turns, M. D. D'Agostini, and A. G. Slavejkov. A study of the influence of oxygen index on soot, radiation, and emission characteristics of turbulent jet flames. *Combust. Sci. Technol.*, 174(8):45–72, 2002.

[63] M. Yu, J. Lin, L. Chen, and T. Chan. Large eddy simulation of a planar jet flow with nanoparticle coagulation. *Acta Mechanica Sinica*, 22:293–300, 2006.

[64] M. Soos, L. Wang, R. O. Fox, J. Sefcik, and M. Morbidelli. Population balance modeling of aggregation and breakage in turbulent Taylor-Couette flow. *J. Colloid Interf. Sci.*, 307:433–446, 2007.

[65] M. Yu, J. Lin, and T. Chan. Numerical simulation of nanoparticle synthesis in diffusion flame reactor. *Powder Technol.*, 181:9–20, 2008.

[66] M. Yu, J. Lin, and T. Chan. Effect of precursor loading on non-spherical TiO_2 nanoparticle synthesis in a diffusion flame reactor. *Chem. Eng. Sci.*, 63:2317–2329, 2008.

[67] M. E. Mueller, G. Blanquart, and H. Pitsch. Hybrid method of moments for modeling soot formation and growth. *Combust. Flame*, 156(6):1143–1155, 2009.

[68] C. P. Leusden and N. Peters. Experimental and numerical analysis of the influence of oxygen on soot formation in laminar counterflow flames of acetylene. *Proc. Combust. Inst.*, 28(2):2619–2625, 2000.

[69] M. Petitti, A. Nasuti, D. L. Marchisio, M. Vanni, G. Baldi, N. Mancini, and F. Podenzani. Bubble size distribution modeling in stirred gas - liquid reactors with QMOM augmented by a new correction algorithm. *AIChE J.*, 56(1):36–53, Jan 2010.

[70] M. Laakkonen, P. Moilanen, V. Alopaeus, and J. Aittamaa. Modeling local bubble size distributions in agitated vessels. *Chem. Eng. Sci.*, 62:721–740, 2007.

[71] G. di Veroli and S. Rigopoulos. Modeling of turbulent precipitation: A transported population balance-PDF method. *AIChE Journal*, 56(4):878–892, 2010.

[72] J. Baldyga and W. Orciuch. Barium sulphate precipitation in a pipe - an experimental study and CFD modelling. *Chem. Eng. Sci.*, 56:2435—2444, 2001.

[73] Y. Sung, V. Raman, R. O. Fox, M. C. Heine, and S. E. Pratsinis. Direct numerical simulation of nanoparticle evolution in turbulent spray flames. In *AIChE Annual Meeting*, Philadelphia, PA, USA, 2008.

[74] S. B. Pope. *Turbulent flows.* Cambridge University Press, 2000.

[75] N. Peters. *Turbulent Combustion.* Cambridge University Press, 2000.

[76] H. Pitsch. Large-eddy simulation of turbulent combustion. *Annu. Rev. Fluid Mech.*, 38:453–482, 2006.

[77] V. Raman and H. Pitsch. A consistent LES/filtered-density function formulation for the simulation of turbulent flames with detailed chemistry. *Proc. Combust. Inst.*, 31:1711–1719, 2006.

[78] J. Smagorinsky. General circulation experiments with the primitive equations - I. The basic experiment. *Mon. Weather Rev.*, 91:99–164, 1963.

[79] J. Bardina, J. H. Ferziger, and W. C. Reynolds. Improved subgrid models for large eddy simulation. In *AIAA Fluid and Plasma Dynamics Conference, 13th, Snowmass, CO, July 14-16*, page 10, 1980.

[80] M. Germano. Turbulence: the filtering approach. *J. Fluid Mech.*, 238:325–336, 1992.

[81] P. Moin, K. Squires, W. Cabot, and S. Lee. A dynamic subgrid-scale model for compressible turbulence and scalar transport. *Physics of Fluids A*, 3:2746–2757, 1991.

[82] S. Ghosal, T. S. Lund, P. Moin, and K. Akselvoll. A dynamic localization model for large-eddy simulation of turbulent flows. *J. Fluid Mech.*, 286:229–255, 1995.

[83] H. Pitsch and H. Steiner. Scalar mixing and dissipation rate in large-eddy simulations of non-premixed turbulent combustion. *Proc. Combust. Inst.*, 28(1):41–49, 2000.

[84] C. D. Pierce. *Progress-variable approach for large-eddy simulation of turbulence combustion*. PhD thesis, Stanford University, 2001.

[85] C. D. Pierce and P. Moin. A dynamic model for subgrid-scale variance and dissipation rate of a conserved scalar. *Phys. Fluids*, 10:3041–3044, 1998.

[86] H. Pitsch. A C++ computer program for 0-D and 1-D laminar flame calculations. RWTH Aachen, 1998.

[87] P. T. Spicer, O. Chaoul, S. Tsantilis, and S. E. Pratsinis. Titania formation by $TiCl_4$ gas phase oxidation, surface growth and coagulation. *J. Aerosol Sci.*, 33:17–34, 2002.

[88] R. H. West, G. J. O. Beran, W. H. Green, and M. Kraft. First-principles thermochemistry for the production of TiO_2 from $TiCl_4$. *J. Phys. Chem. A*, 111(18):3560–3565, 2007a.

[89] R. H. West, M. S. Celnik, O. R. Inderwildi, M. Kraft, G. J. O. Beran, and W. H. Green. Toward a comprehensive model of the synthesis of TiO_2 particles from $TiCl_4$. *Ind. Eng. Chem. Res.*, 46:6147–6156, 2007.

[90] C. T. Bowman, R. K. Hanson, D. F. Davidson, W. C. Gardiner Jr., V. Lissianski, G.P. Smith, D. M. Golden, M. Frenklach, and M. Goldenberg. GRI-Mech 2.11, http://www.me.berkeley.edu/gri_mech, 1996.

[91] P. J. Colucci, F. A. Jaberi, and P. Givi. Filtered density function for large eddy simulation of turbulent reacting flows. *Phys. Fluids*, 10(2):499–515, 1998.

[92] S. B. Pope. A Monte Carlo method for the PDF equations of turbulent reactive flow. *Combust. Sci. Technol.*, 25:159–174, 1981.

[93] R. McGraw. Description of aerosol dynamics by the quadrature method of moments. *Aerosol Sci. Tech.*, 27:255–265, 1997.

[94] S. Rigopoulos. PDF method for population balance in turbulent reactive flow. *Chem. Eng. Sci.*, 62:6865–6878, 2007.

[95] S. E. Pratsinis and P. T. Spicer. Competition between gas phase and surface oxidation of $TiCl_4$ during synthesis of TiO_2. *Chem. Eng. Sci.*, 53(10):1861–1868, May 1998.

[96] R. N. Ghoshtagore. Mechanism of heterogeneous deposition of thin film rutile. *J. Electrochem. Soc.: Solid State Sci.*, 117(4):529–534, 1970.

[97] P. Meakin. Formation of fractal clusters and networks by irreversible diffusion-limited aggregation. *Phys. Rev. Lett.*, 51(13):1119–1122, Sep 1983.

[98] S. C. Garrick, K. E. J. Lehtinen, and M. R. Zachariah. Nanoparticle coagulation via a Navier-Stokes/nodal methodology: Evolution of the particle field. *J. Aerosol Sci.*, 37:555–576, 2006.

[99] M. C. Heine and S. E. Pratsinis. Polydispersity of primary particles in agglomerates made by coagulation and sintering. *J. Aerosol Sci.*, 38(1):17–38, 2007.

[100] O. Desjardins, R. O. Fox, and P. Villedieu. A quadrature-based moment method for dilute fluid-particle flows. *J. Comput. Phys.*, 227:2514–2539, 2008.

[101] R. O. Fox. A quadrature-based third-order moment method for dilute gas-particle flows. *J. Comput. Phys.*, 227:6313–6350, 2008.

[102] O. Desjardins, R. O. Fox, and P. Villedieu. A quadrature-based moment closure for the Williams spray equation. In *Proceedings of the Summer Program*, page 223, Stanford University, 2006. Center for Turbulence Research.

[103] D. E. Rosner. Improved rate laws and population balance simulation methods; CRE applications, including the combustion synthesis of valuable nano-particles. *Int. J. Chem. React. Eng.*, 4:Article A21, 2006.

[104] Y. Liu, C. Cheng, Y. Liu, R. K. Prud'homme, and R. O. Fox. Mixing in a multi-inlet vortex mixer (MIVM) for flash nano-precipitation. *Chem. Eng. Sci.*, 63:2829—2842, 2008.

[105] M. Mehta, Y. Sung, V. Raman, and R. O. Fox. A multiscale modeling approach for TiO_2 nanoparticle production in flame reactors. In *21st In-*

ternational Symposium on Chemical Reaction Engineering (ISCRE 21), Philadelphia, PA, USA, 2010.

[106] P. Donde, H. Koo, and V. Raman. A multivariate quadrature based moment method for LES based modeling of supersonic combustion. Submitted, 2011.

[107] Y. Sung, V. Raman, and R. O. Fox. Large-eddy-simulation-based multiscale modeling of TiO_2 nanoparticle synthesis in a turbulent flame reactor using detailed nucleation chemistry. *Chem. Eng. Sci.*, 2011. In print.

[108] J. C. Barrett and N. A. Webb. A comparison of some approximate methods for solving the aerosol general dynamic equation. *J. Aerosol Sci.*, 29:31–39, 1998.

[109] D. L. Marchisio, A. A. Barresi, and R. O. Fox. Simulation of turbulent precipitation in a semi-batch Taylor-Couette reactor using CFD. *AIChE J.*, 47(3):664–676, 2001.

[110] D. E. Rosner and J. J. Pyykönen. Bivariate moment simulation of coagulating and sintering nanoparticles in flames. *AIChE J., Particle Technology and Fluidization*, 48(3):476–491, 2002.

[111] D. L. Marchisio, A. A. Barresi, and M. Garbero. Nucleation, growth, and agglomeration in barium sulfate turbulent precipitation. *AIChE J.*, 48(9):2039–2050, 2002.

[112] D. Grosschmidt, H. Bockhorn, M. Goodson, and M. Kraft. Two approaches to the simulation of silica particle synthesis. *Proc. Combust. Inst.*, 29:1039–1046, 2002.

[113] D. E. Rosner, R. McGraw, and P. Tandon. Multivariate population balances via moment and Monte Carlo simulation methods: An important sol reaction engineering bivariate example and "mixed" moments for the estimation of deposition, scavenging, and optical properties for populations of nonspherical suspended particles. *Ind. Eng. Chem. Res.*, 42:2699–2711, 2003.

[114] D. L. Marchisio, R. D. Vigil, and R. O. Fox. Quadrature method of moments for aggregation-breakage processes. *J. Colloid Interf. Sci.*, 258:322–334, 2003.

[115] S. S. Talukdar and M. T. Swihart. Aerosol dynamics modeling of silicon nanoparticle formation during silane pyrolysis: a comparison of three solution methods. *J. Aerosol Sci.*, 35(7):889–908, 7 2004.

[116] L. Wang, R. D. Vigil, and R. O. Fox. CFD simulation of shear-induced aggregation and breakage in turbulent Taylor–Couette flow. *J. Colloid Interf. Sci.*, 285:167—178, 2005.

[117] J. Sanyal, D. L. Marchisio, R. O. Fox, and K. Dhanasekharan. On the comparison between population balance models for CFD simulation of bubble columns. *Ind. Eng. Chem. Res.*, 44:5063–5072, 2005.

[118] G. H. Gordon. Error bounds in equilibrium statistical mechanics. *J. Math. Phys.*, 9:655–672, 1968.

[119] M. Mehta and R. O. Fox. Solution of a bivariate distribution fuction for nanoparticle formation in flame reactors.

[120] R. I. A. Patterson, O. C., and M. Kraft. Models for the aggregate structure of soot particles. *Combust. Flame*, 151:160–172, 2007.

[121] S. K. Friedlander and M. K. Wu. Linear rate law for the decay of excess surface area of a coalescencing solid particle. *Phys. Rev. B*, 49:347, 1994.

[122] O. Desjardins, G. Blanquart, G. Balarac, and H. Pitsch. High order conservative finite difference scheme for variable density low Mach number turbulent flows. *J. Comput. Phys.*, 227:7125–7159, 2008.

[123] M. Herrmann, G. Blanquart, and V. Raman. A bounded QUICK scheme for preserving scalar bounds in large-eddy simulations. *AIAA J.*, 44(12):2879–2886, 2006.

[124] O. Desjardins, G. Blanquart, G. Balarac, and H. Pitsch. High order conservative finite difference scheme for variable density low Mach number turbulent flows. *J. Comput. Phys.*, 227:7125–7159, 2008.

[125] K. Radhakrishnan and A. C. Hindmarsh. Description and use of LSODE, the Livermore solver for ordinary differential equations. *Lawrence Livermore National Laboratory Report*, UCRL-ID-113855, 1993.

[126] Personal discussion with M. Mehta.

[127] D. L. Wright. Numerical advection of moments of the particle size distribution in Eulerian models. *J. Aerosol Sci.*, 38:352–369, 2007.

[128] J. A. Shohat and J. D. Tamarkin. *The problem of moments*, volume Mathematical Surveys and monograph, Vol. 1. American Mathematical Society, 1963.

[129] X.-D. Liu, S. Osher, and T. Chan. Weighted essentially non-oscillatory schemes. *J. Comput. Phys.*, 115(200–212), 1994.